



Norwegian University of Life Sciences  
Faculty of Science and Technology

Philosophiae Doctor (PhD)  
Thesis 2023:53

# Toward monitoring of photovoltaic power plants with photoluminescence imaging

Mot monitorering av fotovoltaiske  
kraftverk med fotoluminescensavbildning

Marija Vuković



# Toward monitoring of photovoltaic power plants with photoluminescence imaging

Mot monitorering av fotovoltaiske kraftverk med  
fotoluminescensavbildning

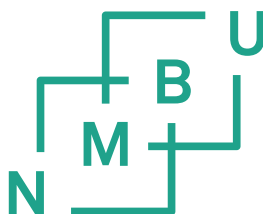
**Philosophiae Doctor (PhD) Thesis**

Marija Vuković

Norwegian University of Life Sciences

Faculty of Science and Technology

Ås, 2023



Thesis number: 2023:53

ISSN: 1894-6402

ISBN: 978-82-575-2082-3



---

# Abstract

It is predicted that the photovoltaic energy conversion will be the largest installed power capacity by 2027. The least costly option for new electricity generation in many of the world's countries will be the utility-scale solar photovoltaic electricity generation. Accurate monitoring of solar plants for localizing and detecting faults is expected to be one of the critical tasks facing the energy industry.

Imaging of photovoltaic modules for the purpose of fault detection can be more efficient and accurate compared to measurements of electrical parameters. Different spectral regions provide different types of information about a faulty module. Detection of photoluminescence, that is, radiation emitted upon band-to-band recombination after charge carrier excitation with an illumination source, has shown a great potential in the laboratory setting. In the recent years, the first approaches in the outdoor setting have been conducted on silicon modules with the Sun as an excitation source.

However, the reflected sunlight overlaps spectrally with the emitted photoluminescence. The imaging apparatus detects the total signal out of which only a few percent represent the emitted photoluminescence. Several approaches for elimination of more than 95% of the total signal have been suggested in the recent years. They are either based on controlling the emission of photoluminescence during imaging to achieve a variation in signal strength and, thus, a separation from the reflected solar irradiance, or on filtering of reflected solar irradiance with specially designed, narrow band-pass filters. The former requires interfering with the production to modulate the operating point of the modules between two operating conditions. This has been implemented by using additional equipment connected physically to a certain number of modules it is dimensioned for and by moving it during imaging.

We have tried to develop an approach for photoluminescence imaging which would enable imaging of as many modules as possible with as little interference as possible for an easier implementation on a utility-scale photovoltaic power plant. This has

---

been done by using the capabilities of a string inverter to change the operating point of a string. The first approach is based on remote control of the operating point between two conditions. The second approach is far less invasive and takes the advantage of the string inverter's built-in functionality to conduct current-voltage curve sweeps. Both approaches enable variation of the operating point on more than one string.

The approach with current-voltage curve sweeps implies that a string undergoes an entire range of operating conditions, which results in a continuously changing photoluminescence signal. From such a data set one can obtain more information about modules' defects than what is possible from an image set obtained during controlled modulation between two conditions. Therefore, it is more time-consuming to process an image set acquired during a current-voltage curve sweep. We propose an alternative algorithm which performs better in case of unsupervised image processing in real time. This way of imaging and data processing is also applicable in irradiance conditions below  $100 \text{ Wm}^{-2}$ . The mentioned aspects of our photoluminescence imaging approach and the novel algorithm make this technique promising for large-scale inspections.

---

# Sammendrag

Ifølge prognoser vil fotovoltaisk energikonvertering være den største installerte effektkapasiteten innen 2027. I mange land vil storskala solcelleanlegg være den rimeligste løsningen for ny energiproduksjon. Presis monitorering av fotovoltaiske kraftverk med mål om lokalisering og detektering av feil forventes å være én av energiindustriens kritiske oppgaver.

Avbildning av fotovoltaiske moduler for å detektere feil kan være mer effektivt og gi mer nøyaktige resultater enn målinger av elektriske parametere. Detektering av fotoluminescens med kamera, dvs. stråling avgitt fra halvledermaterialet silisium i forbindelse med bånd-til-bånd-rekombinasjon etter eksitasjon av elektroner med en lyskilde, har vist stort potensiale. De første forsøkene med sola som eksitasjonsskilde har blitt gjennomført på silisium moduler i de siste årene.

Det reflekterte sollyset i det samme bølgelengdeområdet som det fotoluminescerende signalet blir også detektert av kamerautstyret. Fotoluminescens utgjør kun noen få prosent av det totale signalet. Flere metoder for å skille fotoluminescens fra det reflekterte sollyset har blitt foreslått. De baserer seg enten på kontrollert emisjon av fotoluminescenssignalet i løpet av avbildningen for å oppnå en variasjon i signalet som skal gjøre det mulig å separere det fra det reflekterte sollyset, eller på detektering av kun fotoluminescens gjennom spesiallagde, smale bånd-pass filtre. Førstnevnte krever inngrep i modulenes strømproduksjon for å styre operasjonspunktet mellom to tilstander. Dette kan gjennomføres ved at tilleggsutstyr kobles på modulene og flyttes i løpet av avbildningen.

Vi har jobbet med å utvikle en tilnærming for fotoluminescensavbildning av så mange moduler så mulig med så lite inngrep som mulig. Formålet har vært å utvikle en avbildningsmetode som vil kunne gjennomføres på storskala solcelleanlegg. Dette har blitt gjort ved å utnytte funksjonalitetene til en strenginverter. Den ene tilnærmingen har vært kontaktløs styring av operasjonspunktet gjennom strenginverteren og dermed uten tilleggsutstyr som må flyttes i løpet av avbildningen. En forbedring av denne metoden baserer seg på utnyttelse av streng-

---

inverterens innebygde egenskap til å skanne strøm-spenningsskarakteristikken til en gitt streng og er derfor betraktelig mindre inngripende. Begge tilnærmingene muliggjør en endring i operasjonspunktet på mer enn én streng av gangen.

Tilnærmingen med skanningen av strøm-spenningsskarakteristikken innebærer at strengen(e) går gjennom en hel rekke av operasjonstilstander som resulterer i et fotoluminescenssignal i kontinuerlig endring. En slik bildeserie gir mer informasjon om modulenes defekter enn en bildeserie tatt i løpet av den kontrollerte styringen av operasjonspunktet mellom to tilstander. Det er derfor mer tidkrevende å prosessere en bildeserie samlet med den førstnevnte metoden. I den forbindelse foreslår vi en alternativ algoritme som gir bedre resultater med ikke-styrt bildebehandling i sanntid. Metoden er også anvendelig ved veldig lave irradiansnivåer, under  $100 \text{ W m}^{-2}$ . Metoden for fotoluminescensavbildning mens skanningen av strøm-spenningsskarakteristikken pågår i kombinasjon med den nye algoritmen for bildebehandling er lovende for videre utvikling med hensyn på storskala avbildning.



---

# Preface

The work presented in this thesis was conducted from 2018 to 2023 at the Norwegian University of Life Sciences (NMBU), Faculty of Science and Technology, in the research group for Solar Energy. It was funded by The Research Center for Sustainable Solar Cell Technology as a part of its research activity in Working package 4: End use and impact. I would like to thank both the University and the Research Center for this opportunity.

I would like to thank my supervisors for believing in me from the start and throughout the duration of this project despite all the setbacks. I am grateful to my supervisor, Professor Ingunn Burud, for teaching me that there is a solution to every challenge. I would also like to thank my co-supervisor, Professor Espen Olsen, for all his guidance and valuable pieces of advice both professionally and personally. I am grateful to my co-supervisor Dr. Andreas Svarstad Flø for all the help regarding practical aspects of this project. I would like to thank PhD coordinator Berit Hauger Lindstad for always having her door open for PhD students in need.

I would like to thank my coauthors for their invaluable contributions. I am grateful to Marko Jakovljevic for his continuous help throughout this entire project. Marko's vision that photoluminescence imaging should be possible without controlling the operating point of the modules was the turning point of this thesis. I would like to thank Ingeborg Eriksdatter Høiaas for all her help and support in the most difficult phase of this thesis. I would also like to thank Professor Ulf Geir Indahl and Professor Kristian Hovde Liland for their time and energy invested in our project and for their invaluable contribution to making this thesis complete. I am grateful to Mirabai Hillestad for the insightful questions and discussions which helped me redefine the frames of this work in a larger context.

I am grateful to Professor Jorge Mario Marchetti for his friendship and for the memorable pieces of advice which lifted me up when it seemed that there was no hope left. I would like to thank Dr. Torbjørn Mehl for all the valuable conversations, meticulous proofreading and for being a friend and advisor. I am grateful

---

to Åshild Grøtan for being a friend in every respect and for always being available when I needed to reflect on professional and personal challenges. I am grateful to Kristin Solvang for her friendship during the years at the NMBU. They would have been bleak otherwise. I would also like to thank Arnoud Jochemsen, Agnieszka Kuras, Sahameh Shafiee, Sepideh Niazi, Ivar Loland Råheim and Sondre Grevle Iveland for companionship and valuable perspectives.

I would like to thank my parents for always believing in me and for helping me in every possible way as well as to my sister for vigorously cheering on me at every corner. I am grateful to my husband who, apart from contributing immensely to this thesis in a professional way, teaches me the virtue of patience and understanding every single day. I am grateful to my little girl for giving me the strength and the reason to carry through this project.

Marija Vuković

Ås, May 2023

---

# List of Papers

## Paper A

---

M Vuković, I E Høiaas, M Jakovljević, A S Flø, E Olsen, I Burud.  
Photoluminescence imaging of silicon modules in a string. *Progress  
in Photovoltaics: Research and Applications*, 30(4):436-446, 2022

## Paper B

---

M Vuković, I E Høiaas, M Jakovljević, A S Flø, E Olsen, I Burud.  
Outdoor photoluminescence and electroluminescence imaging of  
photovoltaic silicon modules in a string. *AIP Conference Proceedings*,  
volume 2487, page 030012, 2022

## Paper C

---

M Vuković, M Jakovljević, A S Flø, E Olsen, I Burud. Noninvasive  
photoluminescence imaging of silicon PV modules in daylight.  
*Applied Physics Letters*, 120(24):244102, 2022

## Paper D

---

M Vuković, K H Liland, U G Indahl, M Jakovljević, A S Flø, E  
Olsen, I Burud. Extraction of photoluminescence with Pearson  
correlation coefficient from images of field-installed photovoltaic  
modules. *Accepted by Journal of Applied Physics*

## Paper E

---

M Vuković, M Hillestad, M Jakovljević, A S Flø, E Olsen, I Burud.  
Photoluminescence imaging of field-installed photovoltaic modules in  
diffuse irradiance. *Manuscript*

---

# Contents

<b>Abstract</b>	<b>i</b>
<b>Sammendrag</b>	<b>iii</b>
<b>Preface</b>	<b>v</b>
<b>List of Papers</b>	<b>vii</b>
<b>Contents</b>	<b>ix</b>
<b>1 Introduction</b>	<b>1</b>
1.1 Overview . . . . .	1
1.2 Research question and objectives . . . . .	4
1.3 Thesis outline . . . . .	4
<b>2 Background</b>	<b>7</b>
2.1 Photoluminescence emission and detection from silicon material in daylight . . . . .	7
2.2 Photoluminescence imaging of PV modules in daylight . . . . .	10
2.2.1 Control of the operating point . . . . .	10
2.2.2 Optical filtering . . . . .	15
2.2.3 Interpretation and types of photoluminescence images . . . . .	18
2.3 Overview of the main aspects of daylight photoluminescence imaging of PV modules . . . . .	23
<b>3 Publications</b>	<b>25</b>

---

3.1	Remote control of the operating point . . . . .	25
3.1.1	Development of the imaging method: Paper A . . . . .	25
3.1.2	Defect analysis: Paper B . . . . .	29
3.2	Noninvasive photoluminescence imaging . . . . .	29
3.2.1	Development of the imaging method: Paper C . . . . .	29
3.2.2	Alternative algorithm for extraction of the photolumines- cence signal: Paper D . . . . .	31
3.2.3	Imaging in low irradiance conditions: Paper E . . . . .	34
3.3	Presented contributions compared to related studies . . . . .	35
3.4	Outlook . . . . .	38
<b>4</b>	<b>Conclusion</b>	<b>41</b>
	<b>Bibliography</b>	<b>43</b>
	<b>Appendices</b>	<b>49</b>
<b>A</b>	<b>Paper A</b>	<b>49</b>
<b>B</b>	<b>Paper B</b>	<b>63</b>
<b>C</b>	<b>Paper C</b>	<b>73</b>
<b>D</b>	<b>Paper D</b>	<b>79</b>
<b>E</b>	<b>Paper E</b>	<b>93</b>

# Chapter 1

## Introduction

### 1.1 Overview

Year 2022 was the year when the global installation of solar energy production reached 1 TW, with increasingly ambitious targets being set [1]. Compared to other renewable energy sources, solar photovoltaic (PV) accounts for more than 60% of all renewable capacity expansion. The International Energy Agency predicts that PV energy conversion will be the largest installed power capacity worldwide by 2027, totaling to more than 2.35 TW. For a significant majority of the world's countries, utility-scale solar PV is the least costly option for new electricity generation [2]. However, ensuring efficient and accurate monitoring of solar plants for localizing and detecting faults is one of the main critical tasks facing the energy industry [3, 4].

Two main groups of inspection techniques for PV power plants have been proposed thus far. The first group is based on measurements of electrical parameters [3], in which a common way of monitoring solar plants is with different types of current and voltage sensors [4]. They are usually attached to an array or a string, and their mounting is intrusive. Measurements can also be conducted at the module level, but this requires identifying, locating and disassembling a faulty module. This is time-consuming and costly [4, 5]. In addition, the exact location of the fault is not provided, as current and voltage sensors have a limited ability to pinpoint the cause

of the power loss [3, 6, 7]. The second group is based on irradiance measurements with cameras. This type of inspection enables a higher level of granularity and contactless inspection at the module level and can be combined with unmanned aerial vehicles (UAVs) for fast detection and localization of faults [3, 4].

Camera-based inspection methods can be characterized as contactless because the camera sensor does not require any contact with the PV system. However, although no camera requires contact with the PV system, there are some camera-based inspection techniques that require contact to produce the radiation that is being detected, such as in the case of luminescence-based imaging. No type of interference with the PV system is possible in case of imaging in the infrared range with a thermal infrared (TIR) camera and in the visible light range with an RGB camera.

Inspection with a TIR camera is the most common inspection technique in combination with a UAV. The underlying principle is that most of the defects in a PV module generate heat under sunlight. These defects are visible in TIR images as increased temperature compared to a healthy cell. However, it is not possible to distinguish different defects, such as cracked cells or mismatched cells, based on heat generation. Therefore, it is often not possible to identify the exact origin of the defect based on a TIR image alone. In addition, cases of cracked cells and isolated regions have been observed, which are not visible as increased temperature on TIR images [7, 8].

An RGB camera detects reflected sunlight in the visible range. This camera can provide higher resolution than a TIR camera, and in that way, help identify the reason for defects detected on TIR images. This has been done in combination with a UAV inspection. However, the signal that the RGB camera detects enables identification of only those faults observable by the human eye [5, 9].

In addition to reflected sunlight in the visible range, RGB cameras can detect emitted radiation (fluorescence) from fluorophores upon excitation with ultraviolet (UV) light. Fluorophores are chemical compounds in polymeric lamination material in PV modules and are prone to degradation due to reaction with oxygen, in which case their fluorescence emission is weakened and is thus depicted with lower pixel values in images. In combination with imaging from UAVs, ultraviolet fluorescence (UVF) imaging poses some challenges [10]. The UAV needs to



carry the UV illumination source and the accompanying battery. At high flight altitudes, UV light and correspondingly the emitted fluorescence signal are very weak [8], while low altitudes have a negative effect on throughput. UVF imaging requires long exposure times due to the relatively low intensity of the emitted radiation, but low exposure times are favorable due to the vibration and moving of the UAVs. The inspection must be conducted in the dark due to the strong reflected sunlight in the visible range [10].

The electroluminescence (EL) imaging technique is based on detecting radiative band-to-band recombination in the semiconductor material emitted upon excitation with current. Areas with defects emit weaker radiation compared to healthy areas and therefore have lower pixel values. EL images have a greater level of detail and information than that can be obtained from the above-mentioned imaging techniques. EL imaging outdoors has traditionally been conducted in the dark or in very low light conditions, so that daylight does not interfere with the EL signal detection. In such conditions, EL imaging has been combined with UAVs. Daylight imaging procedures have also been developed in recent years. The major challenge with EL imaging is that the excitation of charge carriers requires forward biasing, which means connecting to the PV system [7, 8, 11–13].

An alternative to EL imaging is photoluminescence (PL) imaging. The two techniques are equivalent when it comes to detecting and locating electrical defects [7]. PL imaging is based on charge carrier excitation through photons, that is, an illumination source. As the information obtained from such images is comparable to that from EL images, it can be employed as their alternative [8] at the same time, as PL imaging does not have to be conducted at night when sunlight is used as an excitation source. However, all promising solutions presented thus far for high throughput daylight PL imaging require physical interference with the PV system, as is the case with EL imaging. Connecting to the PV system is either necessary to control its operating point (OP) as a means of filtering the reflected sunlight or to gain a complete insight into the extent of the PV modules' defects.

The contribution of this thesis is to investigate possibilities for a truly contactless PL imaging approach with sunlight excitation (i.e., without physical contact with the PV system) for the efficient inspection of PV power plants. The focus is on PL imaging under sunlight excitation. Therefore, the PL imaging approaches using

a light emitting diode (LED) [14] or a laser [15] as an excitation source are not addressed. As forecasts point to crystalline silicon (c-Si) PV as the most important world electricity source by 2040–2050 [16], this thesis focuses solely on PL imaging of c-Si modules.

## 1.2 Research question and objectives

Based on the background above, the research question that this thesis aims to answer is as follows: How can PL imaging with sunlight excitation be conducted on as large a PV area as possible with as little interference as possible in the PV system?

The main objective of this research question is to enable PL imaging of several modules or strings simultaneously without having to physically connect to the PV system. This has been achieved in papers A and C. The method for PL image acquisition developed in Paper C resulted in more time-demanding data processing with a conventional algorithm for PL image processing. To develop the potential of this technique, an alternative algorithm, and thus an improved approach to data processing, was presented in Paper D.

Two subordinate objectives were developed during the course of work with this thesis. One was to investigate and compare information obtainable from PL images as opposed to EL images. This was conducted in papers B and E. The other objective was to broaden the applicability of the developed methods for PL imaging under sunlight excitation away from only clear sky and direct illumination conditions to imaging under diffuse irradiance. This was done in Paper E.

## 1.3 Thesis outline

This thesis is divided into two parts. Chapter 2 elaborates on the theoretical background and contributions made thus far with respect to PL imaging with sunlight excitation. Chapter 2.1 presents the principal for PL imaging with sunlight excitation, that is, theoretical background for PL emission and spectroscopic considerations regarding PL signal detection. Chapter 2.2 explains the current state of development with respect to PL imaging with sunlight excitation. Dif-

ferent aspects of the proposed methods are described to set the scene for the contributions presented in this thesis. Furthermore, this chapter elaborates on what is identifiable in PL images obtained based on different imaging procedures. An overview of the main aspects of the developed methods is presented in Chapter 2.3.

The second part of the thesis, Chapter 3, presents the contributions made in the thesis. Chapters 3.1 and 3.2 elaborate on the two proposed procedures for detecting PL signal in daylight. The former is based on papers A and B and the latter on papers C through E. Chapter 3.3 puts the contributions of this thesis in the context of related studies, before an outlook is given in Chapter 3.4, suggesting possible future challenges.



# Chapter 2

## Background

### 2.1 Photoluminescence emission and detection from silicon material in daylight

Radiative band-to-band recombination in silicon (Si) material originates from the de-excitation of charge carriers from the conduction band to the valence band. A photon, whose energy corresponds to the band gap energy of Si, is emitted upon recombination. The signal emitted from the Si material upon de-excitation is called photoluminescence if the excitation before it takes place with photons (i.e., an illumination source). The intensity of photoluminescence  $I_{PL}$  can be expressed as

$$I_{PL} = Cn_i^2 \exp\left(\frac{eV_d}{kT}\right), \quad (2.1)$$

where  $C$  is a proportionality factor that accounts for the optical properties of the sample,  $n_i$  is the intrinsic carrier density,  $e$  is the elementary charge,  $V_d$  is the diode voltage,  $k$  is the Boltzmann constant and  $T$  is the temperature [17].

The two conditions for emission of the minimum and maximum intensity of the PL signal are illustrated in the current-voltage (IV) characteristics in Fig. 2.1. As the intensity of the signal is proportional to the exponential of the diode voltage, the highest signal intensity is achieved in the open-circuit (OC) condition in which there is no current extraction. The lowest signal intensity can be measured in

the short-circuit (SC) condition, when the current extraction is at its maximum. Thus, unless one needs to extract current during PL signal detection, this type of imaging is performed in the OC condition, without any contact with the sample, on both Si bricks, as-cut wafers and solar cells [17].

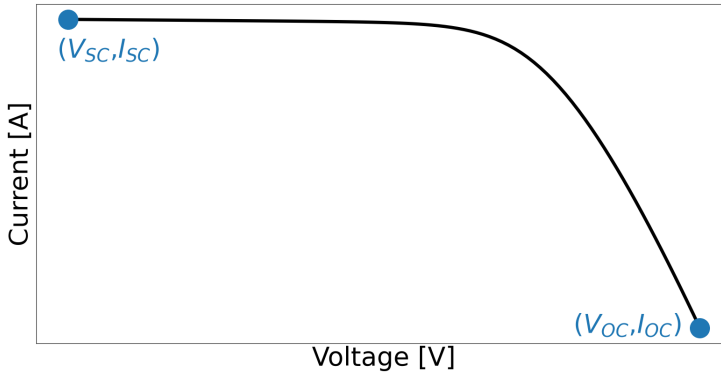


**Figure 2.1:** IV curve illustrated with the two points in which the intensity of the PL signal is at its minimum, the SC condition, and at its maximum, the OC condition.

Detection of the PL signal from Si can be performed with a light source, which illuminates the material and excites the charge carriers, and a camera or a spectrometer, which detects the emitted luminescence. A camera provides the spatial resolution of the signal as opposed to the point measurement obtained with a spectrometer. Depending on the wavelength range of the camera detector and the excitation source, the camera might detect the reflected light from the excitation source in addition to the PL signal. In a controlled laboratory setting, the experiment is designed in such a way that the reflected light and the emitted PL signal do not overlap spectrally. In this case, it is possible to filter out the former with optical filters [18]. When imaging field-deployed modules in daylight, the spectral range of the reflected sunlight and the emitted PL signal overlap. This is illustrated in Fig. 2.2. Although the solar irradiance in the wavelength range in which the PL signal is emitted is weakened when it reaches the Earth's surface due to water absorption in the atmosphere, the irradiance is still orders of magnitude stronger when reflected from the modules compared to the PL signal.

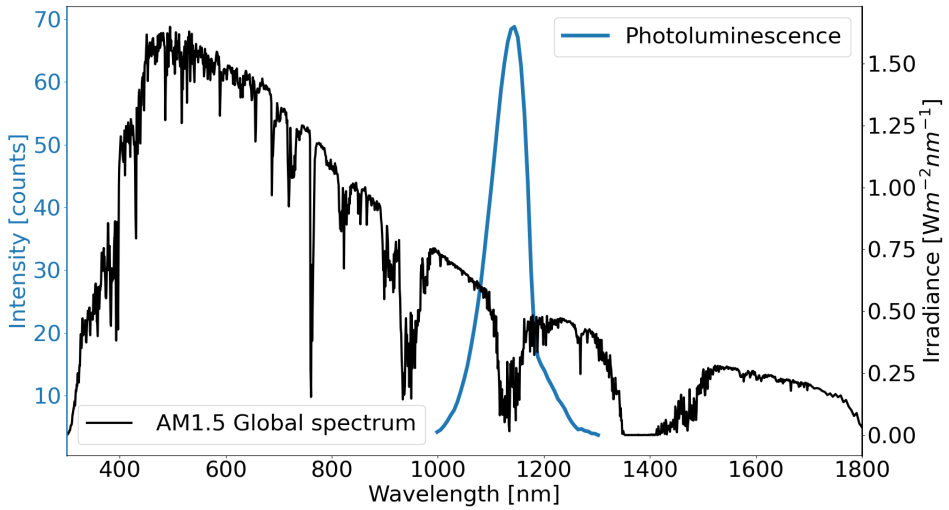


**Figure 2.2:** The AM1.5 global spectrum [19] overlaid with the PL signal detected from a Si solar cell in a controlled laboratory environment with laser light excitation and a hyper-spectral camera.

The challenge regarding the separation of two spectrally overlapping signals is translated to average pixel values, as illustrated in Fig. 2.3. The camera detector registers the total signal, which is the sum of the reflected sunlight and the emitted PL signal. If a camera is placed in front of a module in operation under constant irradiance, that is, in clear sky conditions, and a series of images is acquired, the PL signal and reflected solar irradiance are two constant signals detected over time. The PL signal is almost nonexistent compared to the high intensity of the reflected solar irradiance. The total signal is shifted upwards only slightly from the reflected solar irradiance signal due to the PL emission. Based on this image series, it is not possible to know what proportion of a pixel value is due to the reflected solar irradiance or the PL signal.

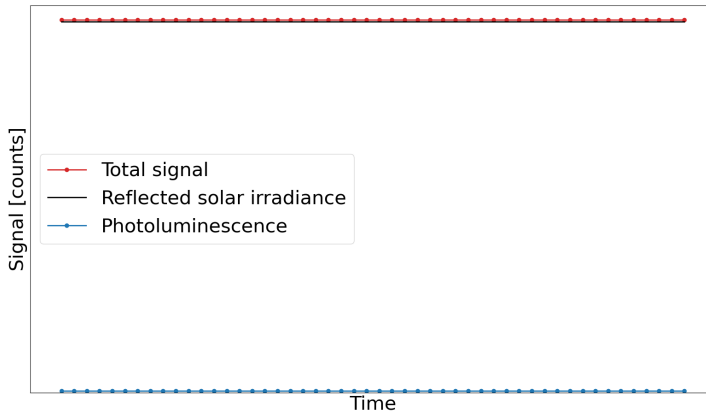


**Figure 2.3:** Signal intensity from PV modules detected with a series of images during constant illumination is translated into the average pixel count over time. It shows the total signal detected and its constituent parts, the reflected sunlight and the PL signal.

## 2.2 Photoluminescence imaging of PV modules in daylight

Different solutions have been proposed for elimination of the reflection and extraction of the emitted signal due to the spectral overlap of the wavelength range in which the PL signal is emitted, and the light from the excitation source is reflected. The methods can be divided into two groups: manipulating the PV system (i.e., control of the PV system's OP [20–29]) or filtering through optical filters [30,31]. In the following section, the two approaches are elaborated.

### 2.2.1 Control of the operating point

The PL signal can be separated from the total signal if it varies in a controlled way while the reflected solar irradiance remains constant. This is the essence of the lock-in technique. The technique is used for signal amplification and evaluation against a noisy background and is based on periodically pulsed amplitude modulation of the primary signal with a particular frequency [21,32]. This is illustrated in Fig. 2.4. The primary signal is the PL signal, which is modulated between low and high amplitudes,  $PL_1$  and  $PL_2$ . The background signal is the reflected



sunlight,  $R$ , assumed to be constant between the two modulation conditions.

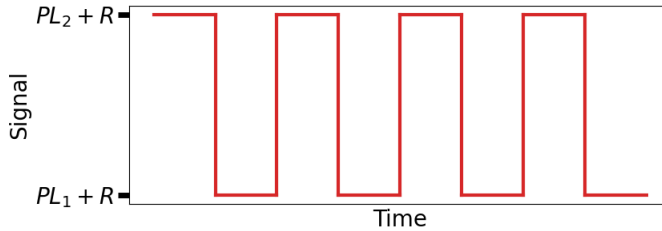


**Figure 2.4:** The total signal consisting of the PL signal and reflected sunlight,  $R$ , can be detected over time with high and low intensity due to pulsed amplitude modulation of the PL emission from PV modules. The PL signal has high intensity,  $PL_2$ , and low intensity,  $PL_1$ . Reflected sunlight,  $R$ , is assumed to be constant.

Four repetitions of the two modulation states are depicted in Fig. 2.4, during which eight images can be acquired. The total signal detected in each image is shown in Fig. 2.5 as the average pixel count over time. Compared to Fig. 2.3, it is clear that the PL signal, and therefore the total signal, varies in intensity up and down from image to image. The variation of the PL signal between two levels makes it possible to identify how much of the total signal is the PL signal in the high state,  $PL_2$ , compared to the low state,  $PL_1$ .

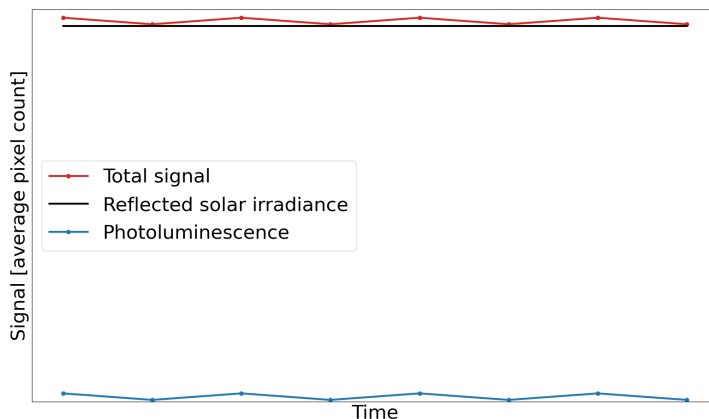


**Figure 2.5:** The PL signal, reflected solar irradiance and the total signal detected by a camera during lock-in modulation.

The difference between an image pair should, in theory, consist of only the difference in the PL signal,  $\Delta PL$ , as the reflected solar irradiance is assumed to remain constant during imaging. Subtracting an image with lower PL signal intensity from an image with higher PL signal intensity enables extraction of the  $\Delta PL$  signal and elimination of the reflected solar irradiance. However, the  $\Delta PL$  signal obtained with only one image pair is weak, and the method for signal enhancement is based on averaging to obtain the final  $\Delta PL_{OP}$  image according to

$$\Delta PL_{OP} = \frac{1}{N} \sum_{i=1}^N (PL_{2i} + R_i) - (PL_{1i} + R_i), \quad (2.2)$$

where  $N$  is the number of images obtained in each state.

Because the intensity of the PL signal is proportional to the exponential of the diode voltage, according to Eq. 2.1, the intensity of the PL signal can be controlled between a high and a low state by controlling the OP of the imaged modules. The subscript  $OP$  in Eq. 2.2 therefore represents the difference in the PL signal obtained based on images acquired in two different OPs. Control of the OP along the IV curve can be achieved with electrical or optical modulation. The assumption of constant reflected solar irradiance during imaging requires a fast, almost instantaneous, switching of the OP. Frequencies of 25 Hz and 30 Hz have been reported [23, 25].

Several solutions have been proposed that use electrical modulation of the OP. The first developed daylight luminescence imaging procedure is based on a patented DaySy imaging system consisting of a DaySyBox and the imaging apparatus [21]. The box can be connected to up to six strings or a power source to modulate the system between the SC, maximum power point (MPP), OC and forward direction conditions. It is possible to conduct EL imaging in daylight and at night as well as daylight PL imaging. With this approach, a  $\Delta PL_{OP}$  image is obtained between images collected in two pre-chosen OPs [8, 20, 22].

The lock-in technique with electrical modulation can be implemented in other ways as well. The OP of one module can be controlled with a modulator that uses a metal-oxide-semiconductor field-effect transistor (MOSFET) as a switch. A programmable DC load in combination with a MOSFET makes it possible to choose the OPs on the IV curve more freely [23]. Another study uses a solid-state relay for switching a module between the OC and SC conditions [24]. At the string

level, one can apply manual switching of one or several strings through a combiner box. In this way, the OP of the string can be switched between the MPP and the OC [29].

Optical modulation has been proposed to avoid interfering with the electrical connections of the modules or strings. Optical modulation is based on controlling the OP of a sub-string in a module by covering one of its cells with an LED. By doing so, the amount of shading on that one cell, and thus the extracted current for all the cells in the sub-string connected to the same bypass diode, is controlled. The switching can be performed between the OC condition by completely shading one cell (0 Sun), in which case the bypass diode leads, and the SC condition by illuminating it with 1 Sun. This approach enables adjustment of the current in the sub-string to any level between the OC and SC conditions by adjusting the LED's intensity. The imaging is conducted at the sub-string level and by moving the LED from one sub-string to the next. The images are then stitched into an image of a whole module [25].

This approach has been tested on a module connected to a microinverter. In this case, it is possible to switch the OP of the entire module by controlling the current through one cell. It was investigated how power electronics affects the almost instantaneous switching. It is found that the particular inverter has a reaction time of 6 s when switched from the OC condition to the MPP condition. Because of the changes in irradiance that could take place during this switching time, the sequential switching method, as illustrated in Fig. 2.4, is not applicable, and the batch measurement approach was proposed [26]. This approach is illustrated in Fig. 2.6. During each of the two states of PV module emission, an image series is acquired. The OP is switched at time  $t_1$ , and the new operating condition is reached at  $t_1 + 6$ . As the irradiance might change in the meantime, it is no longer assumed to be constant and is called  $R_1$  and  $R_2$  in Fig. 2.6. A correction due to the changing reflected solar irradiance was proposed. The images acquired in each state are averaged. The averaged image with the lower PL signal is subtracted from the averaged image with the higher PL signal [26].

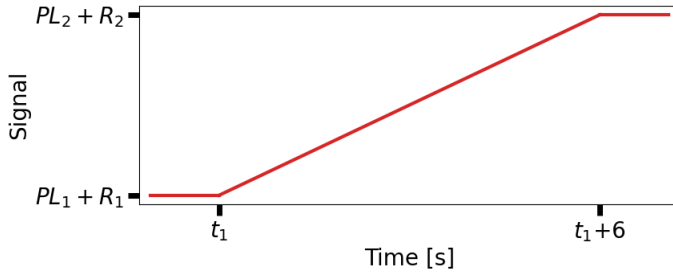


**Figure 2.6:** The total signal consisting of the PL signal and reflected sunlight as a function of time when the lock-in technique is performed on a PV module connected to a microinverter. The inverter has a reaction time of approximately 6 s [26]. The reflected solar irradiance can no longer be assumed to be constant and is called  $R_1$  and  $R_2$ . The shape of the line between the two states does not illustrate the level of the total signal during the inverter’s reaction time but is drawn to illustrate the length of the time compared to instantaneous switching in Fig. 2.4.

The approach with optical modulation was extended to enable a higher throughput by developing an optical modulator consisting of several LEDs. The modulator can cover the necessary number of cells in several modules to switch the OP at the string level. The proposed method controls the OP of five modules in a string of 28 modules. The assumption is that the five modules in the OC condition will force the remaining 23 modules to increase their voltage because the string voltage is fixed by the PV plant design. The increase in voltage by the remaining modules will be around 18%, which is enough to force these modules in the OC condition and thus increase the PL signal emission. The underlying assumption is that a PV array may consist of 200 or more module strings connected in parallel. Modulating one such string will affect the array current by less than 0.5% and thus will not cause the inverter’s OP to change significantly [27].

Although the approaches for electrical and optical modulation described thus far are used for filtering the reflected sunlight according to Eq. 2.2, the camera apparatus also needs to be used in combination with an optical band-pass filter. Such a filter is used to decrease the intensity of the reflected sunlight, which is being detected. The studies described thus far use a short-wave infrared camera with an indium gallium arsenide (InGaAs) detector. The spectral range, in which these cameras can detect, is illustrated in Fig. 2.7 based on one of the cameras that

were used during the work on this thesis. The Raptor Photonics Owl 640S with an InGaAs detector is able to detect radiation in the spectral range of 900–1700 nm. The peak of the PL signal is around 1140 nm [17]. The filter mounted on it covers the range of 1125–1175 nm and has a center wavelength (CWL) at 1150 nm. Omitting optical filters would result in the detection of the reflected sunlight in the wide spectral range of the camera. This would result in saturation of the total detected signal during imaging in bright daylight. Band-pass filters are used in combination with electrical and optical modulation to narrow down the spectral range of interest and therefore the amount of detected reflected sunlight.

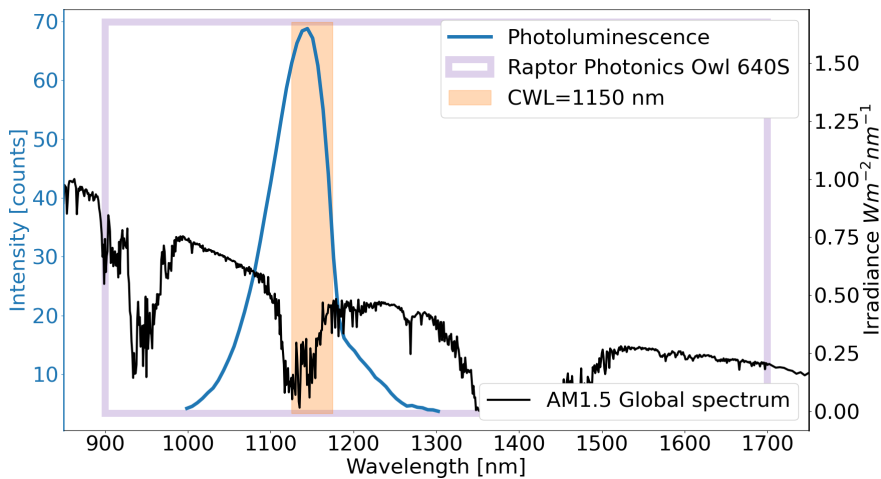


**Figure 2.7:** The AM1.5 global spectrum [19] and the PL signal shown in the spectral range of 850–1750 nm. The purple and orange squares indicate the spectral range of the Raptor Photonics Owl 640S and the accompanying filter, respectively.

## 2.2.2 Optical filtering

Two approaches to optical filtering have been proposed thus far. The approaches do not require connection to the PV system to separate the reflected sunlight from the PL signal.

The first approach is described in Fig. 2.8. Two images are acquired. One image is acquired with a band-pass filter with a CWL where the PL signal peaks at around 1135 nm. This is also the spectral region in which the water vapor absorbs. In this

way, the ratio between the emitted PL and the reflected sunlight is maximized. The other image is acquired with a band-pass filter in the spectral region where the PL signal is weak, either around 1050 nm or 1200 nm. These two filters are chosen so that almost no PL signal is detected in their spectral ranges at the same time as the ambient reflected signal is similar to that detected with the first filter [30].

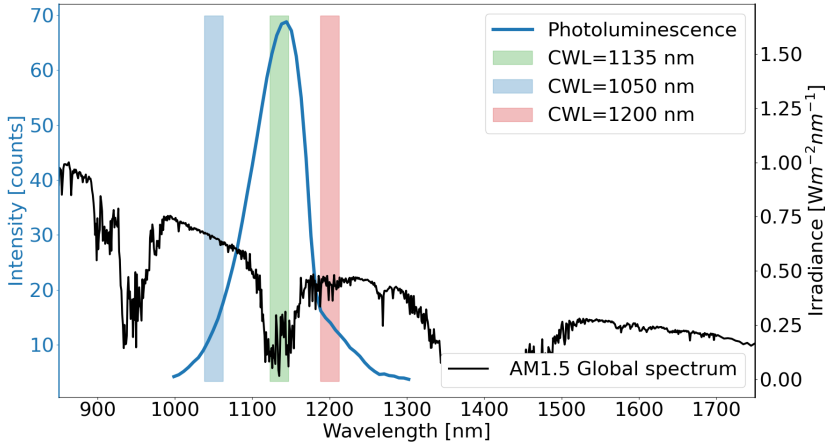


**Figure 2.8:** The AM1.5 global spectrum [19] and the PL signal are shown in the spectral range of 850–1750 nm. The green, blue and red squares indicate the spectral range of three band-pass filters with their CWLs as used in [30].

A difference image is obtained between the image with high PL signal intensity and one of the images with low signal intensity,  $\Delta PL_S$ . The subscript  $S$  indicates the difference in PL images based on different spectral ranges. It is found that  $\Delta PL_S$  obtained with the image in the 1200 nm region gives better results. The authors claim that it is because the reflected solar irradiance in that part of the Sun’s spectrum changes less than in the spectral region around 1050 nm. The imaging was performed in the OC condition, but it should be possible to perform imaging during regular operation of field-deployed modules in the MPP condition. The challenge in that case will be that the PL signal will be up to 20 times weaker. The method is particularly suitable for high-efficiency modules because they have a relatively high ratio of the PL signal to the reflected sunlight [30].

The other approach for PL imaging, which uses optical filtering, is based on ultranarrow band-pass filters. In the spectral range 1134.5–1135.3 nm, the water

vapor absorption in the atmosphere is so strong that almost none of the Sun's radiation reaches the Earth. The ultranarrow band-pass filters cover a bandwidth of 0.34 nm, with the CWL at 1134.98 nm. Almost no reflected sunlight is detected through such filters. A single PL image suffices because it is not necessary to conduct any subtraction to eliminate reflected sunlight. The PL images obtained in this way are referred to as  $PL_U$ , where the subscript  $U$  stands for ultranarrow. This approach is illustrated in Fig. 2.9. In addition to the ultranarrow band-pass filter, a long-pass and a short-pass filter are used to further reduce the unwanted reflected solar irradiance being detected below 1000 nm and above 1400 nm.

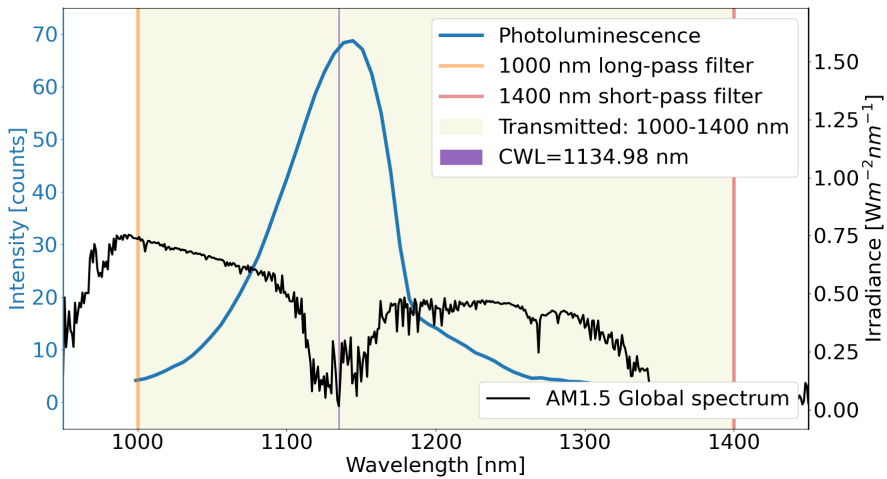


**Figure 2.9:** The AM1.5 global spectrum [19] and the PL signal are shown in the spectral range of 950–1450 nm. The yellow square indicates the spectral range (1000–1400 nm) in which the signal passes through the filter system based on the combination of a long-pass and a short-pass filter. The thin purple line indicates the spectral range in which the ultranarrow band-pass filter transmits [31].

Several interesting PL imaging aspects originate from this imaging method. The PL signal intensity has been found to decrease with increasing distance due to its absorption by water vapor on its way from the module to the camera detector. The optical absorption length in the spectral range is 12 m [7, 31]. Depending on the application, this method requires long acquisition times. To obtain high-quality images displaying micro-cracks in the OC condition, an acquisition time of 20 s and 50 s was used with a heterojunction (HJT) module ( $V_{OC} = 735$  mV/cell)

and a passivated emitter and rear contact solar cell (PERC) module ( $V_{OC}= 686$  mV/cell), respectively. For reliable defect detection, an exposure time of 1 s can also be used during imaging of PERC modules [31]. Moreover, regarding image quality, a considerable area around the  $PL_U$  image edges is blurry because of the custom-designed imaging optics [7]. Concerning the investigation of series resistance-related defects, it is necessary to acquire  $PL_U$  images during current extraction. To do that, control of the OP is needed. The use of optical modulation with LEDs is proposed [31], as described above.

### 2.2.3 Interpretation and types of photoluminescence images

The approaches presented above can be visualized, as shown in Fig. 2.10. When PL image acquisition is conducted with the Sun as the excitation source, approaches for eliminating reflected solar irradiance can be implemented in two ways. One group of approaches uses the PV system, more precisely, control of the OP, while the other uses an imaging apparatus. The arrows in Fig. 2.10 represent the studies described in the two preceding sections. They point from the image acquisition step, comprising elimination of reflected solar irradiance, toward the image processing step.

The two different approaches result in three types of PL images. Acquisition of image pairs during modulation of the OP results in a  $\Delta PL_{OP}$  image, which is a difference image obtained between two images acquired in the same spectral region (Fig. 2.7), but in different OPs. The approach with two band-pass filters, illustrated with Fig. 2.8, results in a difference image,  $\Delta PL_S$ , obtained between two images acquired in two different spectral regions but in the same OP. The approach based on ultranarrow band-pass filters (Fig. 2.9) results in only one  $PL_U$  image. This is the case regardless of whether it is obtained under different levels of current extraction (i.e., controlling the OP) or not, as indicated with arrows in Fig. 2.10.



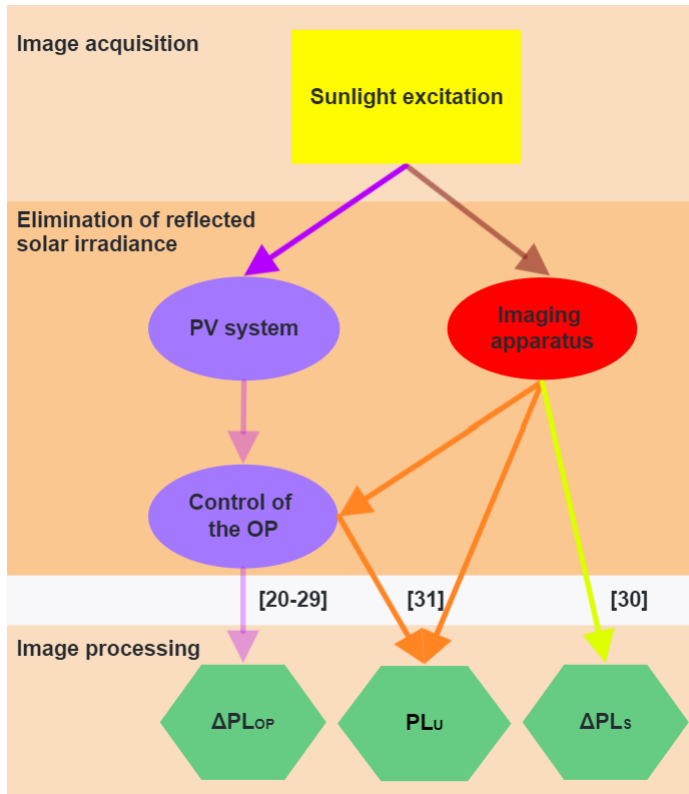


**Figure 2.10:** Two types of solutions for daylight PL imaging and elimination of sunlight are shown with the resultant three types of PL images. The arrows point toward the different steps from the image acquisition stage to the image processing stage. The studies are referenced next to the arrows.

The question arises which faults are visible and how they appear in the three types of images. It is important to emphasize that some faults are visible only if the resolution is sufficient. For example, for micro-cracks to be apparent, the imaged area must be smaller than one entire module. It has been reported that 1/5 of a module (2 x 6 cells [25] or 3 x 4 cells [20]) has been imaged for this type of fault to be visible.

In general, outdoor PL imaging with sunlight excitation is a fairly new approach for fault detection in field-installed PV modules. Information about what kinds of defects are visible in such images is still limited. The study on PL imaging

with two band-pass filters is a small study in which a  $\Delta PL_S$  image of a few cells is displayed. The  $\Delta PL_S$  images are expected to display the same information as  $\Delta PL_{OP}$  images, that is, the difference between the two PL intensity levels. The visible defects in  $\Delta PL_S$  images are cracks [30]. The  $PL_U$  images in the study on ultranarrow band-pass filters show cracks and isolated regions [31]. The studies in which  $\Delta PL_{OP}$  images are obtained have shown that cracks and isolated regions [20, 23–26, 29], bypass diode failure [8, 26], potential induced degradation (PID) [8, 33], fragmented glass [34] and light and elevated temperature-induced degradation (LeTiD) [34] are identifiable.

Cracks and isolated regions (i.e., areas with increased series resistance) are the type of failure that has been addressed most often. It is important to clarify how isolated regions appear in  $\Delta PL_{OP}$  compared to  $PL_U$  images. EL images are used as a reference point.  $\Delta PL_S$  images are not included in this comparison because there is not enough literature on this subject. Three types of regions are illustrated in the EL image obtained with the SC current,  $EL_{SC}$ , in Fig. 2.11(a). Region A is intact, region B is partly isolated and region C is completely isolated. Three colors are used to mark the three levels of pixel intensity in each region. A region of high pixel values is yellow, medium pixel values are red and low pixel values are black, due to the high, medium and low levels of recombination, respectively.

If a  $PL_{U1}$  image is obtained in the OC condition [31], Fig. 2.11(b), all three regions will have high-intensity PL signal emission. The level of isolation of a region in a  $PL_U$  image is visible if the current is extracted during imaging [26, 31], as illustrated with a different color distribution regarding the  $PL_{U2}$  image in Fig 2.11(c). In this case, the highest level of current density is extracted from region A [26]. Consequently, the recombination level in region A is the lowest of the three regions, and it has the lowest pixel values. No current is extracted from region C. Recombination there remains unchanged, and the pixel values remain as high as in the  $PL_{U1}$  image. Controlled current extraction can, in this case, be achieved through modulation of the OP with LEDs, as mentioned above and illustrated with arrows in Fig. 2.10.

To obtain a  $\Delta PL_{OP}$  image, two constituent images are needed,  $PL_2 + R$  and  $PL_1 + R$ , as shown in Fig. 2.11(d) and (e). They are acquired under the same

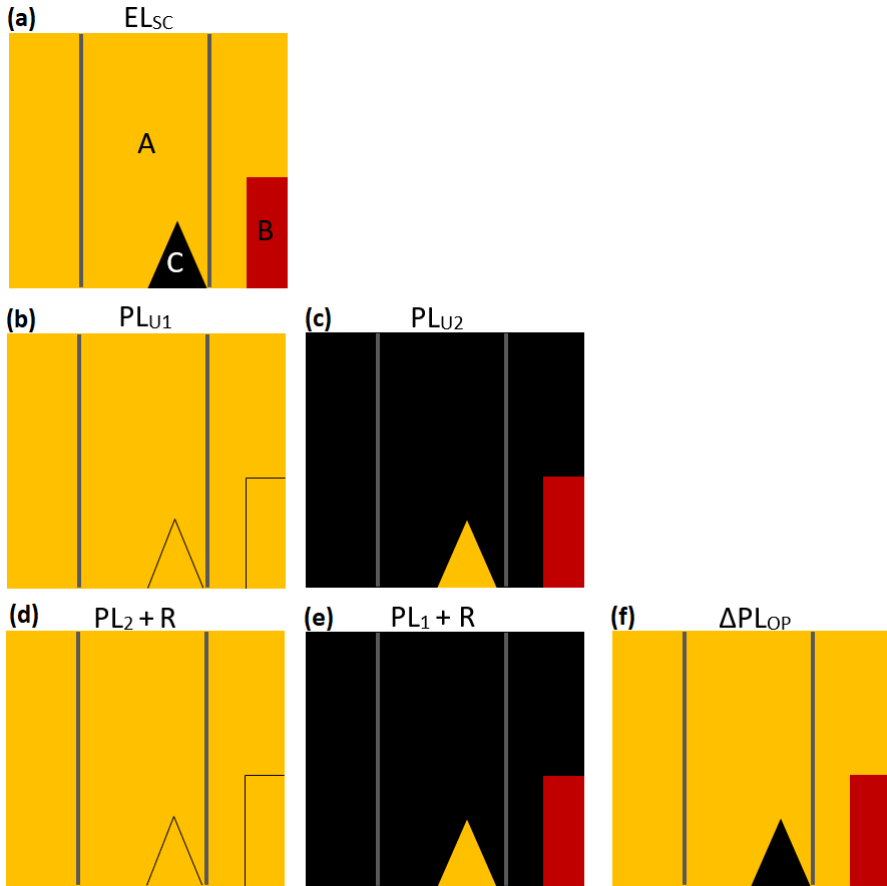


**Figure 2.11:** An intact region, A, a partly isolated region, B, and a completely isolated region, C, are shown with the highest, medium and lowest pixel intensity levels in yellow, red and black, respectively, in an  $EL_{sc}$  image (a). A  $PL_{U1}$  image obtained in the OC condition (b), a  $PL_{U2}$  image obtained under current extraction,  $PL_2 + R$  and  $PL_1 + R$  images (d) and (e) obtained under the same conditions as the two preceding images, and a  $\Delta PL_{OP}$  image (f) obtained after subtraction of  $PL_1 + R$  from  $PL_2 + R$ .

conditions as  $PL_{U1}$  and  $PL_{U2}$ , and thus, the intensity of the PL signal is the same as in Fig. 2.11(b) and (c). However, the reflected solar irradiance values are entailed in  $PL_2 + R$  and  $PL_1 + R$  on top of the PL signal, and the variation in pixel values in Fig. 2.11(d) and (e) is not visible in reality. The  $\Delta PL_{OP}$  image, Fig. 2.11(f), displays pixel values, which are the difference of  $PL_2 + R$  and  $PL_1 + R$ . The color distribution in the  $\Delta PL_{OP}$  images is generally similar to that in the EL images.

Four  $PL_U$  [31] and five  $\Delta PL_{OP}$  [26] images obtained under different levels of current extraction have been used to analyze the level of isolation of a cell region. It has been demonstrated that two different  $\Delta PL_{OP}$  images do not necessarily show that a region is isolated. This depends on the level of current extraction and the degree of isolation of a region [26]. In the case of  $PL_U$  images, a new image can be obtained every time when the level of current extraction is changed [31]. In the case of  $\Delta PL_{OP}$  images, a new round of modulation of the OP is needed to obtain a new  $\Delta PL_{OP}$  image, as illustrated in Fig. 2.12. The original lock-in modulation, as shown in Fig. 2.4, is again displayed in Fig. 2.12(a) for the sake of comparison with modulation when the  $PL_1$  state is shifted due to another level of current extraction, as shown in Fig. 2.12(b). The images acquired during modulation in the latter case will have a smaller  $\Delta PL$  value due to the smaller current difference between the  $PL_1$  and  $PL_2$  states. The equipment used for modulation of the OP presented above must allow different levels of current extraction for more than two  $\Delta PL_{OP}$  images to be obtainable. This is the case with the DaySy system [20], MOSFET with a programmable DC load [23] and LEDs (optical modulator) [26, 27].

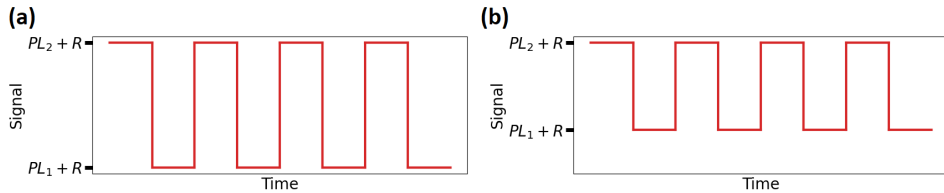


**Figure 2.12:** Lock-in approach from Fig. 2.4 in which the PL signal is modulated between two levels (a) is used for comparison with modulation when the  $PL_1$  state is set to another point on the IV curve (b). The new  $PL_1$  point is closer to the  $PL_2$  level, meaning that the current levels in (b) are closer to each other than in (a).

Finally, the aspect regarding quantitative versus qualitative methods for PL image analysis should be addressed. PL images are analyzed qualitatively, which means that it is possible to detect, identify and count defects if the PL image quality is sufficiently high. Quantitative analysis is not possible because of the level and variability of sunlight intensity and camera settings. However, advances have been made in the quantitative analysis of indoor EL images, connecting the intensity of the detected EL signal to electrical parameters. It can be expected that this knowledge will eventually be transferred to outdoor measurements [7, 8].

## 2.3 Overview of the main aspects of daylight photoluminescence imaging of PV modules

An overview of all the mentioned PL imaging approaches and five aspects that characterize them is shown in Table 2.1. They are chosen because of their relevance for comparison with the contributions presented in this thesis. They are the excitation intensity as described or measured in each study, the equipment which is necessary to enable elimination of sunlight, the PV area size that can potentially be imaged and that is conditioned by the equipment, whether control of the OP is necessary or not, and the type of PL image that results from each method.

The last two aspects are specified in Table 2.1. Control of the OP is specified depending on how many points on the IV curve it can be achieved in conditioned by the equipment. In some cases, modulation between two or three points ( $\leq 3$ ) is possible, while some types of solutions enable modulation along the IV curve ( $> 3$ ). A distinction has also been made regarding whether the modulation is either instantaneous (i) or delayed (d). In the last column, how many  $\Delta PL_{OP}$ ,  $\Delta PL_S$  or  $PL_U$  images can be obtained per image series is specified. An image series is defined as a series of images acquired without having to pause to change camera or PV system settings. Regarding the approach with the lock-in technique, modulation of the OP between two conditions is considered to result in one image series because once the modulation and imaging have started, there is no need to pause and interfere. The approach with two band-pass filters requires a change of filters and therefore two image series to obtain one  $\Delta PL_S$  image.

**Table 2.1:** Main aspects of PL imaging of field-deployed modules with sunlight excitation.

Study	Excitation intensity [ $Wm^{-2}$ ]	Additional equipment	PV area size	Control of the OP ( $\leq 3$ OP: $\leq 3$ IV curve: $> 3$ instantaneous: i delayed: d)	Image type (No. of images/ one image series)
[20]	sun (>80)	DaySyBox	6 strings	yes ( $\leq 3, i$ )	$\Delta P_{LOP}$ (1)
[23]	sun	MOSFET + DC load	module	yes ( $> 3, i$ )	$\Delta P_{LOP}$ (1)
[24]	sun (>260)	solid-state relay	module	yes ( $\leq 3, i$ )	$\Delta P_{LOP}$ (1)
[29]	clear sky	combiner box	several strings	yes ( $\leq 3, d$ )	$\Delta P_{LOP}$ (1)
[25]	full sunlight	LED	sub-string	yes ( $> 3, i$ )	$\Delta P_{LOP}$ (1)
[26]	full sunlight	LED +inverter	module	yes ( $> 3, d$ )	$\Delta P_{LOP}$ (1)
[27]	full sunlight	optical modulator	string	yes ( $> 3, i$ )	$\Delta P_{LOP}$ (1)
[30]	full sunlight	two band-pass f.	several strings	no	$\Delta P_{LS}$ ( $< 1$ )
[31]	full sunlight	ultranarrow band-pass f. (+LEDs)	several strings (string)	no  yes ( $> 3, i$ )	$PL_U$ (1)

# Chapter 3

## Publications

### 3.1 Remote control of the operating point

#### 3.1.1 Development of the imaging method: Paper A

The PL imaging methods proposed before Paper A was written enabled imaging at either the sub-string [25] and module levels [23,24,26] or, if imaging was enabled at the string level, a specially developed piece of equipment connected to a string was required [20], as shown in Table 2.1. The contribution of the work presented in Paper A was to be PL imaging at the string level without the need to connect physically to the PV system.

The idea to use the string inverter was based on the approach using optical modulation with an LED, during which the module under investigation was connected to a microinverter [26]. In Paper A, conducting the modulation of the OP directly through the string inverter by establishing communication with it through communication protocol Modbus TCP is proposed. This approach can be conducted with a WiFi connection. In this way, it is possible to modulate the OPs of several strings simultaneously. The approach can modulate the OP along the IV curve between the MPP and OC conditions. Due to the string inverter's reaction time of 5.5 s, image acquisition with delayed modulation, according to Fig. 2.6, was used as a starting point.

The approach was first demonstrated on one module. A ground truth image for validation was obtained with instantaneous MOSFET modulation [23]. However, a programmable DC load, which would enable modulation between the OC and MPP conditions, in the same way as the string inverter, was not available. Therefore, the MOSFET modulation was possible only between the OC and SC conditions. This posed a problem for the validation step, because a  $\Delta P_{LOP}$  image between the OC and SC conditions does not have the same signal intensity as an  $\Delta P_{LOP}$  image between the OC and MPP conditions.

A way to circumvent this inconsistency was to obtain a ground truth image with the instantaneous MOSFET modulation between the OC and SC conditions, allowed by the equipment set-up, and to simulate the inverter delay by building it into the software that controlled the MOSFET. In this way, the effect of the 5.5 s delay on the  $\Delta P_{LOP}$  images between the SC and OC conditions could be examined. Several rounds of data acquisition were conducted. It was observed that the correspondence was not very good between the ground truth image, called  $\Delta P_{LOP_{GT}}$  in Fig. 3.1(a), and images obtained with the simulated delay, shown as  $\Delta P_{LOP_{1SIM}}$  and  $\Delta P_{LOP_{2SIM}}$  in Fig. 3.1(b) and (c). However, if the two simulated images were averaged, as displayed in Fig. 3.1(d), the correspondence with the ground truth image was improved considerably.

This led to the adjustment of the approach, illustrated in Fig. 2.6, regarding image acquisition, as illustrated in Fig. 3.2. As the MPP condition is the state in which the string operates when the imaging starts, and it is the condition in which the string needs to return to, image acquisition with low PL signal intensity can be conducted two times. This results in two sets of images with low PL intensity and one set with high PL signal intensity. Obtaining two averaged images with low intensity results in two  $\Delta P_{LOP}$  images,  $\Delta P_{LOP_1}$  and  $\Delta P_{LOP_2}$ , which can be averaged into a final  $\Delta P_{LOP}$  image.



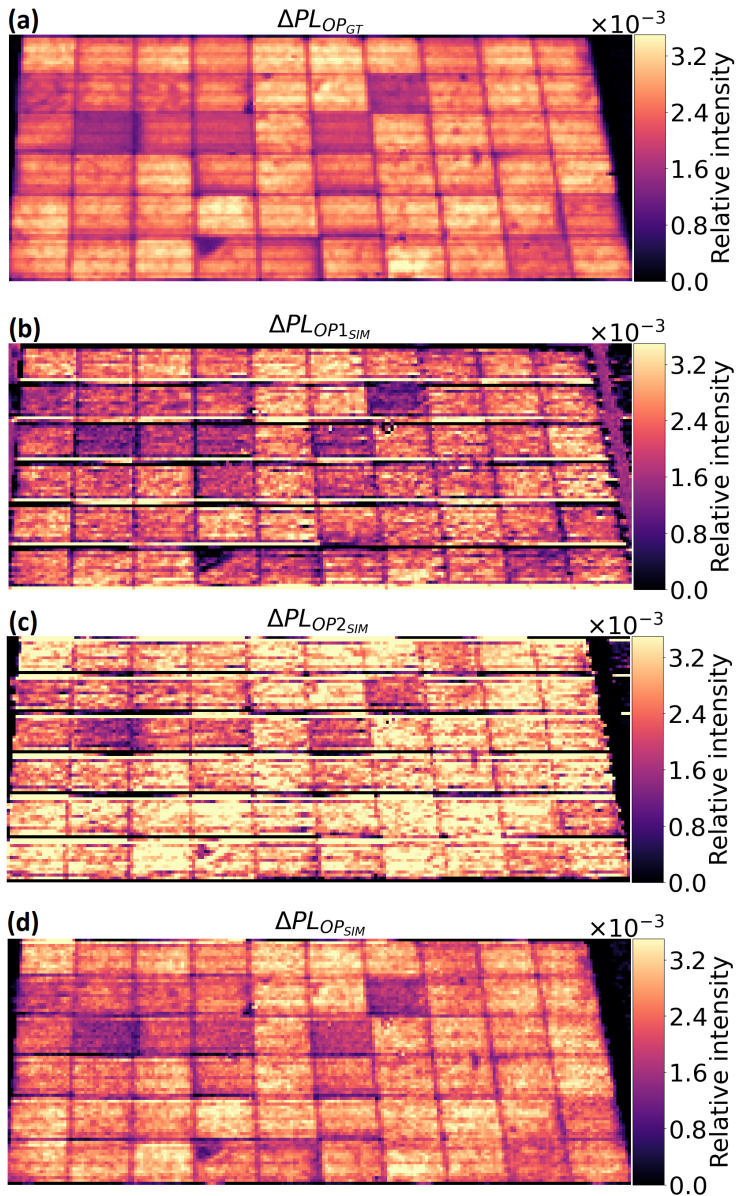


**Figure 3.1:** Ground truth image obtained with almost instantaneous MOSFET modulation between the OC and SC conditions (a), images obtained with simulated inverter modulation carried out with a delay of 5.5 s introduced in the MOSFET modulation between the OC and SC conditions (b) and (c) and the average of the two simulated images (d).

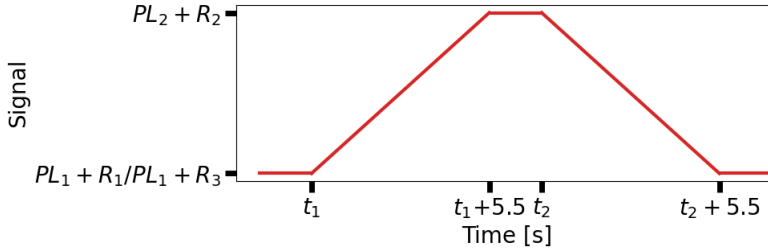


**Figure 3.2:** Modified modulation approach from Fig. 2.6 designed to collect images during two low states of the PL signal. The reaction time of the string inverter is 5.5 s from the moment the switching is initiated at  $t_1$  and  $t_2$ .

Although averaging over  $\Delta PLOP1_{SIM}$  and  $\Delta PLOP2_{SIM}$  images (Fig. 3.1(b) and (c)) results in a final  $\Delta PLOP_{SIM}$  image (Fig. 3.1(d)) with better correspondence with the ground truth image (Fig. 3.1(a)), the method still does not guarantee that conducting only one round of image acquisition between the SC, OC and SC conditions provides satisfactory results. Approximately 40 rounds of simulated modulation were conducted between these two conditions, resulting in approximately 20  $\Delta PLOP$  images obtained with three consecutive image sets, out of which one with good correspondence with the ground truth image was presented in Paper A. The same number of rounds of imaging were also conducted with the inverter modulation between the MPP, OC and MPP conditions because great variation in signal intensity was observed there as well.

It was suggested during the review process of Paper A that the  $V_{OC}$  of the modules plays an important role. The modules used in Paper A are aluminum back surface field (Al-BSF) modules. Therefore, it is expected that the procedure is more reliable when imaging modules with higher  $V_{OC}$ . Unfortunately, the method was never tested on the PERC bifacial modules, which were installed on our test site on a later occasion, and the method remained at the proof-of-concept stage. In general, it can be said that the image acquisition time prolonged by the inverter delay of 5.5 s is a considerable drawback of this method.

### 3.1.2 Defect analysis: Paper B

Before Paper B was written, a new InGaAs camera with a resolution of 640 x 512 was acquired compared to the one used in Paper A with a resolution of 320 x 256. In addition to better resolution, the available exposure times were considerably lower. While the Xenics camera offered a frame rate up to around 20 Hz, the highest frame rate selectable for the Raptor camera was 300 Hz. Another round of images was collected by controlling the string's OP with wireless communication. The goal was to investigate whether the images would benefit from the new camera with respect to the challenges described. Unfortunately, the same challenges were encountered, and shorter exposure time did not help in obtaining more concise  $\Delta PL$  intensity across the many  $\Delta PL_{OP}$  images.

Based on the images acquired with the new Raptor camera, an attempt was made in Paper B to analyze series resistance defects in a module based on  $\Delta PL_{OP}$  images obtained in the OC and SC and OC and MPP conditions. The nature of the defects was first assessed based on EL images obtained with SC current and with 10% of SC current [35]. Based on the two EL images, it was determined that one of the isolated regions had lower series resistance than the rest of the isolated regions. The same regions were analyzed based on the two  $\Delta PL_{OP}$  images to investigate whether it would be possible to make the same conclusion. However, the quality of the  $\Delta PL_{OP}$  image obtained between the OC and MPP conditions with inverter modulation was not sufficient to make such a conclusion despite the higher camera sensitivity.

## 3.2 Noninvasive photoluminescence imaging

### 3.2.1 Development of the imaging method: Paper C

Due to the unwanted effects of a long inverter reaction time with inverter modulation, we investigated whether there existed any other inverter functionality that would result in variation in current and therefore in a detectable change of the PL signal. For example, we tested, the variation in current around the MPP during normal operation, but that did not result in any noteworthy detection of a variation in the PL signal. With the improving PV technology and camera sensitivity, this might be possible in the future.

Eventually, we found a study that explored monitoring and fault detection based on IV curves obtained at the string level with string inverters [36]. We found that the string inverter installed on our test site, Fronius Primo 3.0, initiates IV curve sweeps on its own every 10 min for a global maximum power point search as part of its intelligent shade management system [37]. Other types of inverters can conduct IV curve sweeps on command through a smartphone application for monitoring purposes [38]. They can be initiated by the string inverter or by an operator and conducted at the plant, array or string level depending on the particular solution [37–40].

As the IV curve sweep initiated by the Fronius inverter was not controllable, we placed a camera in front of a module string and started to collect images. Current measurements were collected simultaneously for better insight into the IV curve sweep. However, none of this required any interference with the power production. The total signal detected from three bifacial modules of PERC technology is shown in Fig. 3.3. This method allows for the imaging of several strings simultaneously.

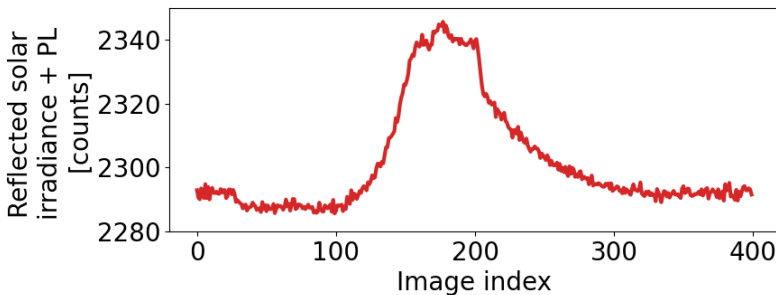


**Figure 3.3:** The total signal detected over 400 images from a module string during an IV curve sweep.

The signal in Fig. 3.3 reflects a continuous change in the current. This is a considerable advantage of PL imaging during IV curve sweeps because it can result in several  $\Delta P_{LOP}$  images obtained from different levels of current extraction. Compared to imaging based on the lock-in technique, which requires a new round of modulation to obtain a new  $\Delta P_{LOP}$  image (as explained with respect to Fig. 2.12), this method does not require more time to be invested to obtain another  $\Delta P_{LOP}$  image. Several  $\Delta P_{LOP}$  images are obtainable from one image set.

### 3.2.2 Alternative algorithm for extraction of the photoluminescence signal: Paper D

Using the lock-in technique for switching the OP results in two clearly distinct PL intensity levels and in unambiguous division of images into two groups at the image acquisition stage. This is an advantage of image processing with the subtraction method, Eq. 2.2, because it requires two groups of images with a clear difference in their signal intensities. Image processing can, in this case, be carried out in an unsupervised way in real time.

As PL imaging based on the string inverter's IV curve sweep results in a continuously changing PL signal, defining which image belongs to either the  $PL_1$  or  $PL_2$  state must be carried out after imaging. With a changing signal, it is not clear which image should belong to which PL intensity level. If one bears in mind that multiple  $\Delta PL_{OP}$  images obtained at different levels of current extraction are necessary to analyze defects related to series resistance, as addressed in Section 2.2.3, two new sub-sets must be defined several times. Data processing in this case is time-consuming.

This motivated us to search for and test a new approach for data processing based on the Pearson correlation coefficient (PCC) [41, 42]. The algorithm does not require the data set to be divided according to two PL intensity levels. An entire data set can be processed at once. Therefore, it is less time-consuming to process images collected during an IV curve sweep with the PCC algorithm than with the subtraction approach. The resultant image contains the PCC in every pixel and is called the  $PCC_{PL}$  image. It conveys the same information as a  $\Delta PL_{OP}$  image.

The PCC approach differentiates between a signal detected in a pixel that changes over time, such as the PL signal, and a signal detected in a pixel that does not change in the same way throughout an image set (Fig. 3.4(a)). This difference can be quantified as a measure of the linear similarity between every pixel in the image set and a reference signal. The reference signal is defined as the mean pixel count of every image in a data set. The idea is that the average image pixel count will show the development of the PL signal in the same way as the module pixels. Correlating a background pixel, showing only the development in reflected solar irradiance, with the reference signal will result in a low correlation value, as shown

in Fig. 3.4(b), while correlating a module pixel will give a high correlation value, as shown in Fig. 3.4(c). In this way, the module pixels (i.e., those that emit the PL signal) are segmented from the background pixels.

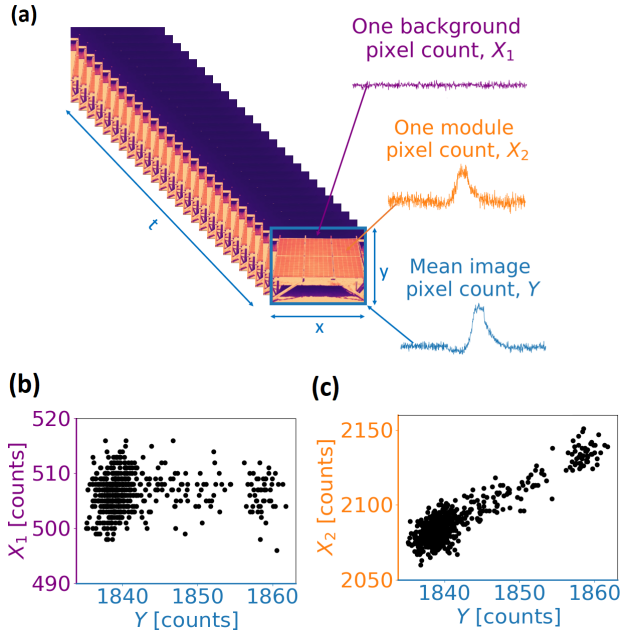


**Figure 3.4:** An image set obtained during an IV curve scan contains information along two spatial dimensions,  $x$  and  $y$ , and one temporal dimension,  $t$ . Values of one background pixel over time,  $X_1$ , are shown in purple, the signal from one module pixel over time,  $X_2$ , is shown in orange and the average image pixel count,  $Y$ , is displayed in blue (a). Variables  $X_1$  and  $X_2$  plotted as a function of  $Y$  (b) and (c) will have no correlation and strong correlation, respectively.

As the reference signal is defined as the average image pixel count, it is affected by the measurement data, such as the number of pixels in the entire image containing the PL signal. The reference signal is also affected by the strength of the emitted PL signal. It has been shown that in the case of a weak and noisy PL signal emitted from Al-BSF modules, smoothing of the reference signal with the Savitzky-Golay filter [43] improves the identification of the PL signal in the module pixels.

Linear similarity can be impaired if the reference signal contains several PL peaks

originating from imaged strings that do not undergo the IV curve sweep simultaneously. As this imaging method allows imaging of several strings at the same time, this is a situation that may arise in image processing in real time, during which a set of several hundred images is processed. If those images show different strings undergoing IV curves asynchronously, the average image pixel count will show several PL peaks, as shown in Fig. 3.5(a), and the  $PCC_{PL}$  image will show lower correlation values, as shown in Fig. 3.5(b). The most pronounced peak originates from the string of three modules, shown in the middle of Fig. 3.5(b), which also has the highest correlation values. The two weaker peaks originate from the damaged module. This data series results from three series being stitched together so that it appears as if the strings were imaged simultaneously. Despite the low correlation values, it is still possible to identify the severely damaged module and three healthy modules.

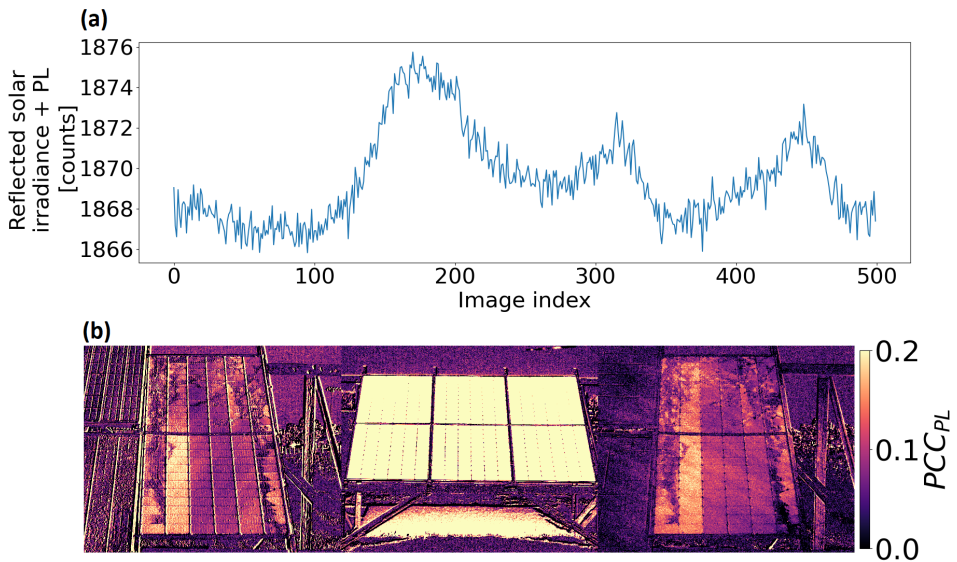


**Figure 3.5:** The reference signal consists of three peaks if three imaged strings undergo the IV curve sweep at different times during imaging (a) and the  $PCC_{PL}$  image obtained if all 500 images are processed simultaneously (b).

### 3.2.3 Imaging in low irradiance conditions: Paper E

In Paper E, we tested the extension of applicability of PL imaging with IV curve sweeps to low irradiance conditions, below  $100 \text{ Wm}^{-2}$ . Imaging in such low irradiance conditions has been conducted only once successfully with instantaneous switching of the OP (lock-in approach) [33], otherwise only under direct sunlight [23, 25, 27, 29–31]. Extension of the applicability of the PL imaging method during IV curve sweeps to lower irradiance levels is advantageous with respect to defect analysis and a wider range of suitable weather conditions.

Validation and comparison with EL images and PL images obtained under direct irradiance were conducted in Paper E, as shown in Fig. 3.6. Figure 3.6(a) and (b) show EL images obtained with SC current and 10% of SC current, while Fig. 3.6(c) and (d) show  $PCC_{PL}$  images obtained under direct and diffuse irradiance. Information that can be obtained from the  $PCC_{PL}$  image obtained under direct irradiance corresponds to the EL image acquired with SC current, while the information obtained from the  $PCC_{PL}$  image collected under diffuse irradiance corresponds to the EL image acquired with 10% of SC current, as expected [44]. It was also investigated whether imaging from the rear was possible, as the investigated modules are bifacial. The  $PCC_{PL}$  image shown in Fig. 3.6(e) was obtained from the rear at  $40 \text{ Wm}^{-2}$  incoming in-plane irradiance and shows good correspondence with Fig. 3.6(d). The image from the rear in Fig. 3.6(e) was mirrored for easier comparison with the images from the front.

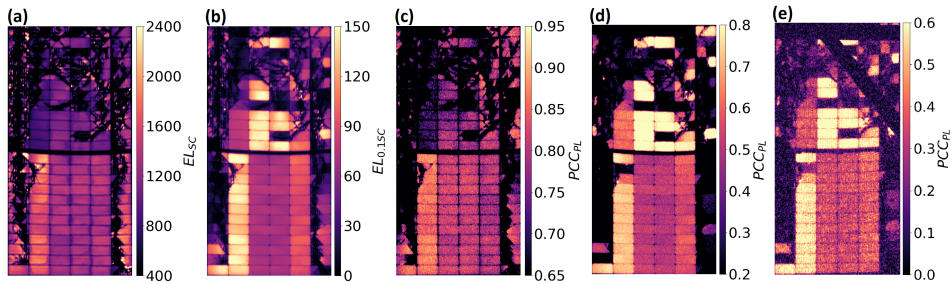


**Figure 3.6:** EL image obtained with SC current (a) and 10% of SC current (b).  $PCC_{PL}$  image obtained in direct (c) and diffuse irradiance conditions from the front (d) and the rear (e).



### 3.3 Presented contributions compared to related studies

A summary of the main concepts addressed in each paper is presented in Fig. 3.7. The papers are listed on a timeline in chronological order with each paper's main topic addressed in the second row. Papers A and C presented a development in the PL imaging method, Paper B presented defect analysis, Paper D demonstrated a new algorithm for image processing, and Paper E demonstrated extension of PL imaging with IV curve sweeps to low irradiance levels. Concrete aspects of the investigation in each paper and how they changed over time are listed. They are the imaging apparatus, module type, method for eliminating reflected solar irradiance, algorithm used for image processing, illumination level and camera orientation. The black line indicates the change in at least one of these aspects in every paper compared to the preceding one.

In Paper A, a Xenics camera was used for imaging Al-BSF modules from the front and under direct irradiance. Remote control of the OP was applied for elimination of reflected solar irradiance, and image processing was conducted with the subtraction algorithm. The change in Paper B compared to Paper A was that the Xenics camera was replaced with a newly purchased Raptor camera. The other aspects of the investigation were the same as in Paper A. Paper C was based on investigation of PERC modules during IV curve sweeps, which is a novel approach compared to the preceding two papers. In Paper D, the PCC algorithm was introduced, and in Paper E, imaging in diffuse irradiance and from the rear side of bifacial modules was conducted.

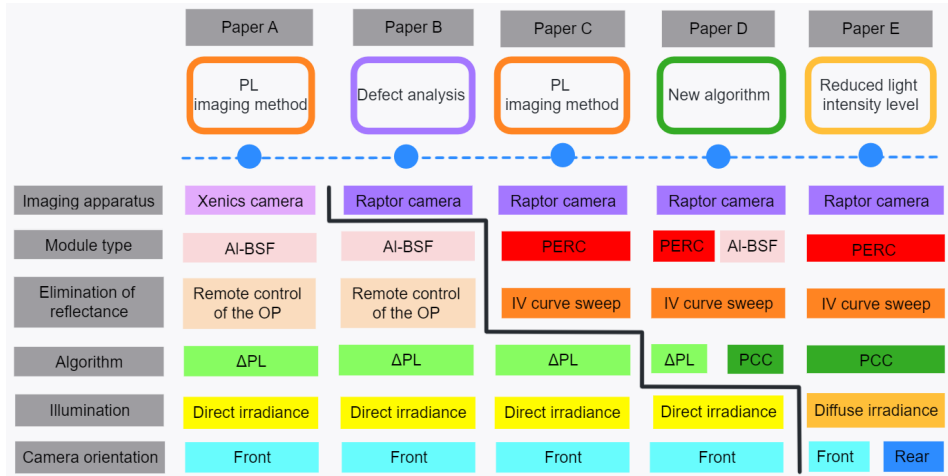


**Figure 3.7:** Chronological order of the five papers produced, their main topics and the main aspects of their content.

To illustrate the connection between the contributions presented in this thesis compared to the studies described in Chapter 2.2, a modification of Fig. 2.10 is shown in Fig. 3.8. Papers A and B fall into the group of studies that use control of the OP for eliminating reflected solar irradiance. The images that result from this procedure are  $\Delta PLOP$  images, as is the case with similar studies that use the lock-in technique. Papers C–E also use the PV system for elimination of reflected solar irradiance, but they employed the built-in functionality of string inverters to conduct IV curve sweeps without having to interfere in its operation by controlling its OP. The images obtained in Paper C are  $\Delta PLOP$  images. Paper D presented a new algorithm for image analysis, which is based on the Pearson correlation coefficient. Because of this, the images are called  $PCC_{PL}$ . These two types of images were used in papers D and E.

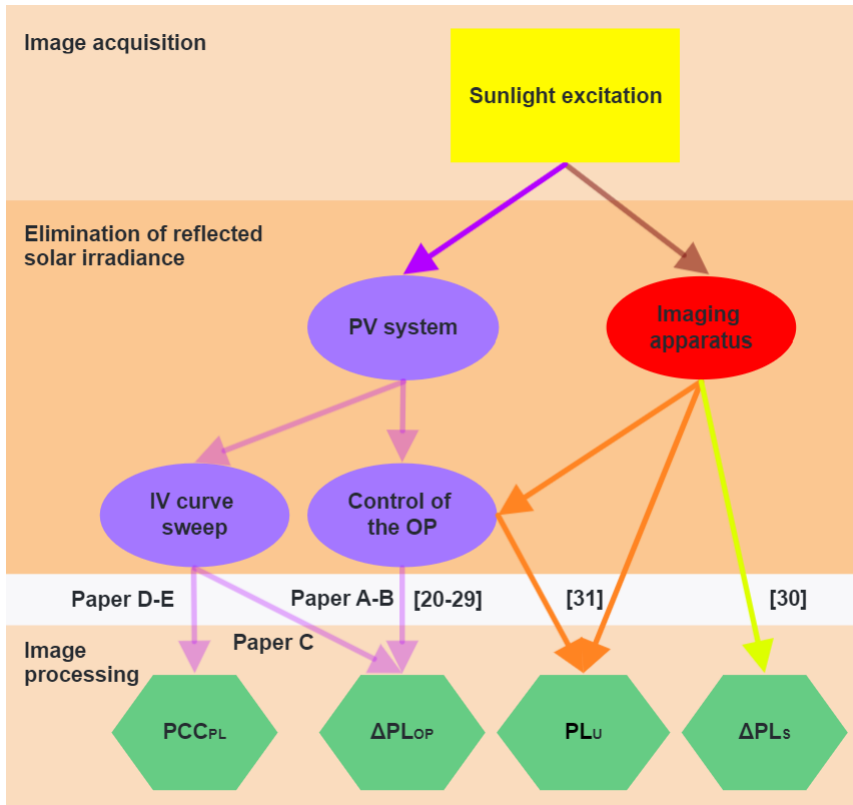


**Figure 3.8:** Modification of Fig. 2.10 incorporates the contributions presented in this thesis.

The overview in Table 2.1 is shown again in Table 3.1 with respect to the five papers presented here. The excitation level was high during image acquisition in papers A–D and below  $100 \text{ Wm}^{-2}$  in Paper E. The last paper extends the possibility of implementing PL imaging during IV curve sweeps to cloudy days with low irradiance. With respect to the necessary additional equipment, the string inverter is used in both PL imaging methods. The advantage is that this is a piece of equipment already installed in the field, and it allows imaging of several strings. When using additional equipment connected to the PV system for control of the OP, it is dimensioned and limited to a certain number of modules.

Explicit control of the OP is not necessary with the IV curve sweep approach, which is the most important contribution of this thesis. This is otherwise possible only

with methods using optical filtering and when no current extraction is necessary. The type of images obtained is either  $\Delta P_{LOP}$ , as in most of the other studies, or  $PCC_{PL}$ , presented in Paper D. PL imaging during IV curve sweeps is the only approach that, based on one image series, results in several  $\Delta P_{LOP}$  or  $PCC_{PL}$  images. As explained above, they provide insight into series resistance-related defects and can be obtained from the IV curve sweep approach without having to adjust the level of current extraction and without acquiring a new series of images.

**Table 3.1:** Overview of the present thesis's contributions to photoluminescence imaging of field-deployed modules with respect to the aspects presented in Table 2.1.

Study	Excitation intensity [ $Wm^{-2}$ ]	Additional equipment	PV area size	Control of the OP (IV curve: >3 delayed: d)	Image type (No. of images/ one image series)
Paper A-B	direct sunlight	string inverter	several strings	yes (>3,d)	$\Delta P_{LOP}$ (1)
Paper C	direct sunlight	string inverter	several strings	no	$\Delta P_{LOP}$ (>1)
Paper D	direct sunlight	string inverter	several strings	no	$PCC_{PL}$ (>1)
Paper E	<100	string inverter	several strings	no	$PCC_{PL}$ (>1)

### 3.4 Outlook

For an efficient investigation of utility-scale power plants with an imaging method, high throughput in combination with an unsupervised, real-time image analysis is desirable. A step in this direction has been made with PL imaging during IV curve sweeps and the application of the PCC algorithm for image processing. The

imaging can be conducted in cloudy conditions, which is advantageous with respect to defect analysis, and more importantly, regarding a wider range of available weather conditions.

There are several advantages of PL imaging in combination with IV curve sweeps in a PV power plant. The string inverter's functionality to conduct IV curve sweeps has been developed for monitoring purposes, among others. In this way, PL imaging can be connected to another type of monitoring technique. Initiating IV curves through a smartphone could be compatible with imaging from a UAV. Alternatively, if the string inverter does not offer the functionality of controlling the IV curve sweeps, one could wait until it takes place. The latter opens up the possibility of using a ground-mounted vehicle that would conduct imaging autonomously and with real-time image processing. The imaging system would collect images and process them in real time, which would enable detecting the occurrence of the IV curve sweep. The imaging would then proceed to a new group of modules.

A future step in developing PL imaging might be an autonomous imaging procedure from either the air or ground. Solving the challenges of image acquisition and processing from a vehicle in motion might enable the collection of a wider number of images and a greater insight into defects that are detectable. This has been limited until now. An interesting question is how the obtained images can be used for the prediction of power loss. It has been suggested that machine learning and deep learning methods are the future of image processing and fault detection [7].



# Chapter 4

## Conclusion

The need for surveillance and monitoring of thousands of PV modules in utility-scale PV power plants results in the pursuit of efficient and accurate inspection techniques. Imaging techniques have become valuable for the sake of precise localization of the defects as well as high throughput. Photoluminescence imaging is a promising imaging technique because of the level of information it can provide. It was only recently adapted for outdoor application, and is still in an early stage of development with respect to its implementation in the field.

The goal of this thesis was to conduct photoluminescence imaging on as large a PV area as possible with as little interference as possible. The contribution is the development of two photoluminescence imaging procedures that do not require any physical contact with the PV system, enable imaging of several strings simultaneously and rely on the equipment already installed in the field (string inverter). The procedure for imaging during IV curve sweeps is far more suited for application in a PV power plant than controlling the OP of the PV system remotely. A new and robust algorithm has been proposed for processing of images acquired during IV curve sweeps. It results in a computationally cost-efficient data analysis, suitable for real-time applications. The approach is also applicable in low-intensity illumination conditions. While the first attempt to conduct defect analysis failed, it was confirmed with images collected in low irradiance conditions that they correspond to the electroluminescence images obtained with 10% of short-circuit current.





# Bibliography

- [1] Message from the technical chair: 1 TW and counting. <https://www.eupvsec.org/index.php?view=article&id=21&catid=12>. Last accessed 9 February 2023.
- [2] H Bahar. Renewables 2022: Analysis and forecast to 2027. Technical report, International Energy Agency, 2022.
- [3] M Meribout, V K Tiwari, J P P Herrera, and A N M A Baobaid. Solar panel inspection techniques and prospects. *Measurement*, page 112466, 2023.
- [4] M Meribout. Sensor systems for solar plant monitoring. *IEEE Transactions on Instrumentation and Measurement*, 72:1–16, 2023.
- [5] I Høiaas, K Grujic, A G Imenes, I Burud, E Olsen, and N Belbachir. Inspection and condition monitoring of large-scale photovoltaic power plants: A review of imaging technologies. *Renewable and Sustainable Energy Reviews*, 161:112353, 2022.
- [6] M Waqar Akram, G Li, Y Jin, and X Chen. Failures of photovoltaic modules and their detection: A review. *Applied Energy*, page 118822, 2022.
- [7] O Kunz, J Schlipf, A Fladung, Y S Khoo, K Bedrich, T Trupke, and Z Hameiri. Outdoor luminescence imaging of field-deployed PV modules. *Progress in Energy*, 4(4):042014, 2022.
- [8] W Herrmann, G Eder, B Farnung, G Friesen, M Köntges, B Kubicek, O Kunz, H Liu, D Parlevliet, I Tsanakas, et al. Qualification of photovoltaic PV power plants using mobile test equipment. *IEA-PVPS T13-24: 2021*, 2021.

- 
- [9] F Grimaccia, S Leva, A Dolara, and M Aghaei. Survey on PV modules' common faults after an O&M flight extensive campaign over different plants in Italy. *IEEE Journal of Photovoltaics*, 7(3):810–816, 2017.
- [10] M Köntges, A Morlier, G Eder, E Fleiß, B Kubicek, and J Lin. Ultraviolet fluorescence as assessment tool for photovoltaic modules. *IEEE Journal of Photovoltaics*, 10(2):616–633, 2020.
- [11] S Koch, T Weber, C Sobottka, A Fladung, P Clemens, and J Berghold. Outdoor electroluminescence imaging of crystalline photovoltaic modules: Comparative study between manual ground-level inspections and drone-based aerial surveys. In *32nd European Photovoltaic Solar Energy Conference and Exhibition*, pages 1736–1740, 2016.
- [12] T Kropp, M Berner, L Stoicescu, and J H Werner. Self-sourced daylight electroluminescence from photovoltaic modules. *IEEE Journal of Photovoltaics*, 7(5):1184–1189, 2017.
- [13] G A dos Reis Benatto, C Mantel, S Spataru, A A S Lancia, N Riedel, S Thorsteinsson, P B Poulsen, H Parikh, S Forchhammer, and D Sera. Drone-based daylight electroluminescence imaging of PV modules. *IEEE Journal of Photovoltaics*, 10(3):872–877, 2020.
- [14] B Doll, J Hepp, M Hoffmann, R Schüler, C Buerhop-Lutz, I M Peters, J A Hauch, A Maier, and C J Brabec. Photoluminescence for defect detection on full-sized photovoltaic modules. *IEEE Journal of Photovoltaics*, 11(6):1419–1429, 2021.
- [15] G A dos Reis Benatto, M Chi, O B Jensen, A A S Lancia, N Riedel, B Iandolo, R S Davidsen, O Hansen, S Thorsteinsson, and Peter B Poulsen. Photoluminescence imaging induced by laser line scan: Study for outdoor field inspections. In *2018 IEEE 7th World Conference on Photovoltaic Energy Conversion (WCPEC)(A Joint Conference of 45th IEEE PVSC, 28th PVSEC & 34th EU PVSEC)*, pages 0395–0399. IEEE, 2018.
- [16] C Ballif, F-J Haug, M Boccard, P J Verlinden, and G Hahn. Status and perspectives of crystalline silicon photovoltaics in research and industry. *Nature Reviews Materials*, 7(8):597–616, 2022.
-

- 
- [17] T Trupke, B Mitchell, JW Weber, W McMillan, RA Bardos, and R Kroeze. Photoluminescence imaging for photovoltaic applications. *Energy Procedia*, 15:135–146, 2012.
- [18] I Burud, T Mehl, A Flo, D Lausch, and E Olsen. Hyperspectral photoluminescence imaging of defects in solar cells. *Journal of Spectral Imaging*, 5:1–5, 2016.
- [19] C B Honsberg and S G Bowden. Photovoltaics education website, 2019. Last accessed 12 May 2023.
- [20] L Stoicescu, M Reuter, and J H Werner. Daysy: luminescence imaging of PV modules in daylight. In *29th European Photovoltaic Solar Energy Conference and Exhibition*, pages 2553–2554, 2014.
- [21] L Stoicescu, M Reutner, and J H Werner. Method and apparatus for testing photovoltaic modules, 2015. United States Patent US 9,680,412 B2.
- [22] Solarzentrum Stuttgart GMBH. Daysy - daylight luminescence system - measurement guide. [https://www.solarzentrum-stuttgart.com/uploads/file/DaySy\\_Measurement\\_Guide\\_current.pdf](https://www.solarzentrum-stuttgart.com/uploads/file/DaySy_Measurement_Guide_current.pdf), 2019. Last accessed 01 April 2023.
- [23] T J Silverman, M G Deceglie, K VanSant, S Johnston, and I Repins. Illuminated outdoor luminescence imaging of photovoltaic modules. In *2017 IEEE 44th Photovoltaic Specialist Conference (PVSC)*, pages 3452–3455. IEEE, 2017.
- [24] M Guada, Á Moretón, S Rodríguez-Conde, L A Sánchez, M Martínez, M Á González, J Jiménez, L Pérez, V Parra, and O Martínez. Daylight luminescence system for silicon solar panels based on a bias switching method. *Energy Science & Engineering*, 8(11):3839–3853, 2020.
- [25] R Bhoopathy, O Kunz, M Juhl, T Trupke, and Z Hameiri. Outdoor photoluminescence imaging of photovoltaic modules with sunlight excitation. *Progress in Photovoltaics: Research and Applications*, 26(1):69–73, 2018.
- [26] R Bhoopathy, O Kunz, M Juhl, T Trupke, and Z Hameiri. Outdoor photoluminescence imaging of solar panels by contactless switching: Technical
-

- 
- considerations and applications. *Progress in Photovoltaics: Research and Applications*, 28(3):217–228, 2020.
- [27] O Kunz, G Rey, M K Juhl, and T Trupke. High throughput outdoor photoluminescence imaging via PV string modulation. In *2021 IEEE 48th Photovoltaic Specialists Conference (PVSC)*, pages 0346–0350. IEEE, 2021.
- [28] L Köster, A Astigarraga, S Lindig, and D Moser. Development of daylight photoluminescence technique for photovoltaic modules and investigation of temperature dependency. In *Proceedings of the 37th European Photovoltaic Solar Energy Conference and Exhibition, Online*, pages 7–11, 2020.
- [29] L Köster, A Astigarraga, S Lindig, A Louwen, M Antinori, D Moser, and G Manzolini. Quality assurance of the photovoltaic power plants installation stage—a complementary strategy based of photoluminescence and steady-state thermography. In *Proceedings of the 38th European Photovoltaic Solar Energy Conference and Exhibition*, pages 1042–1050, 2021.
- [30] O Kunz, G Rey, R Bhoopathy, Z Hameiri, and T Trupke. Outdoor PL imaging of crystalline silicon modules at constant operating point. In *2020 47th IEEE Photovoltaic Specialists Conference (PVSC)*, pages 2140–2143. IEEE, 2020.
- [31] G Rey, O Kunz, M Green, and T Trupke. Luminescence imaging of solar modules in full sunlight using ultranarrow bandpass filters. *Progress in Photovoltaics: Research and Applications*, 30(9):1115–1121, 2022.
- [32] O Breitenstein, W Warta, and M Langenkamp. *Lock-in Thermography: Basics and Use for Evaluating Electronic Devices and Materials*, volume 10. Springer, 2010.
- [33] L Stoicescu and M Reuter. Daysy contactless measurements of PID shunt resistance in installed PV modules. In *25th European Photovoltaic Solar Energy Conference and Exhibition*, pages 1337–1339, 2018.
- [34] L Koester, S Lindig, A Louwen, A Astigarraga, G Manzolini, and D Moser. Review of photovoltaic module degradation, field inspection techniques and techno-economic assessment. *Renewable and Sustainable Energy Reviews*, 165:112616, 2022.
-

- 
- [35] International Electrotechnical Commission. Photovoltaic devices-part 13: Electroluminescence of photovoltaic modules IEC TS 60904-13, 2018.
- [36] S Spataru, D Sera, T Kerekes, and R Teodorescu. Monitoring and fault detection in photovoltaic systems based on inverter measured string IV curves. In *31st European Photovoltaic Solar Energy Conference and Exhibition*, pages 1667–1674. WIP Wirtschaft und Infrastruktur GmbH & Co Planungs KG, 2015.
- [37] International Fronius, GmbH. Lower losses in the case of partial shading of pv systems, 2022. Last accessed 8 May 2023.
- [38] Sungrow. Data-driven monitoring starts at the inverter, 2020. Last accessed 8 May 2023.
- [39] China General Certification Center and Ltd. Huawei Technologies Co. Smart I-V curve diagnosis: technical white paper, 2020. Last accessed 8 May 2023.
- [40] Danfoss. Tlx reference manual, 2010. Last accessed 8 May 2023.
- [41] P G Ellingsen et al. Hyperspectral analysis using the correlation between image and reference. *Journal of Biomedical Optics Letters* 18(2), pages 020501–1–020501–3, 2013.
- [42] D Inamdar et al. The correlation coefficient as a simple tool for the localization of errors in spectroscopic imaging data. *Remote Sensing* 10(2), 231.
- [43] R W Schafer. What is a Savitzky-Golay filter? *IEEE Signal Processing Magazine*, pages 111–117, 2011.
- [44] W Mühleisen, C Hirschl, G Brantegger, L Neumaier, M Spielberger, H Sonnleitner, B Kubicek, G Ujvari, R Ebner, M Schwark, et al. Scientific and economic comparison of outdoor characterisation methods for photovoltaic power plants. *Renewable Energy*, 134:321–329, 2019.
-




# Appendix A

## Paper A





# Photoluminescence imaging of silicon modules in a string

Marija Vuković  | Ingeborg Eriksdatter Høiaas | Marko Jakovljević |  
 Andreas Svarstad Flø | Espen Olsen | Ingunn Burud

Faculty of Science and Technology, Norwegian  
 University of Life Sciences, Ås, Norway

## Correspondence

Marija Vuković, Faculty of Science and  
 Technology, P.O.Box 5003 NMBU, Ås 1432,  
 Norway.  
 Email: marija.vukovic@nmbu.no

## Present address

Marija Vuković, Faculty of Science and  
 Technology, P.O.Box 5003 NMBU, Ås, 1432,  
 Norway

## Funding information

Norges Forskningsråd; The Norwegian  
 Research Center for Sustainable Solar Cell  
 Technology  
 (FMESUSOLTECH,projectnumber257639/  
 E20)

## Abstract

Spectral imaging techniques are a powerful tool for surveillance and monitoring of degradation mechanisms in PV modules. Luminescence images of solar modules have until recently been predominantly acquired in controlled laboratory settings. Recent attempts have been made in detecting luminescence in daylight. This study aims to present a proof of concept for detection of photoluminescence with sunlight excitation. It enables imaging of several modules in a string as well as several strings simultaneously by changing the operating point through wireless and contactless communication with one or more string inverters. This new approach is validated with the electroluminescence technique as well as with an already established photoluminescence technique under sunlight excitation. Due to the string inverter's reaction time, the change in illumination results in lower image quality. However, with a more up-to-date imaging equipment, this approach is promising for identification of certain degradation mechanisms which can be detected with lower resolution such as large area damage and inactive areas. Further studies are needed to optimize the method and potentially use it in connection with an unmanned aerial vehicle inspection.

## KEYWORDS

inverter, photoluminescence, PV modules, string

## 1 | INTRODUCTION

Luminescence imaging is an established method for inspection and characterization of silicon solar cells and modules in a laboratory setting.<sup>1–14</sup> Carrying through the same type of analysis outdoor in the PV plants for the purpose of quality control is challenging due to uncontrollable light conditions. Quality control of PV modules in the field can be carried out by demounting and inspecting them with electroluminescence (EL) imaging in a closed laboratory setting<sup>15</sup> or by using a mobile laboratory for on-site inspections.<sup>16</sup> Even though such an approach has the advantage of controllable light conditions, it is desirable to develop methods for inspection of modules in the

field. Outdoor luminescence imaging has therefore been carried out in the dark,<sup>17–19</sup> very low light conditions<sup>20–22</sup> as well as in daylight.<sup>23–35</sup>

The basis of photoluminescence (PL) imaging is charge carrier excitation with an illumination source which can be a laser,<sup>6,21</sup> LEDs,<sup>2,36</sup> or sunlight.<sup>27–31,34,35</sup> However, the reflected light from the illumination source needs to be accounted for. If the wavelength of the reflected signal does not coincide with the emitted PL signal, reflection can be eliminated by use of optical filters. In the case of daylight imaging, the wavelengths of the reflected signal and the emitted PL signal overlap as shown in Figure 1. The reflected sun spectrum of a solar module of the type used in this study illuminated

This is an open access article under the terms of the Creative Commons Attribution-NonCommercial-NoDerivs License, which permits use and distribution in any medium, provided the original work is properly cited, the use is non-commercial and no modifications or adaptations are made.

© 2021 The Authors. Progress in Photovoltaics: Research and Applications published by John Wiley & Sons Ltd.

with sunlight is acquired with a hyperspectral camera (red curve), while the PL spectrum emitted from a silicon multi-crystalline solar cell is acquired with the same hyperspectral camera in a laboratory setting (blue curve). A hyperspectral camera is a type of camera with which a three-dimensional image can be acquired, the third dimension being the spectral dimension which can consist of several hundreds of wavelengths. The spectra displayed here are the average pixel count at a single wavelength. The wavelength interval of 1000–1300 nm illustrates the wavelengths of interest and is based on the selection of the relevant bands in the hyperspectral cube after image acquisition. Since the signals were recorded in different conditions, their respective intensities, represented with the two y-axis, are not comparable. Even though the PL signal overlaps with a part of the solar spectrum which is weaker due to atmospheric absorption of water, the sun spectrum is still several orders of magnitude stronger than the PL signal.<sup>26,28</sup> The two signals superimpose and therefore cannot be filtered out. The reflected signal needs to be subtracted.<sup>27–31,34,35</sup>

The need to subtract the unwanted reflection from the module has resulted in an approach in which a pair of images in two different operating points is alternately recorded. The image recorded in the operating point in which the module emits less signal is subtracted from the image recorded in the operating point in which the module emits more signal. Subtraction of one image from the other reveals the difference  $\Delta PL$  signal between the two operating points and removes the reflected signal.

A few different methods have so far been developed in order to switch a module's operating point for the purpose of PL imaging in sunlight. Using a solid state-relay<sup>30</sup> or a MOSFET as an on/off switch connected to the module's terminals<sup>34</sup> enables extremely rapid, almost instantaneous, switching and acquisition of a pair of images to be taken under nearly the same illumination conditions. Another approach is based on connecting a module or a module string to a specially developed piece of equipment.<sup>35,37,38</sup>

Apart from the modules' terminals, it is possible to accomplish instantaneous control of the operating point of a sub-string by varying the illumination on one control cell by a LED lamp. In that way, the operating point is determined for all remaining cells in the sub-string.<sup>28,37</sup> This approach has further been applied to switching the operating point of a module connected to a micro-

inverter.<sup>29</sup> Even though it is expected that the method can be used on a sub-string or a whole module without disturbing the production of a large-scale PV plant at the same time as different levels of current extraction from the sub-string are possible,<sup>29</sup> it requires physically covering a cell in a sub-string. This approach has been taken a step further to PV string level. It enables imaging of several modules simultaneously by covering solar cells in different modules in a string with multiple LEDs.<sup>39</sup>

Due to these technical aspects, PL imaging, which in a laboratory setting is a wireless imaging method, requires physically connecting a piece of equipment to one or several modules in case of outdoor imaging with sunlight excitation. Similarly to EL imaging, a method which requires contact with a module or a string due to excitation through current, PL imaging under sunlight excitation is in practice not much easier to carry through. Apart from two references on how it could be conducted on string level,<sup>38–39</sup> PL imaging has so far only been performed on module level,<sup>27–29,31,34</sup> while EL imaging, despite the need for wiring, has been conducted on string level in combination with aerial image acquisition. This has been possible by energizing strings one at a time using switch boxes.<sup>18</sup> Switching can be remotely controlled<sup>40</sup> and automated.<sup>19</sup> If an external power supply is used, the number of modules which can be imaged at once, and which thus need to be connected, is dependent on the possibility to power such a supply on site. This can pose a problem in isolated areas since the size of the equipment increases with the increasing number of modules connected simultaneously.<sup>18</sup> Systems have also been developed for EL imaging in sunlight in which the necessary electrical power comes from other PV strings<sup>32,35</sup> or, on module level, from the module under investigation itself.<sup>32</sup> These systems enable EL in addition to EL + PL imaging. EL + PL imaging for up to 20 modules per string at a time can be conducted, but connection to specially developed equipment is needed.<sup>35,37</sup>

In the current study, we demonstrate how PL imaging can be performed on one or simultaneously on more strings without any physical contact with the PV system such as the case is with EL imaging and other reported cases of PL imaging. This can be achieved through controlling the operating point of one or several string inverters with wireless communication, which makes the PL imaging possible for all affected modules. This opens up for the

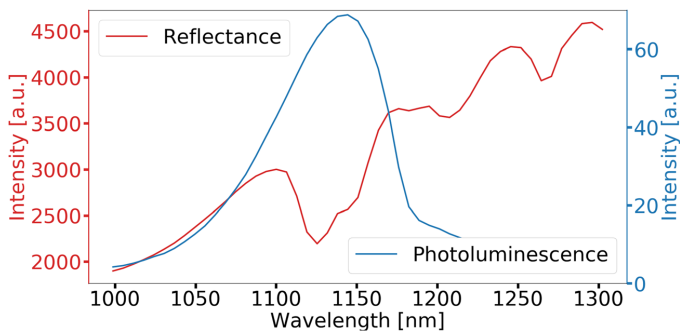


**FIGURE 1** Spectral distribution of the PL signal emitted from a silicon solar cell and the sun spectrum reflected from a silicon module's surface. The signals were recorded with a hyperspectral camera in the laboratory setting and in sunlight, respectively

possibility of performing PL imaging from an unmanned aerial vehicle (UAV).

The obtained results are validated with an  $EL_{SC}$  image obtained in the dark with SC current,  $I_{SC}$ , as well as with  $\Delta PL$  images acquired through the earlier mentioned method based on switching a module's operating point through its terminals with a MOSFET.<sup>34</sup> We have reproduced results with this method and can verify that it is valid. This approach has thus been carried through by two independent research groups. We are confident in this method and have chosen to use the images collected in this way as ground truth. This study describes a proof of concept through result validation with already tested imaging methods, by addressing the preprocessing challenges posed by the strong background (BG) signal as well as by reflecting upon the possible applications.

## 2 | THEORY

The relationship between the intensity of the luminescence signal  $\phi$  over an area of a silicon solar cell and diode junction voltage  $V$  of that region can be approximated with

$$\phi \propto e^{\frac{V}{V_T}} \quad (1)$$

where  $V_T$  is the thermal voltage.<sup>1,7,11</sup> The strongest luminescence signal is acquired when diode voltage is highest and that is the case under the open circuit (OC) condition when  $V=V_{OC}$ . With increasing current extraction, the diode voltage decreases resulting in a decreasing luminescence intensity. The luminescence intensity is weakest when the  $I_{SC}$  is extracted.

If the reflection from the illumination source does not interfere with the measured PL signal during image acquisition,<sup>2,6</sup> it suffices that the cell or a module is imaged in one condition only, for example, in the OC condition in which the PL signal intensity is the highest. In cases when the reflected and emitted signals overlap and the reflected signal needs to be subtracted, two images are recorded with different diode voltages, i.e., different luminescence signal intensities.<sup>27-29,31,34</sup> Image acquisition can be carried through by switching

between two operating points such as OC and short circuit (SC), 0.75C and SC,<sup>34</sup> OC and Maximum Power Point (MPP), or any two points between the OC and MPP conditions.<sup>29</sup> The higher the voltage difference  $\Delta V$  between the two points, the higher is the  $\Delta PL$  signal intensity.

As illustrated in Figure 2A, the voltage difference between  $V_{OC}$  and  $V_{SC}$  is greater than  $\Delta V$  between  $V_{OC}$  and  $V_{MPP}$  or any two other operating points. The intensity of the PL signal in OC, MPP, and SC conditions,  $PL_{OC}$ ,  $PL_{MPP}$ , and  $PL_{SC}$ , is illustrated in (B). The signals  $PL_{OC}$  and  $PL_{SC}$  originate from a multi-crystalline silicon solar cell illuminated with laser light and imaged with a hyperspectral camera in a laboratory setting. The imaging conditions and the illumination intensity were the same for both images. The weak PL signal in the SC condition despite the maximum current extraction could originate from variability in minority carrier lifetime.<sup>11</sup> Due to the lack of a measured  $PL_{MPP}$  signal, it has been estimated based on the measured  $PL_{OC}$  and  $PL_{SC}$  signals,  $I_{MPP}$  given in the specifications of the cell imaged and the linear relationship between current and the intensity of the PL signal as demonstrated in Trupke.<sup>11</sup> The PL signal intensity increases along the IV curve from the SC to OC condition where it is at its maximum. The  $\Delta PL_{OC-SC}$  image acquired by switching between OC and SC has thus a higher intensity than for example a  $\Delta PL_{OC-MPP}$  image.

The choice of the operating points might be conditioned by the wish to obtain the best possible image quality with the highest possible signal to noise ratio (SNR) or by the equipment used. In this study, the choice of operating points is conditioned through the inverter. The image with the stronger PL intensity, in this study always the image in OC condition, will be referred to as the PL image, while the image with weaker PL intensity will be referred to as the BG image. This will be addressed in the following section.

## 3 | METHOD

The investigated modules were mounted on the Campus of the Norwegian University of Life Sciences in Ås, Norway, approximately 5–7 years ago. A string inverter of type Fronius Primo 3.0 is connected to a string of 12 multi-crystalline modules of type SweModule

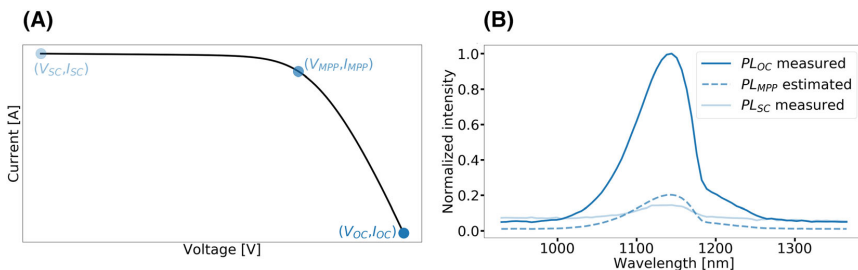


**FIGURE 2** The dots on the IV curve illustrate the operating points used in this study (A). The accompanying graph (B) illustrates the intensity of the PL signal in those points

*Inceptio* 250F with nominal power output of 250 W,  $I_{SC}$  of 8.80 A, and  $V_{OC}$  of 37.7 V ( $V_{OC}=628$  mV/cell) measured at STC. A short-wave infrared (SWIR) camera Xeva 320 with an InGaAs detector (1000–1700 nm) and  $320 \times 256$  resolution was used for image acquisition together with an optical band-pass filter by Edmund Optics with the wavelength interval 1100–1150 nm and optical density  $\geq 4.0$ . A white spectralon reference plate with 25% reflection was imaged together with the modules for the purpose of image correction.

Controlling the string's operating point through the string inverter is conditioned through its electronics, which holds the system around the MPP, with no significant DC current oscillations when the MPP is found. The user cannot influence this algorithm and request significantly higher DC string current. However, the current can be reduced through the output power limitation. Because of that, the two operating points can be chosen between MPP, always sought by the Maximum Power Point Tracker (MPPT), and OC. In this study, OC and MPP are thus the two points which would give the highest  $\Delta PL$  signal. For this reason, they are chosen as the two operating points during inverter modulation.

The switching between two operating points through an inverter is not instantaneous and can take up to several seconds,<sup>29</sup> which may lead to considerable changes in illumination conditions. In order to assess how long time it takes on average between the last image in one operating point and the first image in the next operating point is recorded, an imaging test series was conducted by switching the operating point OC-MPP back and forth several times. It was found that it takes on average 5.5-s between two image acquisitions in two different operating points.

This long delay poses the need to validate and assess reliability of the data collected through switching of a string inverter. A validation step has therefore been performed in which instantaneous switching of a module's operating point through the MOSFET<sup>34</sup> was conducted. In that way, a ground truth image of a module,  $\Delta PL_{OC-SCgt}$ , was obtained. However, the switching through a MOSFET implies working in the OC and SC conditions as opposed to OC and MPP conditions as is the case with inverter modulation. It is not possible to directly

validate the  $\Delta PL_{OC-MPP}$  images acquired through inverter OC-MPP switching with the  $\Delta PL_{OC-SCgt}$  image acquired through MOSFET modulation as the operating points for the BG images differ. The  $\Delta PL$  signal intensity will therefore be different. Because of that, a simulation step has been performed by building in a 5.5-s delay into the software control of the MOSFET. This makes it possible to simulate the effects of such a delay in a  $\Delta PL_{OC-SC}$  image and compare it with the ground truth image,  $\Delta PL_{OC-SCgt}$ , acquired with the instantaneous switching described above. Finally, an EL image with  $I_{SC}$  was acquired in the dark for the sake of a more sound comparison.

The experimental setup for the acquisition of the ground truth image with instantaneous MOSFET modulation differs from the setup for modulation through the string inverter. The data collection and processing before obtaining the ground truth image is also considerably different from the simulation step and image acquisition employing an inverter where a 5.5-s delay occurs. This is illustrated in Figures 3–5.

### 3.1 | Experimental setup

Due to the nominal characteristics of the modules and the MOSFET, the transistor could be used as an on/off switch on one module at a time. Thus one module was disconnected from the string of 12 modules, and the switch was connected to its terminals<sup>34</sup> as shown in Figure 3A. The type of switching device used was a solid state relay with MOSFET output and maximum ON-state resistance 0.02  $\Omega$ . The MOSFET (green square) is connected to the positive (red wire) and the negative (black wire) terminal of the module as well as to the triggering box (black square). Triggering box is a USB based data acquisition and control device by National Instruments. One of the digital outputs on the device is controlled by LabView program and is connected to the triggering input of the camera. The box thus controls the operating point of the module, camera triggering and image acquisition. The procedure is programmed using LabView.

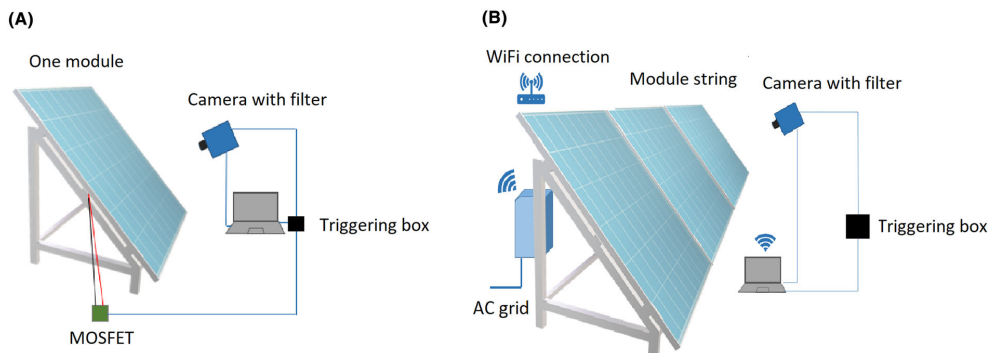


**FIGURE 3** Photoluminescence image acquisition of a module through MOSFET modulation (A) and through wireless string inverter modulation (B)

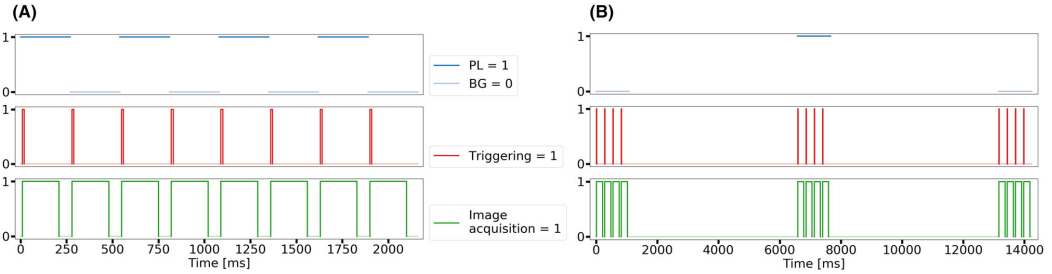


**FIGURE 4** Instantaneous (A) and delayed switching (B) of module's operating point, camera triggering, and image acquisition

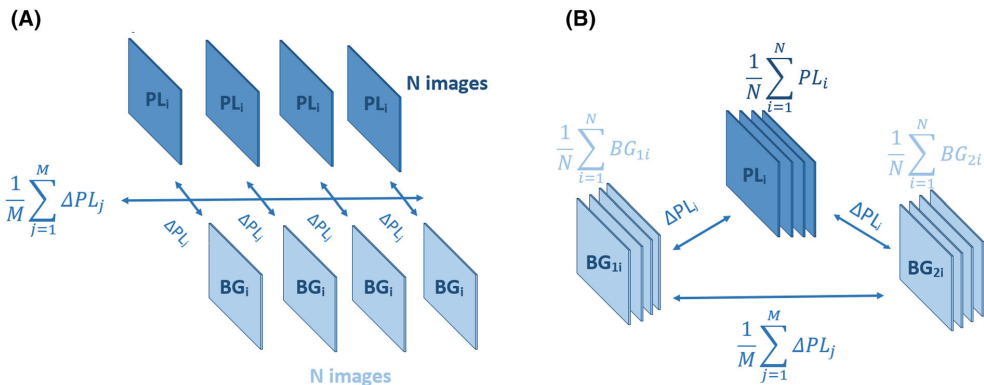


**FIGURE 5** Calculation of the  $\Delta PL$  image obtained when images are collected through instantaneous switching of the module's operating point (A). Obtaining a  $\Delta PL$  image when the modulation is conducted through the string inverter and delayed MOSFET modulation (B)

The setup for PL imaging of a module string with modulation through the string inverter is shown in Figure 3B. Image acquisition and switching of the operating point of the module string through the inverter were synchronized through LabView. Communication with the inverter was established through communication protocol Modbus TCP over WiFi. The software triggered the camera through a triggering box (black square) and synchronized image acquisition with the modules' operating point.

The software logic controlling the inverter needs to trigger the camera depending on when the two desired operating points are reached. The operating points are alternated by changing the output DC power between the maximum power in the MPP and minimum power in the OC condition. The indication of the operating point is obtained through current readings from the inverter through Modbus TCP. For the purposes of this study, the OC position is considered to be reached when  $I_{OC} = 0.5\%I_{MPP}$ , at which point the camera is triggered. Setting the upper current limit for camera triggering in the MPP position requires taking into account the irradiation conditions. Data collection was carried out during a clear summer day in June

2020 with in-plane global irradiation of approximately 800–1000 W/m<sup>2</sup>, which meant that the MPP current could be set to  $I_{MPP} \geq 7$  A.

The image acquisition starts in the MPP condition which corresponds to acquisition of BG images. After a pre-set number of images has been recorded, a signal is sent to the inverter which reduces the output power and thus enables the change of operating point. The inverter then needs to reach the given operating point which takes several seconds. The camera is triggered when the current limits are surpassed as mentioned above. The type of inverter for such image acquisition procedure would need to have the possibility for WiFi connection as well as the possibility for its power to be limited from full to zero output power. Communication over WiFi can make it possible to connect to several inverters simultaneously.

### 3.2 | Image acquisition

The rapid reaction time of the MOSFET and the interchangeable acquisition of the PL and BG images are illustrated in Figure 4A. The

instantaneous change of the module's operating point in which the PL and BG images are obtained in OC and SC conditions is shown at the top. Camera triggering (middle) and image acquisition with 200-ms integration time (bottom) are synchronized with the switching of the operating point. For the illustration purposes, it is shown how 8 images, 4 OC and 4 SC images, can be acquired interchangeably. In this manner, 500 OC and 500 SC images were collected with 200-ms integration time for the ground truth image,  $\Delta PL_{OC-SCgt}$ .

The effects of the inverter's response time and also of the built-in delay in the MOSFET switching procedure are illustrated in Figure 4B. The time it takes to change the operating point for PL and BG image acquisition is considerably longer than the time for the image acquisition itself (top). Camera triggering (middle) and image acquisition (bottom) are postponed accordingly between images taken in different operating points. The illustration shows how such a delay affects image acquisition when 4 images are acquired in one operating mode. Due to long response time compared with the image acquisition time of 200 ms, it makes sense to take several images while the module is in one operating mode before switching.<sup>29</sup>

During simulation of delayed reaction time with the MOSFET, series of images were taken with 6, 10, 20, 40, and 80 images per interval in order to assess image quality for one  $\Delta PL_{OC-SC}$  image with varying number of images per interval. These tests would give an indication on how low the image number per interval could be in order to get satisfactory images. The analysis has shown that a  $\Delta PL_{OC-SC}$  image obtained with intervals of 20 images gives satisfactory results without having to increase the number of images more and thus the image acquisition time. Using intervals of less than 20 images results in poorer image quality due to BG signal, while increasing the number of images above 20 leads to illumination changes during the acquisition of one interval, which also leads to lower image quality.

Based on these considerations, data collection was conducted with 20 images per interval as indicated in Table 1. Firstly, 1000 images were recorded of a module with instantaneous MOSFET switching between OC and SC conditions in order to obtain a ground truth image of one module,  $\Delta PL_{OC-SCgt}$ . Modulation with the MOSFET with built-in delay between OC and SC conditions was then conducted with 20 images per interval and resulted in a  $\Delta PL_{OC-SC}$  image. The same number of images per interval was used during image acquisition of one module through inverter modulation

resulting in a  $\Delta PL_{OC-MPP}$  image. These images were recorded from a distance of approximately 5 m. At the end, a  $\Delta PL_{OC-MPP}$  image was obtained of six modules in the string in order to test the possibilities of imaging several modules at a time from a distance of 12 meters. Every image acquisition was carried out with integration time of 200 ms.

### 3.3 | Data processing

The calculation of the ground truth image based on data collection through instantaneous mode switching<sup>28,34</sup> is illustrated in Figure 5A. For illustrational purposes, 4 images are shown for every mode as illustrated in Figure 4A. The interchangeable acquisition of  $i = 1, \dots, N$  images in OC condition containing the PL signal and the BG signal and  $i = 1, \dots, N$  images in SC condition containing the BG signal results in  $j = 1, \dots, M$  difference images,  $\Delta PL_j$ . In this case, the sets  $N$  and  $M$  are equally big. The  $\Delta PL_j$  images are averaged into one  $\Delta PL$  image.<sup>23-26,28,33-35</sup> The resultant image was used as a ground truth image for one particular module,  $\Delta PL_{OC-SCgt}$ .

Obtaining a  $\Delta PL$  image with data collection through string inverter modulation, Figure 5B, is different than what is illustrated in Figure 5A. Three imaging intervals as illustrated in Figure 4B, each of which contain 4 images for illustrational purposes, are shown. Assuming that the modules in the string are in MPP when the imaging starts,  $i = 1, \dots, N$  BG images are collected in the first imaging interval. One switch to OC condition takes place and  $i = 1, \dots, N$  PL images are collected in the second interval. The mean of the  $N$  images in the two sets is calculated and a difference image between a PL interval and  $BG_1$  interval,  $\Delta PL_j$ , is obtained.<sup>29</sup> This study proposes obtaining the second set of BG images when returning the system to the MPP condition. The reason for this is to try to obtain a better image quality, as averaging over multiple images in same condition is common procedure.<sup>28-31</sup> Since the system needs to return to the MPP condition after the OC condition, acquiring another set of BG images,  $BG_2$ , is less costly than acquiring another set of PL images due to the inverter's reaction time. Another set of BG images results in another  $\Delta PL_j$  image. In that way  $j = 1, \dots, M$ , where  $M=2$  and  $N$  is not equal  $M$ , difference images  $\Delta PL_j$  can be obtained which give the final  $\Delta PL$  image with better quality.

**TABLE 1** Overview of collected image series

Modulation	Operating point	Imaged object	Images per interval	$\Delta PL$ images averaged	Image obtained	Distance (m)	Time (s)
MOSFET instantaneous	OC-SC	1 module		500	$\Delta PL_{OC-SCgt}$	5	270
MOSFET delayed	OC-SC	1 module	20	2	$\Delta PL_{OC-SC}$	5	27
String inverter	OC-MPP	1 module	20	2	$\Delta PL_{OC-MPP}$	5	27
String inverter	OC-MPP	6 modules	20	2	$\Delta PL_{OC-MPP}$	12	27

Experience has shown that acquiring only one series of three intervals BG-PL-BG with the simulated and string inverter delay does not necessarily give a satisfactory result due to pixel values across the module showing an intensity variability. This means that only some BG-PL-BG series produced a good quality  $\Delta PL$  images. For this study, it was therefore necessary to collect several series of three intervals in order to select a satisfactory  $\Delta PL$  image. Data analysis on the different series acquired has shown that the  $\Delta PL_1$  and  $\Delta PL_2$  images might contain intensity variability even though averaging over them can produce a  $\Delta PL$  image which coincides well with the ground truth image.

If illumination during image acquisition varies, it is common to conduct image correction based on pixel values of a white reference imaged together with the object of interest, in this case, the PV modules. This approach was used for data collection with the simulated delay as well as with the delay caused by the inverter. As a preprocessing step, every recorded image is corrected with the pixel average of the white reference according to

$$img_{i,corr} = \frac{img_{i,j}}{\frac{1}{KL} \sum_{k=1}^K \sum_{l=1}^L img_{wr}} \quad (2)$$

where  $img_{corr}$  is the corrected image,  $img$  is the raw image,  $img_{wr}$  is part of the raw image representing the white reference,  $i = 1, \dots, N$  and  $j = 1, \dots, M$ , where  $N$  and  $M$  are the dimensions of the image and  $k = 1, \dots, K$  and  $l = 1, \dots, L$ , where  $K$  and  $L$  are the dimensions of the white reference.

Correction due to varying illumination is not necessary when the switching between two operating points takes place instantaneously, as is the case with instantaneous MOSFET switching for the ground truth image acquisition. Nevertheless, it was performed in this study on all  $\Delta PL$  images for the purpose of better comparison. The  $\Delta PL$  intensity values obtained after correction with the white reference according to Equation (2) are intensity values relative to the white reference values.

### 3.4 | Current readings

The LabView software controlling the data collection procedure contained the possibility of recording the current, voltage, and power readings during both the MOSFET switching as well as inverter

switching procedures. Current readings can be a particularly useful parameter for examining how good the  $\Delta PL_{OC-SC}$  and  $\Delta PL_{OC-MPP}$  images are compared to the ground truth  $\Delta PL_{OC-SCgt}$ . The reason for this is that the detected luminescence is proportional to the difference in current density between the conditions for PL and BG imaging,<sup>34</sup> i.e., OC-SC and OC-MPP conditions.

Thus, the validity of the following expression can be determined

$$\frac{I_{BG} - I_{PL}}{I_{BGgt} - I_{PLgt}} = \frac{\Delta PL}{\Delta PL_{gt}} \quad (3)$$

where  $I_{BG}$  and  $I_{PL}$  are the current measurements during the BG and PL image acquisitions resulting in a  $\Delta PL$  image and  $I_{BGgt}$  and  $I_{PLgt}$  are the current measurements during the BG and PL image acquisitions resulting in a  $\Delta PL_{gt}$  image. Since the current in OC condition is 0A, Equation (3) reduces to

$$\frac{I_{BG}}{I_{BGgt}} = \frac{\Delta PL}{\Delta PL_{gt}} \quad (4)$$

Current readings for image acquisition of one module are shown in Figure 6A–C for instantaneous MOSFET switching, delayed MOSFET switching, and inverter switching, respectively. Sampling was different for the procedures based on MOSFET switching as opposed to inverter modulation. The average values found for SC current during instantaneous and delayed MOSFET modulations,  $I_{SCgt}$  and  $I_{SC}$ , as well as  $I_{MPP}$  during inverter modulation, are listed in Figure 6. The average current values during PL image acquisition (OC condition) for MOSFET modulation are 0A. The current values during inverter modulation, however, are affected by the time it takes for the inverter to be forced into a given operating point. As the  $I_{OC}$  during inverter modulation was set to be at  $0.5\%I_{MPP}$  and  $I_{MPP} \geq 7$  A, the  $I_{OC}$  could not be greater than 0.035A, and  $I_{MPP}$  could not be smaller than 7A for camera to be triggered. These values are confirmed by the current measurements in Figure 6C. The  $I_{OC}$  values slightly above 0A immediately before and after the OC condition should not be taken into consideration because the camera could not be triggered during that time.

The average SC and MPP current values from Figure 6,  $I_{SCgt}$ ,  $I_{SC}$  and  $I_{MPP}$ , are used to evaluate how well the pixel values in the

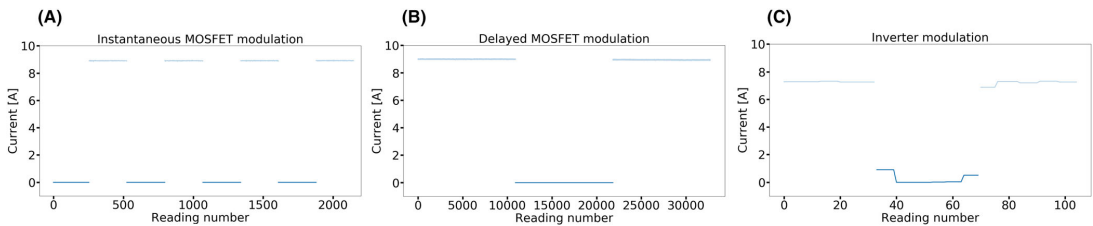


**FIGURE 6** An extract of current readings during ground truth image acquisition averaging to  $I_{SCgt} = 8.946$  A (A), current readings during simulated delayed image acquisition averaging to  $I_{SC} = 8.952$  A (B), current readings during inverter modulation averaging to  $I_{MPP} = 7.276$  A (C)

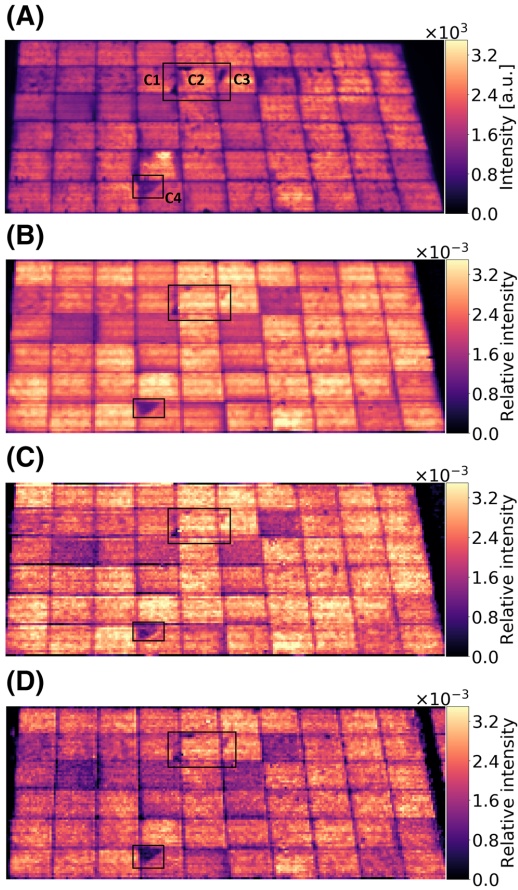


**FIGURE 7**  $EL_{SC}$  image obtained at night with SC current (A), ground truth image  $\Delta PL_{OC-SCgt}$  obtained through instantaneous MOSFET modulation (B), simulated delayed MOSFET modulation giving  $\Delta PL_{OC-SC}$  image (C), and string inverter modulation resulting in  $\Delta PL_{OC-MPP}$  image (D)

$\Delta PL_{OC-SC}$  and  $\Delta PL_{OC-MPP}$  images coincide with Equation (4). According to the current ratio  $I_{SC}/I_{SCgt}=1.000$  and  $I_{MPP}/I_{SCgt}=0.813$ , the pixel ratios  $\Delta PL_{OC-SC}/\Delta PL_{OC-SCgt}$  and  $\Delta PL_{OC-MPP}/\Delta PL_{OC-SCgt}$  are expected to be approximately 1 and 0.8, respectively. This is discussed further in Section 4.2.

## 4 | RESULTS AND DISCUSSION

### 4.1 | Instantaneous versus delayed switching

The  $EL_{SC}$  image of one module obtained in the dark is shown in Figure 7A with intensity values on the color scale. Two black squares

indicate regions with lower pixel values, i.e., increased series resistance. The affected cells are labeled C1-C4. The  $\Delta PL_{OC-SCgt}$  image of the same module obtained through instantaneous MOSFET modulation is shown in Figure 7B. Simulation of the effect of a 5.5-s delay on the image quality when the imaging is conducted in the intervals BG-PL-BG corresponding to operating points SC-OC-SC is illustrated with image  $\Delta PL_{OC-SC}$  in Figure 7C. A  $\Delta PL_{OC-MPP}$  image obtained through switching of the module's operating point with the string inverter between MPP-OC-MPP conditions is shown in Figure 7D. The color scale of the relative intensity values is the same for images (B)–(D) where the regions with higher series resistance are marked with black squares.

The ground truth image  $\Delta PL_{OC-SCgt}$  in (B) and  $\Delta PL_{OC-SC}$  in (C) show mismatch across the cells with respect to  $\Delta PL$  intensities.<sup>34</sup> The fact that the regions with increased series resistance from  $EL_{SC}$  in (A) are visible in (B) and (C) means that the cells are not forced into reverse bias when in SC, or else these regions would not have been visible on images in (B) and (C).<sup>34</sup> Even though the quality of the image in (C) compared to (B) is lower, the broken corners in C1 and C4 are clearly visible. The intensity of the  $\Delta PL$  signal in (C) matches the one in (B).

The pixel values in  $\Delta PL_{OC-MPP}$  in (D) have lower intensity compared to (B) and (C), which is to be expected because the current passing through the module in MPP condition is approximately 20% lower according to Figure 6, thus resulting in higher emission of the PL signal in this condition. This is also visible in the two regions with increased series resistance in C2 and C3. The broken corners in C1 and C4 are clearly visible in (D) as well, but according only to the color scale for (B)–(D), it is not particularly clear whether the  $\Delta PL$  signal is weaker in these corners in (D) compared to (B) and (C).

Further analysis was conducted on the broken corner in C4 comparing it to the intensity of the rest of that cell because it offers the biggest number of pixels which represents a region with increased series resistance. The intensity of both the intact region and the broken corner of C4 is weaker in the  $\Delta PL_{OC-MPP}$  than in the  $\Delta PL_{OC-SCgt}$  image. However, the intensity of the rest of the cell in  $\Delta PL_{OC-MPP} = 0.771\Delta PL_{OC-SCgt}$ , while the broken corner in the  $\Delta PL_{OC-MPP}$  image has an average value of  $0.548\Delta PL_{OC-SCgt}$ . This indicates lower values in the  $\Delta PL_{OC-MPP}$  image in the area affected by series resistance due to lower current extraction and thus higher signal in the MPP condition.<sup>29</sup> Lower current extraction in MPP results in higher PL signal intensity in a part affected by higher series resistance compared to the rest of the cell. This in turn results in lower  $\Delta PL$  signal compared to the rest of the cell.

### 4.2 | Current ratios versus $\Delta PL$ ratios

In order to examine further  $\Delta PL_{OC-SC}$  and  $\Delta PL_{OC-MPP}$  images with respect to the ground truth image  $\Delta PL_{OC-SCgt}$ , the current ratios are compared with image ratios as explained in Section 3.4. The image ratios  $\Delta PL_{OC-SC}/\Delta PL_{OC-SCgt}$  and  $\Delta PL_{OC-MPP}/\Delta PL_{OC-SCgt}$  are illustrated in Figure 8A,B, respectively. The ratio values in each pixel show



that the image in (A) has values around 1, corresponding to the current ratio  $I_{SC}/I_{SCgt}$  found in Section 3.4, while the values in (B) show bigger variation around 0.8–0.9 for the current ratio  $I_{MPP}/I_{SCgt}$ .

A black square is indicated on the image in (A) and a blue square in (B) within which an average is found across the columns plotted in Figure 8C. The black line in (C) varies around 1, which indicates that the values in the  $\Delta PL_{OC-SC}$  are on average the same as the values in the  $\Delta PL_{OC-SCgt}$  image. The blue curve in (C) is on the level of approximately 0.8, which indicates that the values in the  $\Delta PL_{OC-MPP}$  image are on average approximately 0.8 of the values in the  $\Delta PL_{OC-SCgt}$  image across the length of the module. This corresponds to the ratio of the current readings. The spikes in (C), particularly visible on the blue curve, indicate sudden changes in signal in the white back-sheet regions between cells.

### 4.3 | Imaging of multiple modules

The approach of using the string inverter to perform modulation of the operating point makes it possible to image several modules at the

same time enabling a more effective procedure. Figure 9 shows the  $\Delta PL_{OC-MPP}$  image of six modules imaged at the same time from 12-m distance. The two squares on the lower left module enclose the same two areas as in Figure 7. The broken corner on cell C4 is visible also on this image. The series resistance affected areas on cells C1–C3 seem to be barely visible. The resolution of 2.6 cm/pixel is too low to make an evaluation about whether C1–C3 might be affected by series resistance.

The validity of the  $\Delta PL$  values for the rest of the modules in Figure 9 cannot be evaluated based on the present data. Nevertheless, the analysis in Sections 4.1 and 4.2 has shown that a delay of several seconds between the operating points of a module string can still produce a valid  $\Delta PL$  image in which series resistance can be visible. The ratio  $\Delta PL_{OC-MPP}/\Delta PL_{OC-SCgt}$  coincides with the ratio of current measurements during acquisition of the  $\Delta PL_{OC-MPP}$  and  $\Delta PL_{OC-SCgt}$  images. This leaves us to believe that the  $\Delta PL_{OC-MPP}$  result from the remaining five modules in Figure 9 is reliable and that these modules do not suffer from severely damaged cells.

These observations make it necessary to elaborate on what kind of information can be expected to be obtained with images shown in Figures 7 and 9. Certain defects can be expected to be visible from long distance with high throughput of several modules per image. These concern the intactness of a string as well as large area damage with strong impact on power output.<sup>35</sup> Partially broken cells and inactive areas should also be visible if several modules are imaged simultaneously.<sup>35</sup> However, for certain applications, a much higher resolution is necessary such as for visualizing micro-cracks, for detection of which  $10^{28}$  or 12 cells<sup>35</sup> have to be imaged at a time.

This study is a proof of concept, and the method needs to be further improved. A thorough investigation into the reasons for intensity variability mentioned in Section 3.3 still remains to be done. One of the reasons is even the smallest variation in the illumination which the correction with the white reference, as described in Equation (2), cannot account for. The weather conditions should be clear sky conditions. The smallest visible disturbances in the form of clouds have detrimental effects on the image quality. This is particularly so because the  $V_{OC}$  per cell of the modules studied is lower compared to current state-of-the-art PV modules. For example, some studies on

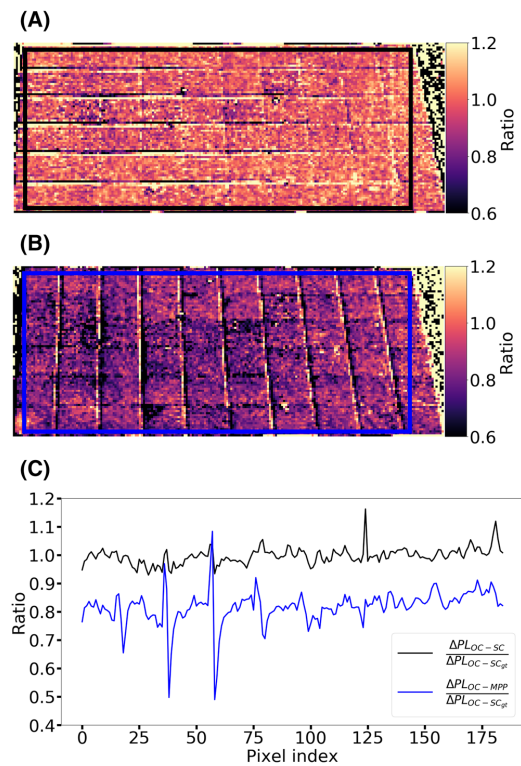


**FIGURE 8** Image ratio  $\Delta PL_{OC-SC}/\Delta PL_{OC-SCgt}$  (A),  $\Delta PL_{OC-MPP}/\Delta PL_{OC-SCgt}$  (B) and the average ratio values within the black and blue squares in (A) and (B) across the columns (C)

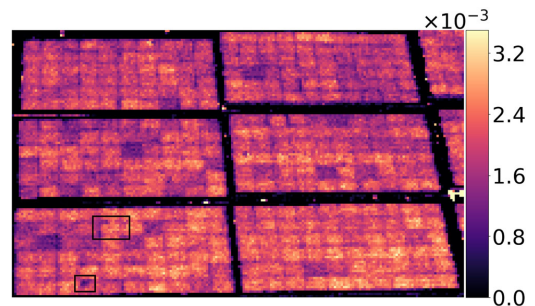


**FIGURE 9**  $\Delta PL_{OC-MPP}$  image of six modules imaged at the same time

detection of the PL signal in outdoor conditions have been based on PV modules with  $V_{OC} = 660$  mV/cell<sup>29</sup> and  $V_{OC} = 730$  mV/cell.<sup>31</sup> Compared to the modules used in this study with  $V_{OC} = 628$  mV/cell, as mentioned above, they emit a PL signal which is approximately 3.5 and 50 times stronger. Thus, applying this method on for example PERC modules, which are currently the most widely installed PV modules,<sup>37</sup> should give better results.

The Xeva camera used at the time of the data collection was rebuilt from the sensor of a 10-year-old defect InGaAs hyperspectral push broom camera. The settings for this rebuilt camera were limited, and a very small aperture opening had to be applied in order to get the image depth required for a whole module string. As a consequence, the exposure times were as long as 200 ms. A higher sensitivity and sharper images are expected with a dedicated camera with an optimized setting for this type of application. With respect to the camera apparatus, it is also necessary to investigate its vibrations<sup>33</sup> in future studies, which could lead to a better alignment of images and thus reduction of spikes in Figure 8C.

## 5 | CONCLUSION

Recent developments in PL imaging based on sunlight excitation make this spectral imaging method more available for the study of degradation mechanisms in silicon modules in the field. Firstly, the challenges with BG signal caused by sunlight need to be surpassed. This can be done by subtracting the reflected sunlight from the overall detected signal. Methods that have already been tested suggest that it can be achieved through image acquisition in two different operating points.

This study is a proof of concept and presents an approach which makes it possible to image several modules in a string as well as several strings simultaneously without the need to physically interfere with the PV system. The method enables switching the operating point of several modules or strings through wireless communication with one or several string inverters. Due to the string inverter's reaction time, the change in illumination causes the image quality to deteriorate. However, these lower quality images can still be used for identification of certain degradation mechanisms such as large area damage as well as broken and inactive cells. Further studies and an up-to-date camera are needed to optimize the method. Applying the method on state-of-the-art PV modules with higher  $V_{OC}$  than what has been the case in this study should also give better results. The method can potentially be used within the scope of UAV inspection. However, this would most likely induce noise due to vibrations and turbulence. This may be overcome by advanced image analysis including vibrational corrections.

## ACKNOWLEDGEMENTS

This work was performed within The Norwegian Research Center for Sustainable Solar Cell Technology (FME SUSOLTECH, project number 257639/E20). The center is co sponsored by the Research Council of Norway and its research and industry partners.

## CONFLICT OF INTEREST

The authors declare that they have no conflicts of interest.

## DATA AVAILABILITY STATEMENT

The data that support the findings of this study are available from the corresponding author upon reasonable request.

## ORCID

Marija Vuković  <https://orcid.org/0000-0003-1148-5958>

## REFERENCES

- Augarten Y, Trupke T, Lenio M, et al. Luminescence shunt imaging: Qualitative and quantitative shunt images using photoluminescence imaging. In: 24th European Photovoltaic Solar Energy Conference; 2009:21-25.
- Doll B, Kornhas J, Hepp J, et al. Towards true contactless outdoor luminescence of silicon photovoltaic modules with inhomogeneous small area excitation source. In: IEEE 7th World Conference on Photovoltaic Energy Conversion; 2018:390-394.
- Hinken D, Ramspeck K, Bothe K, Fischer B, Brendel R. Series resistance imaging of solar cells by voltage dependent electroluminescence. *Appl Phys Lett*. 2007;91(18):182104.
- Kampwerth H, Trupke T, Weber JW, Augarten Y. Advanced luminescence based effective series resistance imaging of silicon solar cells. *Appl Phys Lett*. 2008;93(20):202102.
- Kropp T, Schubert M, Werner JH. Quantitative prediction of power loss for damaged photovoltaic modules using electroluminescence. *Energies*. 2018;11(5):1172.
- Mehl T, Di Sabatino M, Adamczyk K, Burud I, Olsen E. Defects in multicrystalline Si wafers studied by spectral photoluminescence imaging, combined with ebsd and dislocation mapping. *Energy Proc*. 2016;92:130-137.
- Potthoff T, Bothe K, Eitner U, Hinken D, Köntges M. Detection of the voltage distribution in photovoltaic modules by electroluminescence imaging. *Progress Photovoltaics: Res Appl*. 2010;182:100-106.
- Ramspeck K, Bothe K, Hinken D, Fischer B, Schmidt J, Brendel R. Recombination current and series resistance imaging of solar cells by combined luminescence and lock-in thermography. *Appl Phys Lett*. 2007;90:153502.
- Spataru S, Hacke P, Sera D, Glick S, Kerekes T, Teodorescu R. Quantifying solar cell cracks in photovoltaic modules by electroluminescence imaging. In: IEEE 42nd Photovoltaic Specialist Conference; 2015:1-6.
- Trupke T, Bardos R A, Abbott M & Pink E. Progress with luminescence imaging for the detection of cracks in silicon wafers and solar cells. In: IEEE 7th World Conference on Photovoltaic Energy Conversion; 2007:22-31.
- Trupke T, et al. Spatially resolved series resistance of silicon solar cells obtained from luminescence imaging. *Appl Phys Lett*. 2007;90(9):93506.
- Trupke T, Mitchell B, Weber JW, McMillan W, Bardos RA, Kroez R. Photoluminescence imaging for photovoltaic applications. *Energy Proc*. 2012;15:135-146.
- Zafirovska I, Juhl MK, Trupke T. Efficient detection of finger interruptions from photoluminescence images. In: 33rd European Photovoltaic Solar Energy Conference and Exhibition; 2017:1689-1693.
- Zafirovska I, Juhl MK, Trupke T. Comparison of line scan luminescence imaging techniques for defect characterisation in crystalline silicon solar modules. In: IEEE 7th World Conference on Photovoltaic Energy Conversion; 2018:1364-1369.
- Coello J. Introducing electroluminescence technique in the quality control of large pv plants. In: 6th European Photovoltaic Solar Energy Conference and Exhibition; 2011:3469-3472.

16. Navarrete M, et al. On-site inspection of pv modules using an internationally accredited pv mobile lab: a three-year experience operating worldwide. In: 31st European Photovoltaic Solar Energy Conference and Exhibition; 2015:1689-1699.
17. Bertani D, Liciotti C, Guastella S & Camilloni C. Investigation and diagnostic tool comparison: infrared thermography vs electroluminescence. In: 32nd European Photovoltaic Solar Energy Conference and Exhibition; 2016:2098-2104.
18. de Oliveira AKV, Bedin C, de Andrade Pinto GX, et al. Low-cost aerial electroluminescence (ael) of pv power plants. In: IEEE 46th Photovoltaic Specialists Conference; 2019:532-537.
19. Koch S, Weber T, Sobotta C, Fladung A, Clemens P, Berghold J. Outdoor electroluminescence imaging of crystalline photovoltaic modules: Comparative study between manual ground-level inspections and drone-based aerial surveys. In: 32nd European Photovoltaic Solar Energy Conference and Exhibition; 2016:1736-1740.
20. dos Reis Benatto GA, Chi M, Jensen OB, et al. Photoluminescence imaging induced by laser line scan: study for outdoor field inspections. In: 7th World Conference on Photovoltaic Energy Conversion; 2018:395-399.
21. dos Reis Benatto GA, Chi M, Santamaria Lancia AA, et al. Scaling up laser line photoluminescence imaging for outdoor inspections. In: 35th European Photovoltaic Solar Energy Conference and Exhibition; 2018:1352-1354.
22. Doll B, Pickel T, Schreer O, et al. High-throughput, outdoor characterization of photovoltaic modules by moving electroluminescence measurements. *Opt Eng.* 2019;58(8):83105.
23. Adams J, Doll B, Buerhop C., et al. Non-stationary outdoor measurements with a fast and highly sensitive ingaas camera. In: 32nd European Photovoltaic Solar Energy Conference and Exhibition; 2016:1837-1841.
24. dos Reis Benatto GA, Riedel N, Mantel C, et al. Luminescence imaging strategies for drone-based pv array inspection. In: 33rd European Photovoltaic Solar Energy Conference and Exhibition; 2017: 2016-2020.
25. dos Reis Benatto GA, Mantel C, Lancia AAS, et al. Image processing for daylight electroluminescence pv imaging acquired in movement. In: 35th European Photovoltaic Solar Energy Conference and Exhibition; 2018:2005-2009.
26. dos Reis Benatto GA, Mantel C, Spataru S, et al. Drone-based daylight electroluminescence imaging of pv modules. *IEEE J Photovoltaics.* 2020;10(3):872-877.
27. Bhoopathy R, Kunz O, Juhl M, Trupke T, Hameiri Z. Inspecting series resistance effects and bypass diode failure using contactless outdoor photoluminescence imaging; 2018:377-380.
28. Bhoopathy R, Kunz O, Juhl M, Trupke T, Hameiri Z. Outdoor photoluminescence imaging of photovoltaic modules with sunlight excitation. *Progress Photovoltaics: Res Appl.* 2018;26(1):69-73.
29. Bhoopathy R, Kunz O, Juhl M, Trupke T, Hameiri Z. Outdoor photoluminescence imaging of solar panels by contactless switching: technical considerations and applications. *Progress Photovoltaics: Res Appl.* 2020;28(3):217-228.
30. Guada M, Moretón A, Rodríguez-Conde S, et al. Daylight luminescence system for silicon solar panels based on a bias switching method. *Energy Sci Eng.* 2020;8(11):3839-3853.
31. Koester L, Astigarraga A, Lindig S, Moser D. Development of daylight photoluminescence technique for photovoltaic modules and investigation of temperature dependency. In: 37th European Photovoltaic Solar Energy Conference and Exhibition; 2020:908-913.
32. Kropp T, Berner M, Stoicescu L, Werner JH. Self-sourced daylight electroluminescence from photovoltaic modules. *IEEE J Photovoltaics.* 2017;7(5):1184-1189.
33. Mantel C, dos Reis Benatto GA, Riedel N, et al. Snr study of outdoor electroluminescence images under high sun irradiation. In: IEEE 7th World Conference on Photovoltaic Energy Conversion; 2018: 3285-3289.
34. Silverman TJ, Deceglie MG, VanSant K, Johnston S, Repins I. Illuminated outdoor luminescence imaging of photovoltaic modules. In: IEEE 44th Photovoltaic Specialist Conference; 2017:3452-3455.
35. Stoicescu S, Reuter M, Werner JH. Days: Luminescence imaging of pv modules in daylight. In: 29th European Photovoltaic Solar Energy Conference and Exhibition; 2014:2553-2554.
36. Doll B, Hepp J, Hoffmann M, et al. Photoluminescence for defect detection on full-sized photovoltaic modules. *IEEE J Photovoltaics.* 2021;11(6):1419-1429.
37. Herrmann W, Eder G, Farnung B, Friesen G, Köntges M, Kubicek B, Kunz O, Liu H, Parlevliet D, Tsanakas I, Vedde J, et al. Qualification of photovoltaic (pv) power plants using mobile test equipment. *Int Energy Agency Photovoltaic Power Syst Programme T13-24.* 2021; 13-24:139-160.
38. Stoicescu S & Reuter M. Days contactless measurements of pid shunt resistance in installed pv modules. In: 35th European Photovoltaic Solar Energy Conference and Exhibition; 2018:1337-1339.
39. Kunz O, Rey G, Juhl MK & Trupke T High throughput outdoor photoluminescence imaging via pv string modulation. In: 2021 IEEE 48th Photovoltaic Specialists Conference (PVSC); 2021:346-350.
40. Jahn U, Köntges M, Parlevliet D, Paggi M, Tsanakas I, Stein J S, Berger K A, Ranta S, French R H, Richter M, Tanahashi T, et al. Review on infrared and electroluminescence imaging for pv field applications. *Int Energy Agency Photovoltaic Power Syst Programme.* 2018;13-10:51-70.

**How to cite this article:** Vuković M, Eriksdatter Høiaas I, Jakovljević M, Svarstad Flø A, Olsen E, Burud I. Photoluminescence imaging of silicon modules in a string. *Prog Photovolt Res Appl.* 2022;30(4):436-446. doi:10.1002/PIP.3525



# Appendix B

## Paper B



# Outdoor Photoluminescence and Electroluminescence Imaging of Photovoltaic Silicon Modules in a String

Marija Vuković<sup>a)</sup>, Ingeborg Eriksdatter Høiaas, Marko Jakovljević, Andreas Svarstad Flø, Espen Olsen, Ingunn Burud

*Norwegian University of Life Sciences, Universitetstunet 3, 1433 Ås, Norway*

<sup>a)</sup> Corresponding author: marija.vukovic@nmbu.no

**Abstract.** Spectral imaging techniques are powerful tools for surveillance and monitoring of degradation mechanisms in PV power plants. Luminescence images of silicon solar modules have until recently been predominantly acquired in controlled laboratory settings. Recent attempts have been made in detecting photoluminescence from silicon PV modules in daylight. This study aims to present an approach for detection of photoluminescence with sunlight excitation. It enables imaging of several modules simultaneously by changing the string's operating point through wireless, contactless communication with the string inverter. The advantage of this approach compared to electroluminescence imaging is that it can be conducted in daylight and it does not require wiring of the modules. However, due to the string inverter's reaction time, the change in illumination causes image quality to deteriorate compared to the methods for photoluminescence imaging using instantaneous switching of the operating point and electroluminescence imaging. A comparison is conducted between photoluminescence images acquired through string inverter modulation and images acquired through instantaneous switching as well as with electroluminescence images. It shows that the photoluminescence images obtained through string inverter modulation can be used for identification of degradation mechanisms such as series resistance. Further studies are needed to improve the image quality and potentially use it in UAV inspections.

## INTRODUCTION

The basis of photoluminescence (PL) imaging is charge carrier excitation with an illumination source which can be a laser [1], a LED [2] or sunlight [3]-[8]. However, the reflected light from the illumination source needs to be accounted for. In the case of sun's excitation, the reflected sunlight and the emitted PL signal overlap. The need to subtract the unwanted reflection from the module has so far resulted in two approaches. One of them is based on conducting imaging with the module at a constant operating point by recording images with different optical bandpass filters. The PL signal is obtained by subtracting the images with low or no PL intensity from the images with high PL intensity [7]. The other approach is based on collecting images with the same optical filter while switching between a module's two operating points in which the current extraction differs e.g. the intensity of the PL signal differs. Subtracting the images recorded in the condition with the weaker PL signal from the images with the stronger PL signal gives a difference signal  $\Delta PL$ .

Technical considerations when changing a module's operating point have resulted in different solutions. Solid state-relay [6] such as MOSFET transistor connected to the module's terminals [3] or controlling the current extraction by covering a cell in a sub-string with a LED lamp [4] enable instantaneous switching of the operating point. Combining the latter approach with a PV system containing an inverter [5] or using only an inverter [8] results in delayed switching due to inverter's reaction time. This in turn leads to bigger change in illumination conditions during image acquisition and thus lower image quality.

So far studies have been carried through on one module at a time. In the current study we demonstrate how  $\Delta PL$  imaging can be conducted on a string of several modules simultaneously. This approach makes  $\Delta PL$  imaging possible through wireless communication with the string inverter for the modulation of the operating point. Furthermore, we

investigate possibilities of this approach by comparing the  $\Delta$ PL images obtained this way with electroluminescence (EL) images as well as with an already tested  $\Delta$ PL imaging method [3].

## EXPERIMENTAL SETUP AND DATA COLLECTION

The intensity of the luminescence signal over an area of a silicon solar cell is proportional to the diode junction voltage of that region. Image acquisition can be carried through by switching between any two operating points in which the voltage differs. The bigger the difference in voltage between the two operating points, the bigger is  $\Delta$ PL and the better is the image quality. The choice of the two operating points may depend on the equipment available. The maximum  $\Delta$ PL obtained with string inverter modulation is between open-circuit (OC) and maximum power point (MPP) conditions, which is used in this study.

The setup for  $\Delta$ PL imaging of a module string with modulation through a string inverter is shown in Fig. 1. The string consists of 12 series connected multi-crystalline silicon (Si) modules of type *SweModule Inceptio 250F* ( $P_{NOM}=250$  W,  $I_{SC}=8.80$  A,  $V_{OC}=37.7$  V at STC) and the string inverter *Fronius Primo 3.0*. The camera used is a short-wave infrared camera of type *Raptor Photonics Owl 640S* with an InGaAs detector, optical range 900 nm – 1700 nm and 640x512 resolution. The synchronization between camera triggering and the string's operating point was achieved with a computer equipped with frame grabber and camera software. Communication with the inverter was established through communication protocol Modbus over WiFi. The operating point was switched by controlling the output power between maximum in the MPP and minimum in OC condition. A Spectralon white reference (25% reflection) was included in all the images.

The method was first tested by imaging one module. The  $\Delta$ PL image obtained through string inverter modulation is here referred to as  $\Delta PL_{OC-MPP}$ . It is validated and compared with two EL images,  $EL_{SC}$  and  $EL_{0,ISC}$ , acquired with short-circuit current  $I_{SC}$  and 10% of  $I_{SC}$  in dark [9] as well as with a  $\Delta PL_{OC-SC}$  image obtained with an already proven  $\Delta$ PL imaging method consisting of instantaneous switching of operating point between OC and SC using a MOSFET transistor as a switch [3]. The two EL images were obtained by averaging 200 EL images and subtracting the average of 200 background (BG) images. The  $\Delta PL_{OC-SC}$  image was obtained by averaging 500 PL-BG differences obtained in OC and SC conditions. After the preliminary tests and analysis on one module, a final  $\Delta PL_{OC-MPP}$  image was obtained for several modules simultaneously.

Inverter's reaction time, which was for this inverter registered to be approximately 6 seconds, is the reason why it is preferable to switch between two operating points as few times as possible while obtaining  $\Delta PL_{OC-MPP}$  images. The data collection and processing for the data set obtained with inverter modulation are illustrated in Fig. 2. A set of 100-200 BG images is collected in the MPP condition. The operating point is switched to OC and a new set of equally many PL images is recorded before the operating point is switched back to MPP when the last set of BG images is recorded.

The data processing starts with white reference correction due to considerable variation in illumination caused by the inverter's reaction time. After that an average image is calculated for every image set. With three average images it is possible to obtain two  $\Delta PL_{OC-MPP}$  images which are averaged into a final  $\Delta PL_{OC-MPP}$  with better image quality than its constituent parts. Correction with white reference was carried through on every image acquired through inverter modulation as well as on images that result in  $\Delta PL_{OC-SC}$  image for the purpose of easier comparison with  $\Delta PL_{OC-MPP}$ .

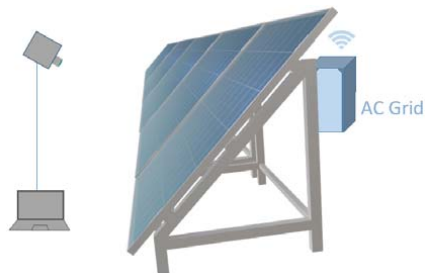


FIGURE 1. Equipment used for acquisition of  $\Delta$ PL through wireless string inverter communication.



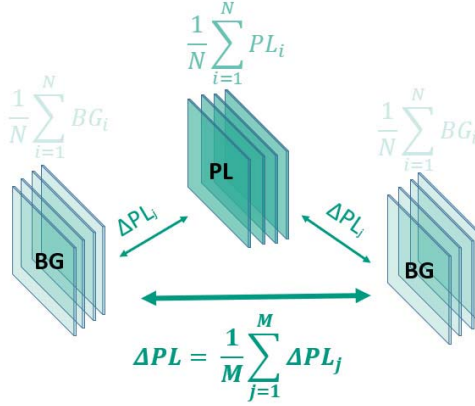


FIGURE 2. Data processing of image sets acquired in two operating points modulated through the string inverter.

## RESULTS AND DISCUSSION

The results of data collection carried through on one module are shown in Fig. 3. EL images obtained with two different current levels,  $I_{SC}$  and  $I_{0,1SC}$ , are displayed in (a) and (b).  $\Delta PL_{OC-SC}$  image acquired through instantaneous MOSFET modulation between OC and SC conditions is displayed in (c), while the  $\Delta PL_{OC-MPP}$  image obtained with the string inverter modulation between OC and MPP operating points is shown in (d). It is visible that images (a)-(c) have a considerably better quality. More details are visible on those images at the same time as they appear clearer. The reason for that is that  $EL_{SC}$  and  $EL_{0,1SC}$  images were collected in dark, while  $\Delta PL_{OC-SC}$  image was acquired through instantaneous modulation in daylight during which the sunlight between two images in 500 pairs collected in OC-SC conditions changed minimally. The effect of the reaction time of the inverter is visible in the image quality in (d) compared to (a)-(c). The blue and red squares on all four images mark the areas with regions of higher series resistance. These areas are emphasized because the series resistance problems are visible in all three images (a)-(c) as well as in (d) despite the lower image quality. The areas within the blue and red squares are enlarged in Fig. 4 and Fig. 5.

With respect to  $EL_{SC}$  images, there will be high contrast between a healthy region with high values compared to a region with increased series resistance with considerably lower values [9]. This can be observed in Fig. 4 (a)-(b) showing the areas within the blue and red squares from Fig. 3. In both  $EL_{SC}$  images in (a) and (b) there is a high contrast between the disconnected regions and the rest of the cells.

In  $EL_{0,1SC}$  images, the same regions might have a high contrast or reduced contrast compared to the rest of the cells depending on the degree of electrical disconnection of that region from the rest of the cell [9]. High contrast on  $EL_{0,1SC}$  images implies electrically disconnected regions, while reduced contrast in  $EL_{0,1SC}$  images implies partially electrically disconnected regions. This is illustrated in Fig. 4 (c)-(d).  $EL_{0,1SC}$  image in (c) shows a reduced contrast between the disconnected region and the rest of the cell compared to the same  $EL_{SC}$  image in (a). It almost seems as if there is no contrast apart from the visible crack around the upper left corner. The  $EL_{0,1SC}$  image in (d) seems to display a much higher contrast like the one in (c). This indicates that series resistance in disconnected region in (a) and (c) is lower compared to series resistance in regions in (b) and (d).

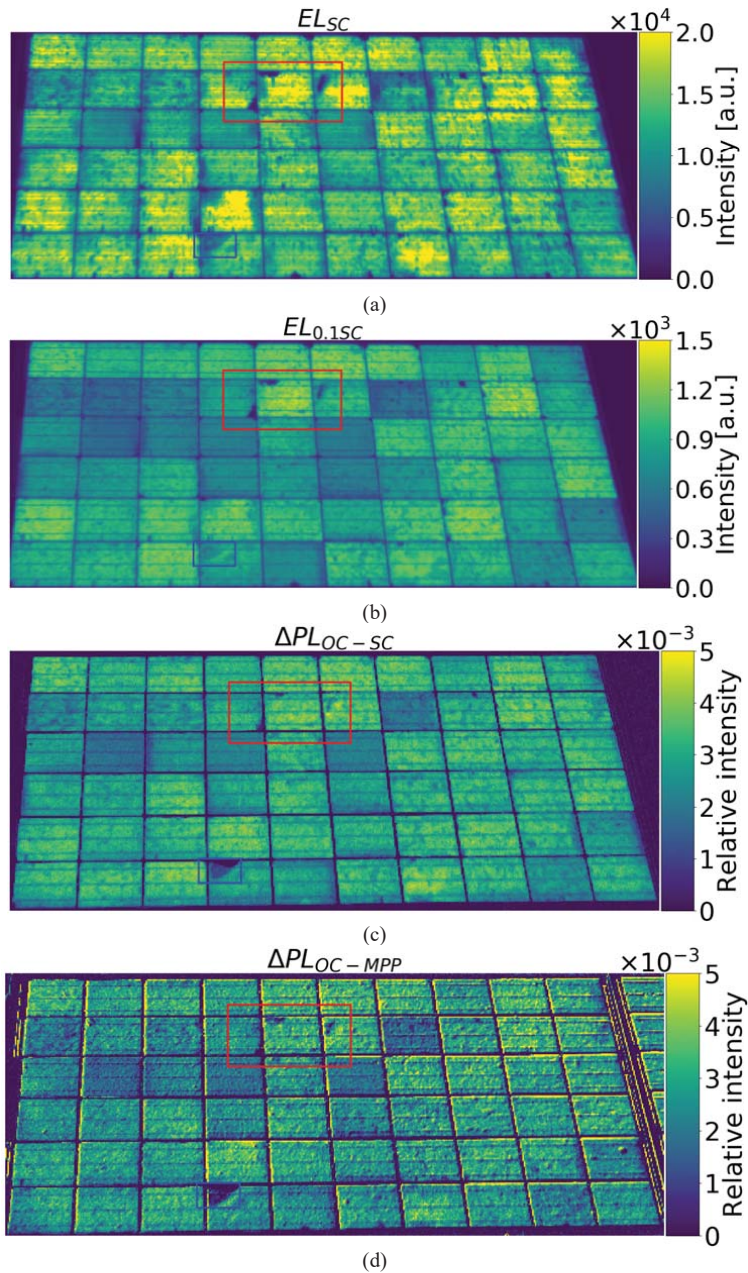


**FIGURE 3.** EL images of a module acquired with different current levels, SC (a) and 0.1SC (b), and  $\Delta PL$  images of the same module obtained with different current extraction levels, SC (c) and MPP (d). The intensity scale in (c) and (d) is the same.

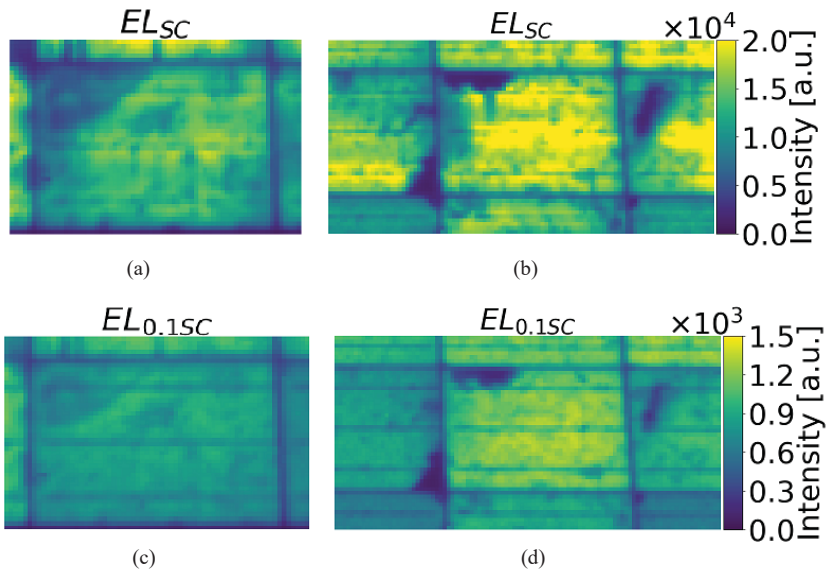


FIGURE 4.  $EL_{SC}$  images of the blue and red squares from Fig. 3 with the same intensity scale in (a) and (b).  $EL_{0.1SC}$  images of the same regions with the same intensity scale in (c) and (d).

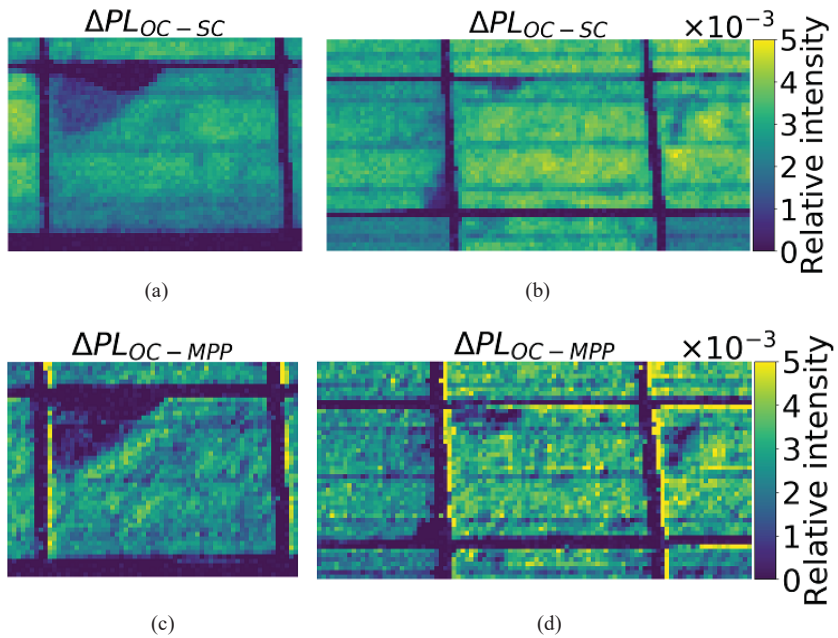


FIGURE 5.  $\Delta P_{LOC-SC}$  and  $\Delta P_{LOC-MPP}$  images of the blue and red squares from Fig. 3. The intensity scale is the same in (a)-(d).

The same regions from Fig. 4 are displayed in Fig. 5 on  $\Delta PL_{OC-SC}$  and  $\Delta PL_{OC-MPP}$  images. The blue and red regions of  $\Delta PL_{OC-SC}$  are displayed in (a) and (b), while the same regions of  $\Delta PL_{OC-MPP}$  are shown in (c) and (d). As opposed to the above analysis of  $EL_{SC}$  and  $EL_{0,1SC}$ , which is based on the comparison between the electrically disconnected regions with the rest of the cells, care should be taken when comparing the  $\Delta PL$  images in the same way. This is because of the visibly lower image quality of the  $\Delta PL_{OC-MPP}$  image. There are regions with higher intensity in Fig. 5 (c)-(d) than in Fig. 5 (a)-(b) such as the horizontal and vertical yellow lines on the edges of the cells. This should not be the case because, in general, current extraction in the MPP condition during  $\Delta PL_{OC-MPP}$  imaging is lower compared to current extraction in the SC condition during  $\Delta PL_{OC-SC}$  imaging. The PL signal is thus higher in the MPP condition compared to the SC condition. The  $\Delta PL_{OC-MPP}$  difference should therefore be lower than the  $\Delta PL_{OC-SC}$  difference.

However, it can be observed that these theoretical considerations are met when comparing the regions with increased series resistance in (c) and (d) ( $\Delta PL_{OC-MPP}$ ) with those in (a) and (b) ( $\Delta PL_{OC-SC}$ ). The parts of cells affected by series resistance appear darker in (c) and (d) compared to (a) and (b). The  $\Delta PL$  image with higher current extraction,  $\Delta PL_{OC-SC}$ , has higher values compared to the image with lower current extraction,  $\Delta PL_{OC-MPP}$ .

How the  $\Delta PL$  values change in series resistance affected regions depending on current extraction is conditioned by the level of series resistance. As the current extraction level changes, the region with lower series resistance displays a stronger  $\Delta PL$  intensity change than a region with higher series resistance [5]. Based on the above analysis of the EL images, the region in Fig. 4 (a) and (c) has lower series resistance than the regions in Fig. 4 (b) and (d). This means that as the current extraction level changes from SC to MPP in the  $\Delta PL$  images, the disconnected region in Fig. 5 (c) would display a stronger  $\Delta PL$  intensity change compared to (a) than the disconnected regions in Fig. 5 (d) compared to (b). However, as mentioned above, the image quality of  $\Delta PL_{OC-MPP}$  is not good enough for this type of conclusion to be made based on the images in Fig. 5. In Fig. 5 (c) and (d) some pixels even have negative values which should physically not be possible. Image quality needs therefore to be improved before such type of analysis can be made.

An example of the possibilities with this type of imaging is displayed in Fig. 6. This  $\Delta PL_{OC-MPP}$  image shows 6 modules imaged simultaneously. The image quality seems to be the same as in Fig. 3 (d). The regions in red and blue squares from Fig. 3 are also emphasized in Fig. 6. The regions with increased series resistance are visible, particularly the region in the blue square. The three regions in the red square are also visible, but seem to be more influenced by the increased distance between the camera and the modules.

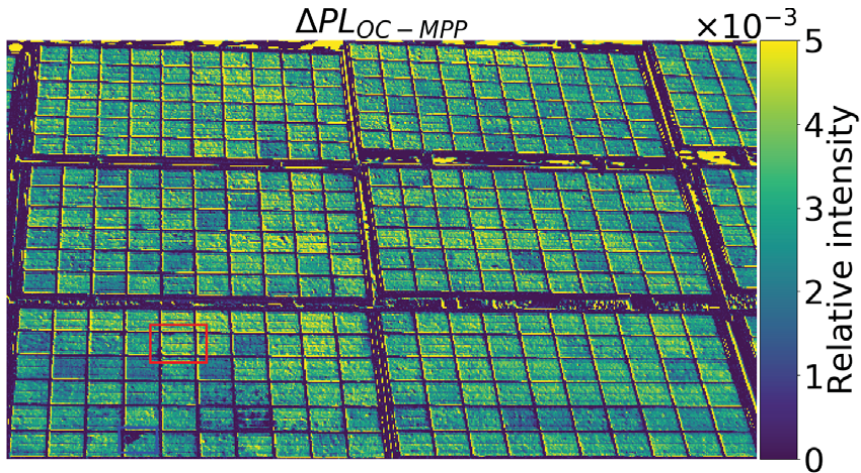


FIGURE 6.  $\Delta PL_{OC-MPP}$  image acquired simultaneously of 6 modules. The blue and red squares from Fig. 3 are also displayed here.

## CONCLUSION

Recent developments in photoluminescence imaging based on sunlight excitation make this spectral imaging method more available for the study of degradation mechanisms in silicon modules in the field. Firstly, the challenges with background noise caused by sunlight need to be surpassed. This can be done by subtracting the reflected sunlight from the overall detected signal. Methods that have already been tested suggest that it can be achieved through image acquisition in two different operating points of a module. This study presents an approach which makes it possible to image several modules in a string simultaneously and contactless. The method requires switching of the modules' operating point through wireless communication with the string inverter. The advantage compared to the EL imaging is that it can be conducted in daylight at the same time as no wiring is necessary.

Due to the string inverter's reaction time, the change in illumination causes image quality of  $\Delta$ PL images obtained in this way to deteriorate compared to EL images and  $\Delta$ PL images acquired with instantaneous switching of operating point. However, a comparison of a  $\Delta$ PL image of one module acquired through string inverter modulation with EL images and a  $\Delta$ PL<sub>OC-SC</sub> image of the same module shows great potential when it comes to identifying degradation mechanisms such as series resistance. How well they are visible depends on the resolution e.g. distance between the camera and the modules. Further studies are needed to increase the image quality and potentially use it in UAV inspections.

## ACKNOWLEDGMENTS

This work was performed within The Norwegian Research Center for Sustainable Solar Cell Technology (FME SUSOLTECH, project number 257639/E20). The center is co-sponsored by the Research Council of Norway and its research and industry partners.

## REFERENCES

1. T. Mehl, M. Di Sabatino Lundberg, K. Adamczyk, I. Burud and E. Olsen, *Energy Procedia* **92**, 130-137 (2018).
2. B. Doll, J. Kornhas, J. Hepp, C. Buerhop, J. Hauch, C. Camus and C. J. Brabec, "Towards true contactless outdoor luminescence of silicon photovoltaic modules with inhomogeneous small area excitation source", *IEEE 7<sup>th</sup> World Conference on Photovoltaic Energy Conversion Proceedings*, 2018, pp. 390-394.
3. T. J. Silverman, M. G. Deceglie, K. Vansant, S. Johnston and I. Repins, "Illuminated outdoor luminescence imaging of photovoltaic modules", *IEEE 44<sup>th</sup> Photovoltaic Specialist Conference Proceedings*, 2017, pp. 3452–3455.
4. R. Bhoopathy, O. Kunz, M. Juhl, T. Trupke and Z. Hameiri, *Progress in Photovoltaics: Research and Applications* **26**, 69–73 (2018).
5. R. Bhoopathy, O. Kunz, M. Juhl, T. Trupke and Z. Hameiri, *Progress in Photovoltaics: Research and Applications* **28**, 217-228 (2020).
6. M. Guada, Á. Moretón, S. Rodríguez-Conde, L. A. Sánchez, M. Martínez, M. Á. González, J. Jiménez, L. Pérez, V. Parra and O. Martínez, *Energy Science and Engineering* **8**, 3839-3853 (2020).
7. O. Kunz, G. Rey, R. Bhoopathy, Z. Hameiri and T. Trupke, "Outdoor PL imaging of crystalline silicon modules at constant operating point", *47<sup>th</sup> IEEE Photovoltaic Specialists Conference Proceedings*, 2020, pp. 2140-2143.
8. L. Koester, A. Astigarraga, S. Lindig and D. Moser, "Development of daylight photoluminescence technique for photovoltaic modules and investigation of temperature dependency", *EU PVSEC Proceedings*, 2020, pp. 908-913.
9. International Electrotechnical Commission, "Photovoltaic Devices-Part 13: Electroluminescence of photovoltaic modules", *IEC TS 60904-13* (2018).



# Appendix C

## Paper C





## Non-invasive Photoluminescence Imaging of Silicon PV Modules in Daylight

M. Vuković, M. Jakovljević, A.S. Flø, E. Olsen, I. Burud<sup>1</sup>

Faculty of Science and Technology, Norwegian University of Life Sciences, Ås, Norway

(\*Electronic mail: marija.vukovic@nmbu.no)

Outdoor photoluminescence imaging on field-deployed solar cell modules has been conducted to an increasing extent in the recent years. Photoluminescence images provide more details about defects than thermal infrared images, while the imaging procedure has the potential to be faster than electroluminescence imaging because it does not require electrical connection to the modules. However, when conducted with sunlight excitation, it is based on lock-in technique which implies switching between the modules' two operating points. This often results in the need to connect additional electrical equipment dimensioned for the task and leads to production disruption for the investigated modules. The present study demonstrates image acquisition based on the string inverter's ability to sweep the IV curve. The advantage of this approach is two-fold. This is a non-invasive method which only requires imaging apparatus and therefore allows for a flexible imaging procedure on string, module or cell level without having to take into account additional equipment. Furthermore, photoluminescence images spanning the whole IV curve can be obtained during one sweep, as opposed to obtaining images in two operating points when using lock-in technique. Such image series can be used to investigate the state of the cells and modules by looking at the photoluminescence images acquired on different current extraction levels. This has been done for a healthy string and a broken module.

Images of photoluminescence (PL) emitted from silicon photovoltaic (PV) cells and modules can be acquired due to the radiative band-to-band recombination of charge carriers over the bandgap at 1150 nm<sup>1</sup>. This signal can reveal different parameters affecting solar cell performance and is a valuable tool for the PV industry<sup>1</sup>. PL images of modules collected outdoor have been studied to an increasing extent in the last years<sup>2-8</sup> and they can reveal a variety of faults that might affect their performance such as cracks<sup>3,4,6</sup>, potential induced degradation<sup>5</sup>, "snail trails"<sup>5</sup>, EVA degradation<sup>5</sup>, bypass diode failures<sup>4,5</sup> and regions affected by series resistance losses<sup>2-5,8</sup>. The advantage of outdoor PL imaging is that the procedure can potentially be notably faster than electroluminescence (EL) imaging because connecting electrically to a PV system is no prerequisite as it is for EL imaging. Additionally, PL images, similar to EL images, provide more information than thermal infrared images<sup>9</sup>.

When PL imaging is conducted with sunlight excitation, the weak radiative band-to-band signal is not obtainable due to the reflected sunlight recorded by the camera, unless the image acquisition is carried through together with the modulation of the PV system's operating point<sup>2-4,6-8</sup>. Approaches developed so far are mostly dependent on the equipment dimensioned for imaging a certain number of modules<sup>2,4,7,10</sup>. In that way PL imaging ceases to be a contactless imaging method, it causes interference with the production process and it makes it harder to make spontaneous decisions in the field.

We demonstrate a non-invasive method for PL imaging of PV modules which takes advantage of an integrated functionality of string inverters, namely the IV curve sweep. No connection with the PV system is necessary. The only equipment is the imaging apparatus allowing for flexibility to image on string, module or cell level. The validity of a PL image obtained in this way is discussed compared to an EL image. Advantages of a data set spanning the whole IV curve are demonstrated.

The PL signal intensity is dependent on the level of current

extraction during the IV curve sweep. The extracted current density  $J$  of an area  $A$  of a solar cell which behaves as an ideal diode is given by

$$J = J_{SC} - J_0 \exp \frac{V_{d,A}}{V_T} \quad (1)$$

where  $J_{SC}$  is the short circuit (SC) current density and  $J_0$  is the total dark current density<sup>11,12</sup>. The PL signal of the area  $A$  is given by

$$PL_A = C \exp \frac{V_{d,A}}{V_T} + PL_{offset,A} \quad (2)$$

where  $C$  is a calibration constant accounting for the carrier lifetime of the cell, the optical characteristics and geometry,  $V_{d,A}$  is the diode voltage of the same area,  $V_T$  is the thermal voltage and  $PL_{offset,A}$  is the PL signal caused by diffusion-limited carriers<sup>12,13</sup>. Solving Eq. 2 for  $V_{d,A}$  and substituting in Eq. 1 results in

$$J = J_{SC} - \frac{J_0}{C} (PL_A - PL_{offset,A}). \quad (3)$$

The levels of current extraction and the PL signal intensities in two different operating points are given by

$$J_1 = J_{SC1} - \frac{J_{01}}{C_1} (PL_{A1} - PL_{offset1,A}) \quad (4)$$

and

$$J_2 = J_{SC2} - \frac{J_{02}}{C_2} (PL_{A2} - PL_{offset2,A}). \quad (5)$$

Since the calibration constant  $C$  can be determined from an image in the open circuit condition and the open circuit voltage<sup>11,12</sup>,  $C_1 = C_2 = C$ . The illumination conditions are considered unchanged during the acquisition of two images and therefore  $J_{SC1} = J_{SC2} = J_{SC}$ . The dark current density is assumed  $J_{01} = J_{02} = J_0$ . Since  $PL_{offset,A}$  is obtained with

an image in SC condition<sup>11,12</sup>,  $PL_{offset1,A} = PL_{offset2,A} = PL_{offset,A}$ . Subtracting Eq. 5 from Eq. 4 and solving for the difference in PL signal intensity results in

$$PL_{A2} - PL_{A1} = \frac{C}{J_0}(J_1 - J_2). \quad (6)$$

This relationship shows that the difference in the PL signal intensity between two operating conditions,  $\Delta PL = PL_2 - PL_1$ , is linearly proportional to the difference in the extracted current density. The intensity of the PL signal in condition 2,  $PL_2$ , is higher than in condition 1,  $PL_1$ , at the same time as the current density  $J_2$  is lower than  $J_1$ . In the following, the average PL signal intensity of an area is analysed as a function of its extracted current.

Images were acquired in this study during measurement of a part of the IV curve performed by the string inverter Fronius Primo 3.0<sup>14</sup> connected to three bifacial PERC modules (JA Solar JAM72D20) in series as shown in Fig. 1. This built-in functionality is a part of the string inverter's intelligent shade management with the aim of searching for the global maximum power point (MPP) and is realized by sweeping the IV curve every 10 minutes. The camera was positioned in front of the modules connected to the inverter and 200 000 images were collected during approximately 20 minutes. In that period two IV curve sweeps took place.

The imaging was conducted with a short-wave infrared camera of type Raptor Photonics Owl 640S with an InGaAs detector, optical range 900 nm – 1700 nm and 640x512 resolution. An optical band-pass filter by Edmund Optics with the wavelength range 1100-1150 nm and optical density  $\geq 4.0$  is used in order to filter out the reflection detected outside the range of the emitted PL signal. Integration time of 0.3 ms and frame rate of 167 Hz (acquisition time of 6 ms) allowed for approximately 330 images to be collected during one sweep.

In order to illustrate the IV curve sweep in this study, current had to be recorded. This was done at the same time as the images were collected using a triggering and acquisition box, as illustrated in Fig. 1. The box triggered the camera and

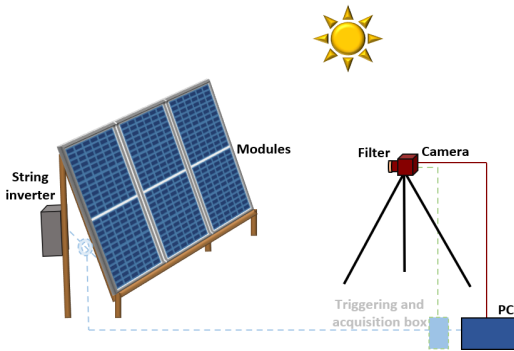


FIG. 1. Experimental setup for PL imaging and current measurements for the PV string consisting of three bifacial modules.

recorded the current. This part of the equipment, illustrated with light color and dashed lines, is otherwise not necessary because the increase in the PL signal intensity, i.e. the pixel values, is a sign of the IV curve sweep taking place.

One IV curve sweep during which the images were acquired is displayed in Fig. 2. Fig. 2(a) shows the string current at the MPP at approximately 11 A when the sudden drop below 5 A is measured at 12 h 23 minutes. The current drop is enlarged in Fig. 2(b) with the values on the x-axis sampled in milliseconds. It shows that it takes approximately 2 seconds

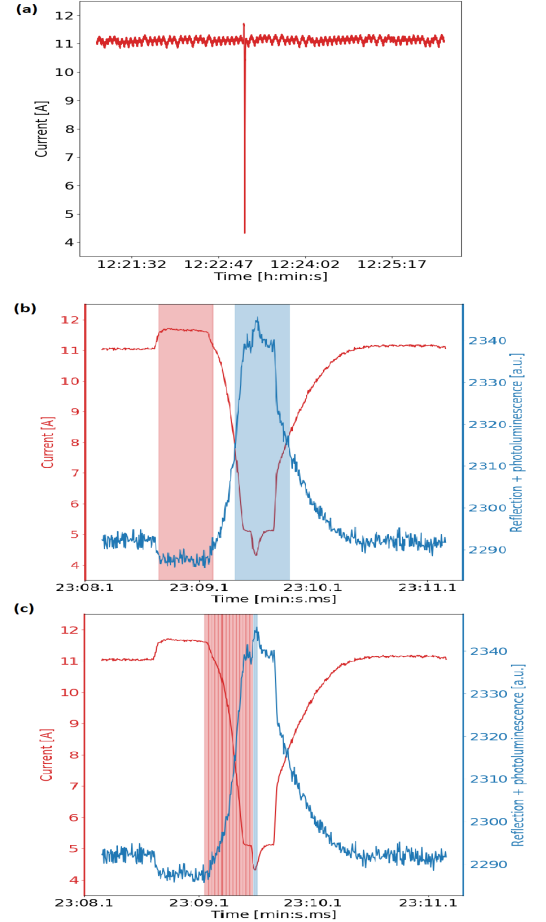


FIG. 2. Current displayed as a function of time showing a brief fall at 12h 23 minutes (a). Time sequence between 12h 23min 08sec and 12h 23min 11sec shows the shape of the current fall and the increasing signal from the modules. The blue and red areas mark the selected images resulting in a  $\Delta PL$  image (b). The same enlarged time sequence with red and blue regions mark the images chosen to test the result in Eq. 6 (c).

for the inverter to sweep the IV curve. The current data is overlaid with the average pixel count per image as a function of time, which is the sum of reflection from the modules and the PL signal. The increase in the total signal detected is due to the increase in the PL signal at the time of the current fall.

The blue and red areas in Fig. 2(b) mark the images selected for the calculation of one difference PL image,  $\Delta PL$ . They are chosen so that they might give a  $\Delta PL$  image with the highest difference in PL signal. The two areas are selected based on where the PL signal is at its strongest (top of the blue curve) and at its weakest (dip in the blue curve). The calculation was performed by averaging and subtracting 80 images in the red region from 80 images in the blue region. The obtained  $\Delta PL$  image is compared with the EL images of the modules acquired in the dark with SC current,  $EL_{SC}$ .

In order to further investigate the quality and possibilities of this data set, the result in Eq. 6 is tested for the images marked in blue and red in Fig. 2(c). These areas are defined in order to produce not one, but a sequence of  $\Delta PL$  images. Averaging over the images in the blue region results in a  $PL_2$  image (Eq. 6) with the lowest current for five images. Looping

through the red area by choosing five new images with every step results in 14  $PL_1$  images. The interval size of five images was chosen as a trade-off between improving the quality of  $\Delta PL$  images through averaging and obtaining a data set with more points. The red region starts at the SC condition and is defined so that it does not comprise redundant data i.e. images taken in the same operating condition. For every  $\Delta PL$  image obtained, the difference in extracted current is calculated.

The  $\Delta PL$  image of the string obtained as described in Fig. 2(b), is shown in Fig. 3(a). Three separate  $EL_{SC}$  images are shown in Fig. 3(b). The pixel values differ on the two scales since they represent the intensity of different signals. The EL images show three modules which appear to be in a good state. The  $\Delta PL$  image is in accordance with this observation. A few areas which display lower intensity values in the EL images are marked with blue squares in (a) and (b). They appear to be areas with dark color i.e. increased series resistance, which are visible to a smaller or greater extent in the  $\Delta PL$  image.

The color distribution on the  $\Delta PL$  image in (a) and  $EL_{SC}$  images in (b) differs in such a way that the  $\Delta PL$  values in the upper halves of the two modules on the sides seem to be higher than in the lower halves of the same modules. The upper halves are elevated from the ground and for the bifacial modules this leads to increased gain<sup>15</sup>, which might be the case here. Why this is not so clearly visible for the upper part of the middle module could be because it is in the middle and less diffuse light reached it at the back in the moment of imaging.

The data points obtained based on Eq. 6 and Fig. 2(c),  $PL_2 - PL_1$  as a function of difference in current, are plotted in Fig. 4. They are fitted with a linear model with the coefficient of determination  $R^2=0.9987$  having the intercept point of -0.016. The intercept point very close to zero is in accordance with Eq. 6. The modules satisfy the assumption about an ideal diode model since they display a linear relationship between the  $\Delta PL$  and difference in current extraction. This confirms the observations in Fig. 3 that the modules are in a good state and not affected by any serious resistance problems. The result in Fig. 4 also shows that the data set collected can be used not only to produce one  $\Delta PL$  image, but several of them with different signal intensities. This makes it possible to assess

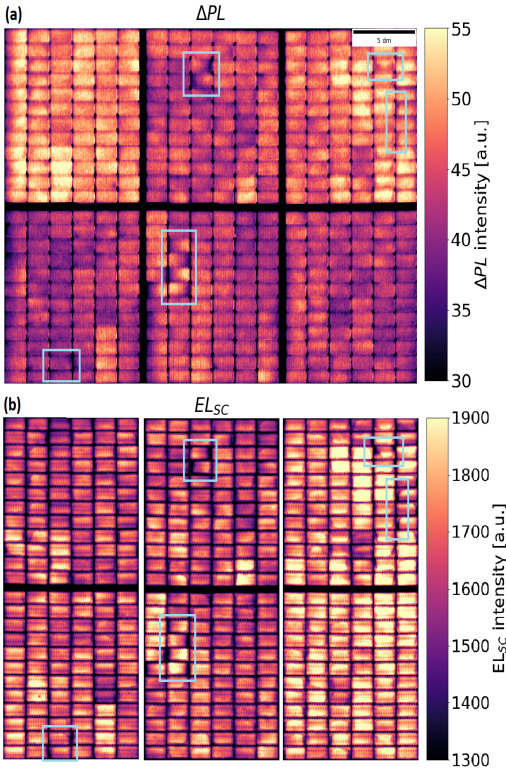


FIG. 3.  $\Delta PL$  image of a string consisting of three bifacial modules connected in series (a) and three  $EL_{SC}$  images of the modules (b).

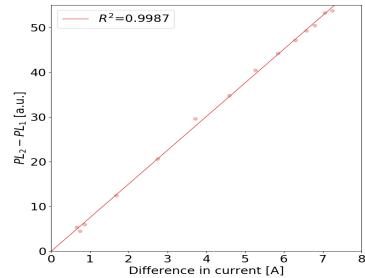


FIG. 4. Linear regression model  $y = 7.54x - 0.067$  fitted to the average pixel count as a function of current difference for 14 images.

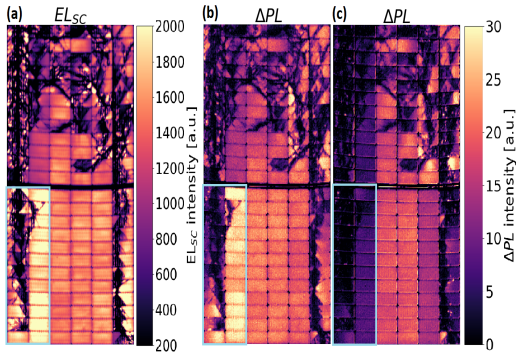


FIG. 5.  $EL_{SC}$  image of a broken bifacial module (a),  $\Delta PL$  image obtained with  $PL_1$  and  $PL_2$  taken with a difference in current extraction of  $5.74A - 3.49A = 2.25A$  (b) and  $\Delta PL$  obtained with the same difference in current extraction  $7.99A - 5.74A = 2.25A$  (c).

modules with defects into greater detail<sup>3,4</sup>.

In order to investigate how useful  $\Delta PL$  images obtained with different levels of current extraction might be, the imaging procedure has been conducted on a broken bifacial module. This is illustrated in Fig. 5. An  $EL_{SC}$  image is shown in Fig. 5(a), while two  $\Delta PL$  images are shown in (b) and (c). The raw images in (b) and (c) were acquired with an average current of  $3.49A/5.74A$  and  $5.74A/7.99A$  respectively, meaning that the difference in current extraction is  $2.25A$  for both images. The  $\Delta PL$  image in (b) is quite similar to the EL image with respect to color distribution, while the image in (c) differs. This is particularly the case for the two lower left columns. The intact cells of this sub-string have high values in (a) and (b). However, the same two columns behave differently in (c) and have considerably lower values compared to the rest of the module.

Given the irradiation level at the time of imaging, the MPP current for this module was at  $7.32A$ . This means that the  $\Delta PL$  image in (b) was obtained with images taken when the current was in the lower part of the IV curve, while the image in (c) was obtained with one current level above and one below the MPP. Very low  $\Delta PL$  values in (c) for the lower left sub-string might mean that the current levels above the MPP cannot be extracted equally well as currents below the MPP. Further analysis of the state of this module is needed. This particular case shows how different  $\Delta PL$  images might give diverging information. The advantage of conducting image acquisition with the IV curve sweep is that a whole range of  $\Delta PL$  images is obtained without having to invest any additional effort in acquiring them.

Photoluminescence images of PV modules collected outdoor with sunlight excitation can provide useful information about the field-deployed modules. Removing the need for additional equipment and disturbance in power production contributes to a more efficient imaging. The present study demonstrates a method which takes advantage of already

existing PV system equipment in the field. A series of images can be collected during the string inverter's IV curve measurement and result in a whole range of PL images. They can be a useful tool to analyse the nature of the defects that the modules might be affected by. This method allows for diagnostic imaging with a high throughput on the string level before a more targeted imaging is conducted on module or cell level.

This work was performed within The Norwegian Research Center for Sustainable Solar Cell Technology (FME SUSOLTECH, project number 257639/E20). The center is co sponsored by the Research Council of Norway and its research and industry partners.

Data available on request from the authors.

- <sup>1</sup>E. Olsen and A. Flå, "Spectral and spatially resolved imaging of photoluminescence in multicrystalline silicon wafers," *Applied Physics Letters* **99**, 011903–1–011903–3 (2011).
- <sup>2</sup>L. Stoicescu, M. Reuter, and J. Werner, "Days:luminescence imaging of pv modules in daylight," 29th European Photovoltaic Solar Energy Conference and Exhibition, 2553–2554 (2014).
- <sup>3</sup>T. Silverman, M. Deceglie, K. VanSant, S. Johnston, and I. Repins, "Illuminated outdoor luminescence imaging of photovoltaic modules," *IEEE 44th Photovoltaic Specialist Conference*, 3452–3455 (2017).
- <sup>4</sup>R. Bhoopathy, O. Kunz, M. Juhl, T. Trupke, and Z. Hameiri, "Outdoor photoluminescence imaging of solar panels by contactless switching: Technical considerations and applications," *Prog Photovolt Res Appl*, 1–12 (2019).
- <sup>5</sup>B. Doll, J. Hepp, M. Hoffmann, R. SchÄ¼ler, C. Buerhop-Lutz, I. Peters, J. Hauch, A. Maier, and C. Brabec, "Photoluminescence for defect detection on full-sized photovoltaic modules," *IEEE Journal of Photovoltaics*, 1–11 (2021).
- <sup>6</sup>L. KÄ¼ster, A. Astigarraga, S. Lindig, A. Louwen, M. Antinori, D. Moser, and G. Manzolini, "Quality assurance of the photovoltaic power plants installation stage - a complementary strategy based of photoluminescence and steady-state thermography," 38th European Photovoltaic Solar Energy Conference and Exhibition, 1042–1050 (2021).
- <sup>7</sup>O. Kunz, G. Rey, M. Juhl, and T. Trupke, "High throughput outdoor photoluminescence imaging via pv string modulation," 48th IEEE Photovoltaic Specialists Conference, 346–350 (2021).
- <sup>8</sup>M. Vuković, I. HÄ¼jaas, M. Jakovljević, A. Flå, E. Olsen, and I. Burud, "Photoluminescence imaging of silicon modules in a string," *Prog Photovolt Res Appl*, 436–446 (2022).
- <sup>9</sup>W. Herrmann, G. Eder, B. Farnung, G. Friesen, M. KÄ¼ntges, B. Kubicek, O. Kunz, H. Liu, D. Parlevliet, I. Tsanakas, and J. Vedde, "Qualification of photovoltaic (pv) power plants using mobile test equipment," *Photovoltaic Power System Programme 13* (International Energy Agency, 2021).
- <sup>10</sup>M. Guada, MoreÄ¼n, S. RodrÄ¼guez-Conda, L. SÄ¼nchez, M. MartÄ¼nez, M. GonzÄ¼lez, J. JimÄ¼nez, L. PÄ¼rez, V. Parra, and O. MartÄ¼nez, "Daylight luminescence system for silicon solar panels based on a bias switching method," *Energy Science and Engineering*, 1–15 (2020).
- <sup>11</sup>T. Trupke, M. Abbott, and E. Pink, "Spatially resolved series resistance of silicon solar cells obtained from luminescence imaging," *Applied Physics Letters* **90**, 093506–1–093506–3 (2007).
- <sup>12</sup>Y. Augarten, T. Trupke, M. Lenio, J. Bauer, O. Breitenstein, J. Weber, and R. Bardos, "Luminescence shunt imaging: Qualitative and quantitative shunt images using photoluminescence imaging," 24th European Photovoltaic Solar Energy Conference, 27–31 (2009).
- <sup>13</sup>C. Shen, *Power loss analysis via photoluminescence*, PhD dissertation, UNSW (2014).
- <sup>14</sup>F. S. Energy, "Dynamic peak manager: profitable pv systems despite shading," (2022), last accessed 17 April 2022.
- <sup>15</sup>X. Sun, M. Khan, C. Deline, and M. Alam, "Optimization and performance of bifacial solar modules: A global perspective," *Applied Energy* **212**, 1601–1610 (2018).

# Appendix D

## Paper D



# Extraction of photoluminescence with Pearson correlation coefficient from images of field-installed photovoltaic modules

M. Vuković, K. H. Liland, U. G. Indahl, M. Jakovljević, A. S. Flø, E. Olsen, I. Burud<sup>1</sup>  
*Faculty of Science and Technology, Norwegian University of Life Sciences, Ås, Norway*

(\*Electronic mail: marija.vukovic@nmbu.no)

Photoluminescence imaging of field-installed photovoltaic modules has the potential to be a high through-put on-site inspection technique. A contribution to this development is a noninvasive photoluminescence imaging method proposed recently. It is based on acquiring images during a progressing current-voltage curve sweep, resulting in a detection of a continuously changing photoluminescence signal. From this follows the necessity to employ an alternative algorithm based on the Pearson correlation coefficient, which will contribute to an efficient, unsupervised image processing and thus easier (in real-time) implementation. The new algorithm separates photoluminescence from the reflected sunlight, similar to the conventional subtraction algorithm. However, it is robust to varying solar irradiance, can process photoluminescence signal emitted from multiple asynchronised strings, and we predict will enable unsupervised real-time surveillance and detection of functional anomalies at low computational cost. It is also more sensitive at segmenting ground-reflected photoluminescence.

## I. INTRODUCTION

In order to ensure effective operation of photovoltaic (PV) power plants, fast and detailed inspections are necessary<sup>1,2</sup>. They should be based on complimentary techniques for a comprehensive understanding of faults and degradation mechanisms in PV modules. Luminescence imaging is an important technique in this context due to the level of information and accuracy which is obtainable from the images<sup>2</sup>. Compared to electroluminescence imaging (EL), photoluminescence (PL) imaging has the potential to be considerably faster because excitation of charge carriers is based on illumination and it therefore does not require wiring of an external power source to the PV system<sup>3</sup>.

In a recent study we showed how PL imaging in daylight can be conducted with a noninvasive procedure on string level<sup>4</sup>. This method does not require any connection to the PV system for the purpose of explicit control of its operating point (OP), as is the case with the lock-in technique<sup>5-11</sup>, and can instead be carried through during string inverter's built-current-voltage (IV) curve sweep procedures.

Compared to maximum power point tracking (MPPT), which determines the maximum power point (MPP) based on continuous measurement of the output current and voltage within the preset voltage range, an IV curve scan can be extended to cover almost the entire scope of the IV characteristics<sup>12-15</sup>. The MPPT algorithm does not guarantee the detection of the global MPP in case of partial shading when there are different local MPPs<sup>16</sup>. But the global maximum can be located by sweeping the IV curve<sup>13,14</sup>.

The implementation of IV curve sweeps by different companies is a subject of their proprietary solutions<sup>16</sup>. The sweeps can be conducted on plant, array or string level depending on the inverter. They can be initiated by the string inverter itself or by an operator, depending on the producers implementation of the IV curve sweep functionality<sup>12,14,17,18</sup>. Their duration is not specified in manuals and technical papers. In case of Fronius Primo 3.0 string inverter, IV curve sweeps, as a part of Fronius' intelligent shade management system<sup>13</sup>, have been measured to around 2-s taking place on a regular basis (ev-

ery 10 minutes)<sup>4</sup>. Huawei and Sungrow offer IV curve scans, logging and reporting for monitoring purposes<sup>12,18</sup>. Danfoss string inverters offer standard sweep on plant or string level at the defined time intervals, as well as forced sweeps<sup>14</sup>.

An advantage with PL imaging during IV curve sweeps is that it can be conducted with a higher through-put. Furthermore, it results in an image set, which, instead of only two discrete OP, covers the range of the scanned IV curve and therefore a continuously changing PL signal. In that way, images obtained at different levels of current extraction can be analysed<sup>4,7</sup>.

PL images have so far been processed with a subtraction algorithm<sup>4-11</sup>. It is based on subtracting images with lower PL signal, obtained while the PV system is in an OP with high current extraction, from the images with higher PL signal, obtained while the PV system is in an OP with low or no current extraction. The reflected sunlight is eliminated, under the assumption of constant irradiance, and the difference PL signal,  $\Delta PL$ , extracted.

If the images are acquired during switching between two predetermined OP, then they fall into two groups of images with two distinct PL intensity levels and their processing with the subtraction approach does not require any additional decision-making. Imaging during IV curve sweeps, however, does not result in images with clearly distinct PL intensity levels and, consequently, they need to be divided into two groups at a later stage. They contain a continuously changing PL signal, and different  $\Delta PL$  images extracted from such data set might result in different information about the damage of a module<sup>4</sup>. Image processing with the subtraction algorithm requires a division into sub-sets based on conscious decision-making and input of knowledge (a supervised approach) or a search for all possible  $\Delta PL$  images without using any prior knowledge about the data set (unsupervised, exhaustive approach). This is computationally demanding and impairs the potential of PL imaging during IV curve sweeps.

In the present study, we propose the application of the Pearson correlation coefficient (PCC) as a more suitable algorithm for image processing of data sets containing continuously changing PL signal. This work is organized as follows.

In the Methodology we describe the PL signal and detection setup, as well as the  $\Delta PL$  image procedure, before introducing our novel Pearson correlation coefficient approach. In the Results we compare the two approaches on various panels in order to show the improved sensitivity of the correlation approach. Finally, we demonstrate how the procedure can be applied in a real-time image processing setting.

## II. METHODOLOGY

### A. PL signal emission and detection

The strength of the radiative band-to-band recombination is proportional to the exponential of the voltage and inversely proportional to the extracted current density from the solar cell<sup>19</sup>. Emitted from within the silicon semiconductor material at around 1150 nm, the PL emission can be detected with a short-wave infrared, such as the camera Raptor Photonics Owl 640S with an InGaAs detector and a resolution  $640 \times 512$ . Its optical range is 900 nm - 1700 nm. An optical bandpass filter with the central wavelength at 1150 nm by Edmund Optics and an optical density of  $\geq 4.0$  is used in order to filter out the reflected sunlight detected outside the range 1125-1175 nm.

Three image series have been acquired of modules of different cell technology: bifacial monocrystalline silicon (mono c-Si) passivated emitter and rear cell (PERC) modules as well as mono c-Si and multicrystalline silicon (multi c-Si) aluminium back surface field (Al-BSF) modules. They are listed in Table I with respect to the cell technology, module type, producer, number of imaged modules, module's condition, nominal power, open-circuit ( $V_{OC}$ ) voltage, short-circuit ( $I_{SC}$ ) current and the notation for the image series. The modules imaged in PERC3 series are connected to a Fronius Primo 3.0 string inverter. The module imaged in PERC1 series is connected to a separate string inverter of the same type together with four Al-BSF modules imaged in BSF6 series. Two multi c-Si modules from BSF6 series are not connected to the two imaged strings.

The image acquisition procedure is illustrated in Fig. 1. Each image series listed in Table I was obtained during one IV curve scan initiated by the Fronius Primo 3.0 string inverter from the  $I_{SC}$  condition to a current level close to the  $V_{OC}$  condition in duration of approximately  $2 \cdot s^4$ . Current measurements were collected simultaneously with the same sampling frequency as images (150 Hz).

### B. PL signal identification

#### 1. Difference PL image

The approach used so far for separation of the PL signal from the reflected sunlight has been the  $\Delta PL$  algorithm<sup>5-7,9,11,20</sup>. Two images of a PV module are acquired in two different operating conditions, i.e., under different operating voltages. They contain the emitted PL signal and the

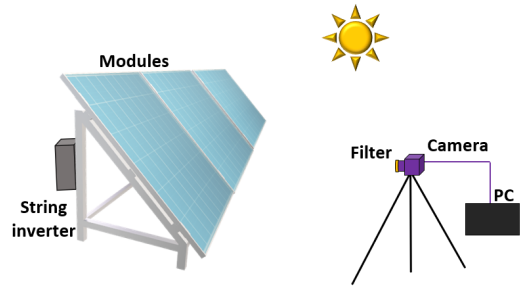


FIG. 1. PL imaging in daylight is based on detection of the PL signal with a short-wave infrared camera during an IV curve sweep initiated by the string inverter.

reflected solar irradiance  $R$ . Due to PL emission's voltage dependency, PL signal has different intensities in the two conditions,  $PL_1$  and  $PL_2$ . The total signal detected in both images can therefore be written as  $PL_1 + R_1$  and  $PL_2 + R_2$ . Switching between two OP fast enough gives grounds to assume constant irradiance during acquisition of both images. Therefore, one can assume that  $R_1 = R_2 = R$  and eliminate the detected reflected solar irradiance by obtaining a difference PL image,  $PL_1 + R - (PL_2 + R) = \Delta PL$ . However, using only one image pair and obtaining one  $\Delta PL$  image results in a low signal-to-noise ratio<sup>7,9</sup>. A method for signal enhancement has been to acquire a series of images  $PL_{11} + R_{11}, PL_{12} + R_{12}, \dots, PL_{1i} + R_{1i}$  and  $PL_{21} + R_{21}, PL_{22} + R_{22}, \dots, PL_{2i} + R_{2i}$ , where  $i = 1, 2, \dots, N$  images in each operating condition, and to average over them in order to obtain two images,  $PL_{1avg} + R_{1avg}$  and  $PL_{2avg} + R_{2avg}$ <sup>5-7,9,11</sup>.

As opposed to collecting images in two discrete operating conditions, using the IV curve sweep approach results in a series of images  $PL_1 + R_1, PL_2 + R_2, \dots, PL_j + R_j$ , where  $j = 1, 2, \dots, M$  images collected over a wide range of operating conditions<sup>4</sup>. This means that it is possible to define the size  $N$  of any two image sub-sets after image acquisition in order to obtain  $PL_{1avg} + R_{1avg}$  and  $PL_{2avg} + R_{2avg}$ . The result can be several  $\Delta PL$  images, which give a more thorough investigation into how a module operates in different conditions<sup>4</sup>.

However, with a frame rate of 150 Hz, an IV curve scan can be covered with a few hundreds of images. An image sub-set can consist of only 20 images, as will be demonstrated in the present study, and it can serve as either  $PL_{1avg} + R_{1avg}$  or  $PL_{2avg} + R_{2avg}$  image. Therefore, a vast number of  $\Delta PL$  images can be obtained. Having an image series, in which the PL signal changes over time, gives a possibility for an alternative and more efficient approach, which is based on the PCC algorithm.



TABLE I. An overview of the imaged modules and their specifications.

Cell technology	Module type	Producer	Nr. of modules	Nr. of cells	Module's condition	Nominal power	$V_{OC}$	$I_{SC}$	Image series
PERC	JAM72D20	JA Solar	3	144 half-cells	Undamaged	460 W	49.91 V (0.693 V/cell)	11.5 A	PERC3
			1		Damaged				PERC1
AI-BSF (mono c-Si)	ZKX-260D-24	CETC Solar Energy	2	60 cells	Slightly damaged	260 W	38.23 V (0.637 V/cell)	8.67 A	BSF6
AI-BSF (multi c-Si)	Inceptio 250F	SweModule	4	60 cells	Unknown	250 W	37.7 V (0.628 V/cell)	8.80 A	BSF6

## 2. Pearson correlation coefficient image

The following expression for PCC,  $\rho$ , can be applied to a set of PL images

$$\rho = \frac{\sum_{i=1}^N (X_i - \bar{X})(Y_i - \bar{Y})}{\sqrt{\sum_{i=1}^N (X_i - \bar{X})^2} \sqrt{\sum_{i=1}^N (Y_i - \bar{Y})^2}} \quad (1)$$

where  $X$  is the detected signal over time in every pixel and  $Y$  is the mean image pixel count,  $\bar{X}$  and  $\bar{Y}$  are their mean values and  $N$  is the number of temporal measurements, i.e., number of aligned images<sup>21,22</sup>. The PCC represents a measure of linear similarity between two variables<sup>22</sup> and can have values in the interval  $-1 \leq \rho \leq 1$ <sup>21</sup>. A PCC image, here referred to as  $PCC_{PL}$ , is given by the associated array of correlation coefficients obtained for all pixel positions of the  $N$  images.

The PCC algorithm makes it possible to separate the PL signal from reflected solar irradiance based on the unique change in its emission during an image acquisition procedure. The pixels depicting the grass or the sky contain only information about the reflected sunlight. This distinction is illustrated in Fig. 2(a) with the temporal change in the signal from one background pixel,  $X_1$ , and one module pixel,  $X_2$ , detected during an IV curve sweep. Correlating the temporal measurements of pixel positions  $X_1$  and  $X_2$  and a corresponding reference signal  $Y$ , showing a similar development of the PL signal as the module pixels, results in a low and a high correlation value,  $\rho_1$  and  $\rho_2$ , as shown in Fig. 2(b)-(c). This difference in correlation values can be exploited for PL extraction from reflected solar irradiance. As there is no library signal<sup>23</sup>, which can be used as reference signal  $Y$  in the present study, it can be defined from the measurement data as the mean image pixel count. This approach is applicable to PL image series in which the PL signal changes in a distinct way compared to the background signal, independently of whether it is acquired during an IV curve sweep.

Even though the mean image pixel count is an average of more than 300k pixels, it can still be noisy due to atmospheric and instrumental noise. One option for smoothing, popular for its ability to retain signal shape, is the Savitzky-Golay (SG) filter. SG smooths time-series or spectral data by a sliding window approach where a polynomial of chosen degree and window is locally fitted at every position along the time-series

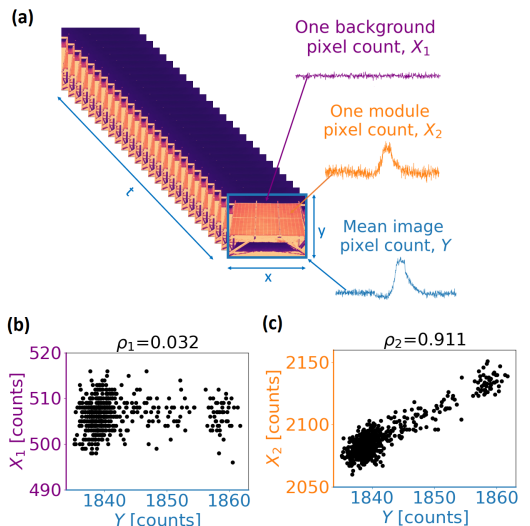


FIG. 2. An image set obtained during an IV curve scan contains information along two spatial dimensions,  $x$  and  $y$ , and one temporal dimension,  $t$ . Values of one background pixel over time,  $X_1$ , is shown in purple, the signal from one module pixel over time,  $X_2$ , is shown in orange and the average image pixel count,  $Y$ , is displayed in blue (a). Variables  $X_1$  and  $X_2$  plotted as a function of  $Y$  (b)-(c) show no correlation,  $\rho_1$ , and strong correlation,  $\rho_2$ .

and each original value is replaced by the middle point of the fitted polynomial. In the following, we fixed the polynomial at degree three and tested windows widths 5, 15, 25, 35 and 45 (increasing smoothness)<sup>17,24,25</sup>.

## III. RESULTS AND DISCUSSION

One raw image from image series *PERC3*, *PERC1* and *BSF6* is shown in Fig. 3(a)-(c). Average image pixel counts across all images in addition to current measurements are displayed on the left and right y-axis in Fig. 3(d)-(f). The peak

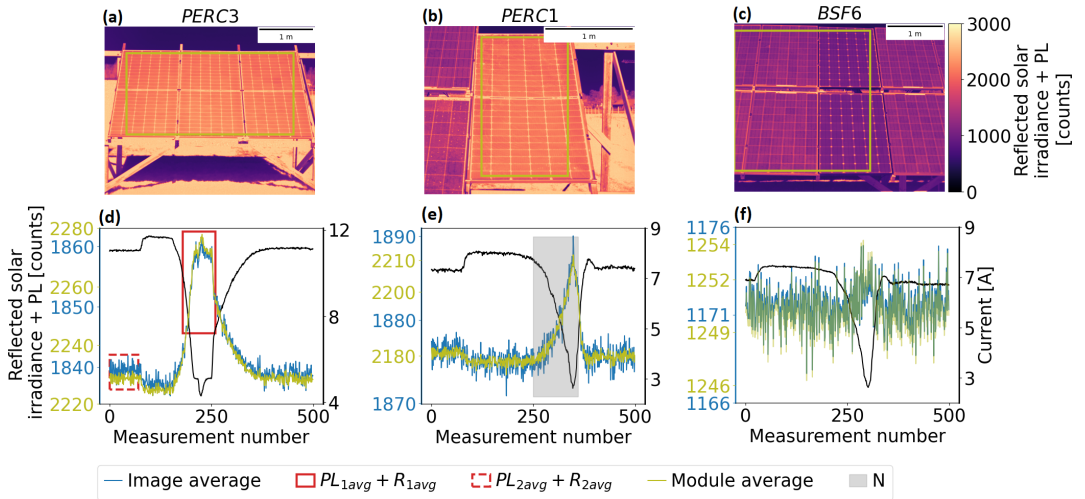


FIG. 3. A raw image from the *PERC3* (a), *PERC1* (b) and *BSF6* images series (c) with the corresponding current measurements and average image and module pixel count (d)-(f).

of the average image pixel count is most pronounced in Fig. 3(d). That is to be expected because the *PERC3* modules have a higher  $V_{OC}$  than the *BSF6* modules and they are not damaged as the module in the *PERC1* data series. The PL signal is difficult to detect from the average image pixel count in the *BSF6* data series in Fig. 3(f), despite the fact that the current difference was around 4 A during the IV curve sweep, the same as in Fig. 3(e). This can be ascribed to the BSF technology and a lower  $V_{OC}$  voltage<sup>11</sup>.

The mean image pixel count is compared with the mean module pixel count in Fig. 3(d)-(f), obtained from the pixels within the yellow square in Fig. 3(a)-(c). This makes it possible to visualize whether the background pixels of grass, sky or other surfaces distort the original PL signal. The absolute values are lower for the average image pixel count compared to the average module pixel count in all three cases. However, the shape of the PL signals based on the mean image pixel count is not distorted and it can therefore be used as the reference signal  $Y$ . This is an advantageous approach for real-time data analysis in field campaigns, because not having to segment the module pixels in order to obtain the reference signal results in a more efficient and low-cost image processing. It raises, however, the question of which percentage of an image should depict PV modules as opposed to surroundings in order for the PL peak to be recognisable in the reference signal. This should be investigated at a later stage.

Figure 3(d)-(e) also illustrate how  $\Delta PL$  and  $PCC_{PL}$  images can be obtained from the three image sets. For the  $\Delta PL$  analysis, as mentioned above, two sub-sets of images need to be selected and averaged into a  $PL_{1avg} + R_{1avg}$  and a  $PL_{2avg} + R_{2avg}$  image. Randomly placed squares with full and dashed lines in Fig. 3(d) illustrate one possibility for this selection. For

the  $PCC_{PL}$  analysis, the  $N$  number of images needs to be determined, as given by Eq. 1 and illustrated in Fig. 3(e). The PCC approach is more favorable in this regard because its implementation requires only one image sub-set. This aspect will be discussed in depth in the subsequent sections.

## A. Correspondence between the $\Delta PL$ and $PCC_{PL}$ images

### 1. Background pixels vs. module pixels

It is important to emphasize that the absolute  $\Delta PL$  and  $PCC_{PL}$  values are not comparable and cannot be translated to each other. It is the distribution of values across an image that is comparable between the two types of images.

Correspondence between the two algorithms with respect to the background and module pixels is investigated based on data series *PERC3* presented in Fig. 4-Fig. 9. Image sub-sets have been selected manually from the data set for calculation of the  $\Delta PL$  and  $PCC_{PL}$  images. The selection was based on the width of the PL signal. Images  $PL_{1avg} + R_{1avg}$  and  $PL_{2avg} + R_{2avg}$  were obtained by averaging 90 and 100 images around the highest and the lowest regions of the PL signal, while the  $PCC_{PL}$  image was obtained by using  $N=130$ , which is the number of images covering the entire PL peak.

Figure 4(a)-(b) show a  $\Delta PL$  image and a  $PCC_{PL}$  image obtained in this way. In both images the module pixels are segmented from the background pixels. All background pixels in the  $PCC_{PL}$  image have values considerably lower than the module pixels. However, the  $\Delta PL$  image has multiple areas of high intensity pixels around the modules which depict the surroundings. These are caused by the difference in reflected

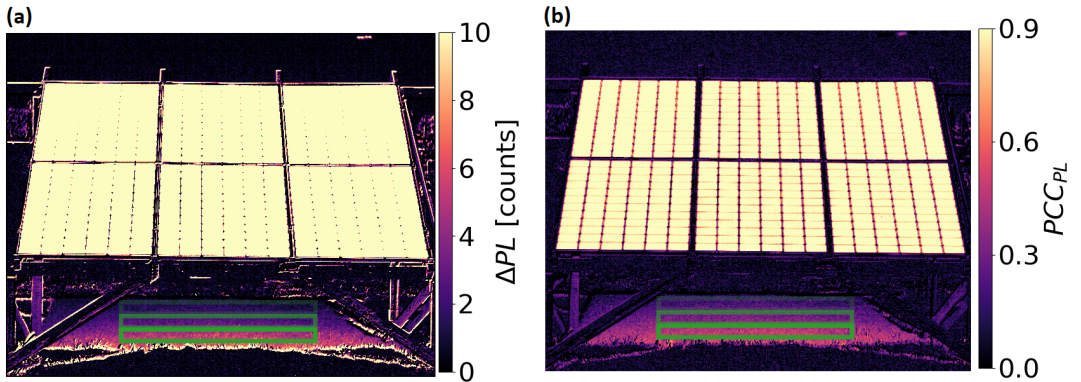


FIG. 4.  $\Delta PL$  (a) and  $PCC_{PL}$  (b) images obtained from *PERC3* data series. The regions marked with the three squares are investigated in Fig. 6.

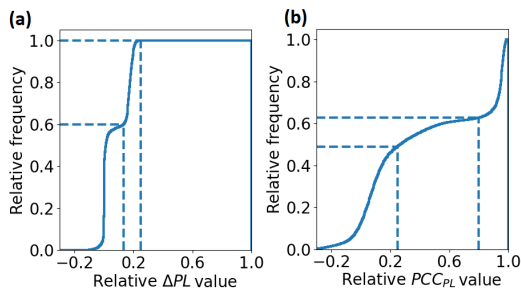


FIG. 5. Cumulative histograms obtained from the normalized  $\Delta PL$  (a) and  $PCC_{PL}$  image (b). They show which fraction of all pixels (y-axis) has values below a certain relative value (x-axis). The stippled lines mark the fractions and relative values of particular interest, i.e., those which describe two groups of pixels, background and modules.

solar irradiance.

For a more detailed look into the overall value distribution in Fig. 4, cumulative histograms of both images are shown in Fig. 5. The pixel values were first normalized relative to the maximum value in each image in order to make the  $\Delta PL$  and  $PCC_{PL}$  value range comparable. The stippled lines give an indication about a difference in the spread of pixel values (contrast) of the two images, which is smaller for the  $\Delta PL$  image compared to the  $PCC_{PL}$  image. Around 60% of the  $\Delta PL$  pixels and 50% of the  $PCC_{PL}$  pixels have values which are smaller than 15% and 25% of the maximum value in each image. But the other 40% of the  $\Delta PL$  pixels have values which are in the narrow range of 15%-25% of the maximum value, while the same percentage of the  $PCC_{PL}$  pixels has values higher than 80% of the maximum value. This means that the PCC algorithm is more sensitive at segmenting the module pixels from the background pixels.

The relative intensity of 100% of the  $\Delta PL$  pixels below 0.25 means that the highest pixel value in that image is more than

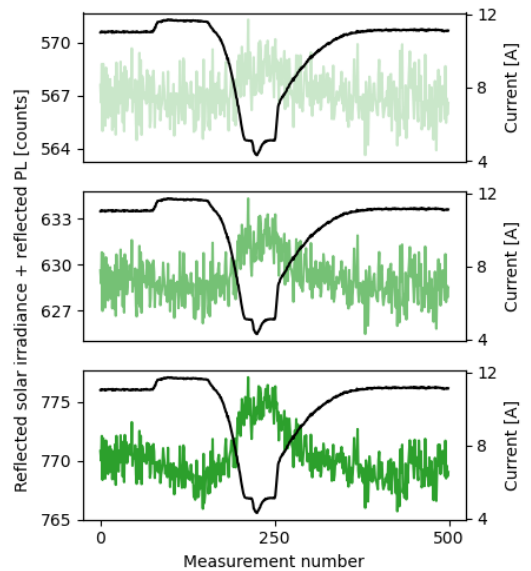


FIG. 6. Signal detected from the ground beneath the modules in data series *PERC3* and extracted from the regions marked with the three green squares in Fig. 4.

four times higher than all the other pixel values. The maximum value in Fig. 4(a) is located in the background region below the modules, where several other pixels have considerably higher values than the module pixels. They should have been eliminated with subtraction, which should have resulted in the module pixels having the highest values. The reason why this is not so is, on the one hand, because the irradiance in reality is not constant, and, on the other hand, because the  $\Delta PL$  algorithm is not robust enough to varying reflected solar

irradiance. The  $PCC_{PL}$  algorithm is more robust in that sense. The maximum value of that image is located on the modules and not in the background. There are no background pixels which have values in the same range as the module pixels.

Considering this robustness of the PCC algorithm, the grass below the modules in the  $PCC_{PL}$  image in Fig. 4(b) has surprisingly high correlation values. These pixels depict the grass in the shadow of the modules, also visible in Fig. 3(a). A look into the average raw values from the three regions within the green squares in Fig. 4(a)-(b) reveals in Fig. 6 that there is a peak originating from the grass shaded with modules. This peak coincides with the current fall. As the grass pixels are far away from the module pixels and their contamination is therefore not probable, the only plausible explanation is that the radiation emitted from the backside of the bifacial modules has been reflected from the grass. The strength of the signal increases as the distance between the ground and the modules decreases, which might be explained by less scattering due to decreasing distance.

This grass region in the  $\Delta PL$  image in Fig. 4(a) shows the same color distribution as in Fig. 4(b). However, since there are multiple background pixel regions with even higher values in the  $\Delta PL$  image, the grass region does not stand out the same way as in the  $PCC_{PL}$  image. The PCC algorithm is more sensitive when it comes to separating ground-reflected photoluminescence from the rest of the background pixels. From the surveillance and monitoring point of view, ground-reflected photoluminescence is an indication that the PL signal emitted from the backside of the bifacial modules has a measurable intensity. This will be investigated in a future study.

In order to investigate correspondence between the two images in Fig. 4 on the module level, it is necessary to adjust their colorbar, as shown in Fig. 7. In that way it becomes visible that the two images correspond well on the cell level, but also that the  $PCC_{PL}$  image has dark, perpendicular lines in most of the cells. Enlarging four cells from Fig. 7 marked with a yellow square shows that these lines are busbars, visible in the  $PCC_{PL}$  image in Fig. 8(b), but not in the  $\Delta PL$  image in Fig. 8(a). Green and black arrows point towards silicon semiconductor columns and busbar columns in Fig. 8(a)-(b) from which raw signal has been extracted for comparison.

The raw signal from the silicon region is shown in Fig. 9(a) and from the busbar region in Fig. 9(b). In both cases they are compared with the mean image pixel count. The raw signal from the cell region coincides very well with the reference signal  $Y$ . The signals from the busbar columns show that the PL peak is detected there as well, which is an indication that the busbar pixels have been contaminated. But those PL peaks are distorted and noisier compared to the mean image pixel count. The distorted PL peak has lower correlation with the reference signal  $Y$  and the busbars therefore appear as dark lines on the solar cells. This distortion of the PL signal is not detectable with the  $\Delta PL$  algorithm because the PL peak is still pronounced enough to result in a  $\Delta PL$  value in the busbars in the same range as the  $\Delta PL$  value in the silicon region.

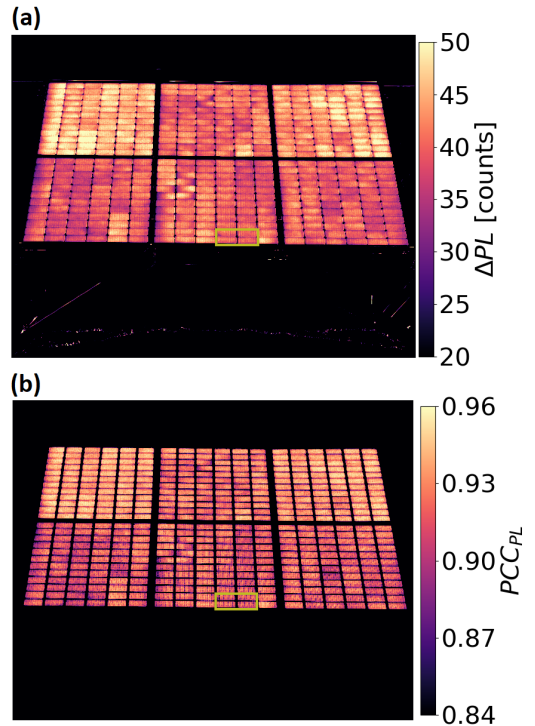


FIG. 7.  $\Delta PL$  (a) and  $PCC_{PL}$  (b) images from Fig. 4 with an adjusted color bar. This makes it possible to compare the two images based on their variation in the module pixels. The yellow square in both images marks a region enlarged in Fig. 8.

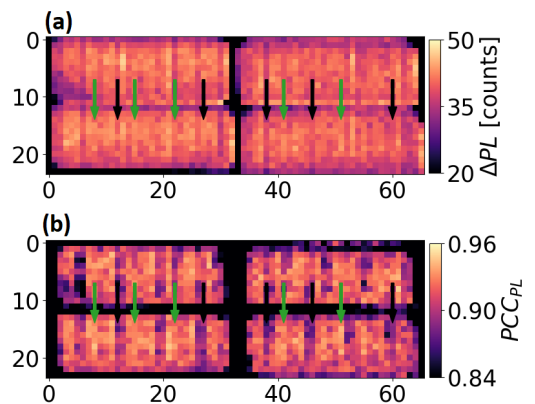


FIG. 8. The region marked with a yellow square in Fig. 7 is enlarged in the  $\Delta PL$  image (a) and  $PCC_{PL}$  image (b). The busbars are visible in the latter, but not in the former. The green arrows point towards the cell columns and black arrows towards the busbar columns from which the signal is investigated in Fig. 9.

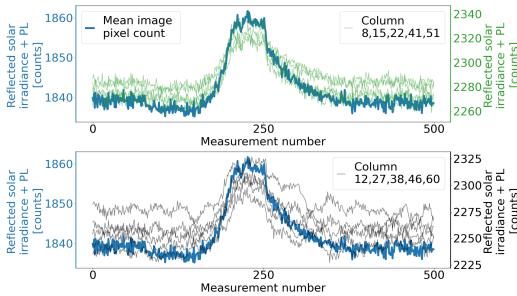


FIG. 9. The raw signal is extracted from the original *PERC3* image series. The green spectra were extracted from the solar cell region (a), while the black spectra were extracted from the busbar region (b) as marked with the green and black arrows in Fig 8(a)-(b), respectively. In both cases, they are compared with the mean image pixel count, reference signal  $Y$ .

## 2. $PCC_{PL}$ images at different levels of current extraction

Two or more  $\Delta PL$  images of a module with series resistance defects obtained during different levels of current extraction might have different  $\Delta PL$  value intensities in the same pixels<sup>4,7</sup>. An investigation is made into how well two  $PCC_{PL}$  images from one data set correspond with two such  $\Delta PL$  images by using the damaged module from *PERC1* series.

Figure 10(a)-(b) illustrate how two  $\Delta PL$  images in Fig. 10(c)-(d) and two corresponding  $PCC_{PL}$  images in Fig. 10(e)-(f), displaying different information about the same module, can be obtained from the same image series. The mean image pixel count from *PERC1* image series is displayed in Fig. 10(a)-(b) with the blue line for images with number 200-350 together with current measurements. The purple line indicates how the signal extracted from the bottom left sub-string of the module changes in these images. The region from which the signal is extracted is marked with the purple square in Fig. 10(c)-(f). Two image sub-sets  $PL_{1avg} + R_{1avg}$  and  $PL_{2avg} + R_{2avg}$  represented with red squares in Fig. (a)-(b) are used in order to obtain the two  $\Delta PL$  images in Fig. 10(c)-(d). The size of each sub-set is 50 images acquired during high level of current extraction, Fig. 10(a), and 20 images acquired during low level of current extraction, Fig. 10(b). Two series of  $N=50$  images indicated with the grey regions in Fig. 10(a)-(b) are used to obtain the two  $PCC_{PL}$  images in Fig. 10(e)-(f) during high and low levels of current extraction, respectively. There is good correspondence between the  $\Delta PL$  images in Fig. 10(c)-(d) and the  $PCC_{PL}$  images in Fig. 10(e)-(f).

The bottom left sub-string in Fig. 10(c) has lower  $\Delta PL$  values compared to the rest of the module. This is due to the almost unchanged PL emission from that part of the module indicated with the purple line in Fig. 10(a) between the image number 200 and 250 as well as in the image range 255-305. The  $PCC_{PL}$  image shows close to zero correlation in Fig. 10(e) for the same reason. Almost no change in the PL signal from the bottom left sub-string in the image range 255-305 in Fig.

10(a) does not correlate well with the reference signal since the blue line shows a slight increase in the PL values.

The bottom left sub-string in Fig. 10(d) has higher  $\Delta PL$  values compared to the rest of the module. This means that the difference in the PL emission is higher between the two chosen OP ranges in Fig. 10(b) in the bottom left part of the module compared to the rest of the module. This is visible based on the steeper increase in the PL signal along the purple line compared to the blue line. The  $PCC_{PL}$  image in Fig. 10(f) conveys the same information in the form of correlation values, showing that the bottom part of the left sub-string correlates well with the average image pixel count. This is due to the similar way in which the blue and purple lines increase in the grey region of Fig. 10(b), when the current is below the MPP.

## B. Unsupervised image processing

It was shown in the last section that the  $PCC_{PL}$  images correspond very well with the  $\Delta PL$  images. However, the question which poses itself is why the PCC algorithm is more favorable for PL image processing. An advantage demonstrated above has to do with the PCC algorithm's ability to separate the pixels of interest from the background pixels, i.e. the pixels in which the PL signal has been detected from those which contain only information about varying irradiance. Other advantages with respect to image processing will be elaborated here. One of them has to do with the amount of generated data during image processing, while the other is related to real-time image processing.

Image processing of PL images acquired with IV curve sweeps<sup>4</sup> is different from PL images acquired during controlled switching of the OP<sup>5,6,9,11</sup> because in the latter approach the image sets defined as  $PL_{1avg} + R_{1avg}$  and  $PL_{2avg} + R_{2avg}$  are determined during image acquisition. It requires a conscious decision about which two OP the switching will be conducted between. This results in an immediate assignment of the acquired images to either one of the two groups. For the image processing step, this means that applying the  $\Delta PL$  algorithm does not require any decision-making and is conducted by averaging and subtracting the two distinct image sets. PL imaging with IV curve sweeps does not require any decision-making about the OP before or during imaging, and the decision about which images will form either  $PL_{1avg} + R_{1avg}$  or  $PL_{2avg} + R_{2avg}$  sub-sets is therefore postponed to the image processing stage. But defining two image sub-sets can potentially be more complicated to carry through than choosing only one image sub-set for the PCC algorithm implementation.

### 1. Data generation

Consequences of dividing images into sub-sets during data processing and not image acquisition stage are implied in Fig. 10(a)-(b). An exhaustive search might often be necessary because one does not know what information is hidden in im-

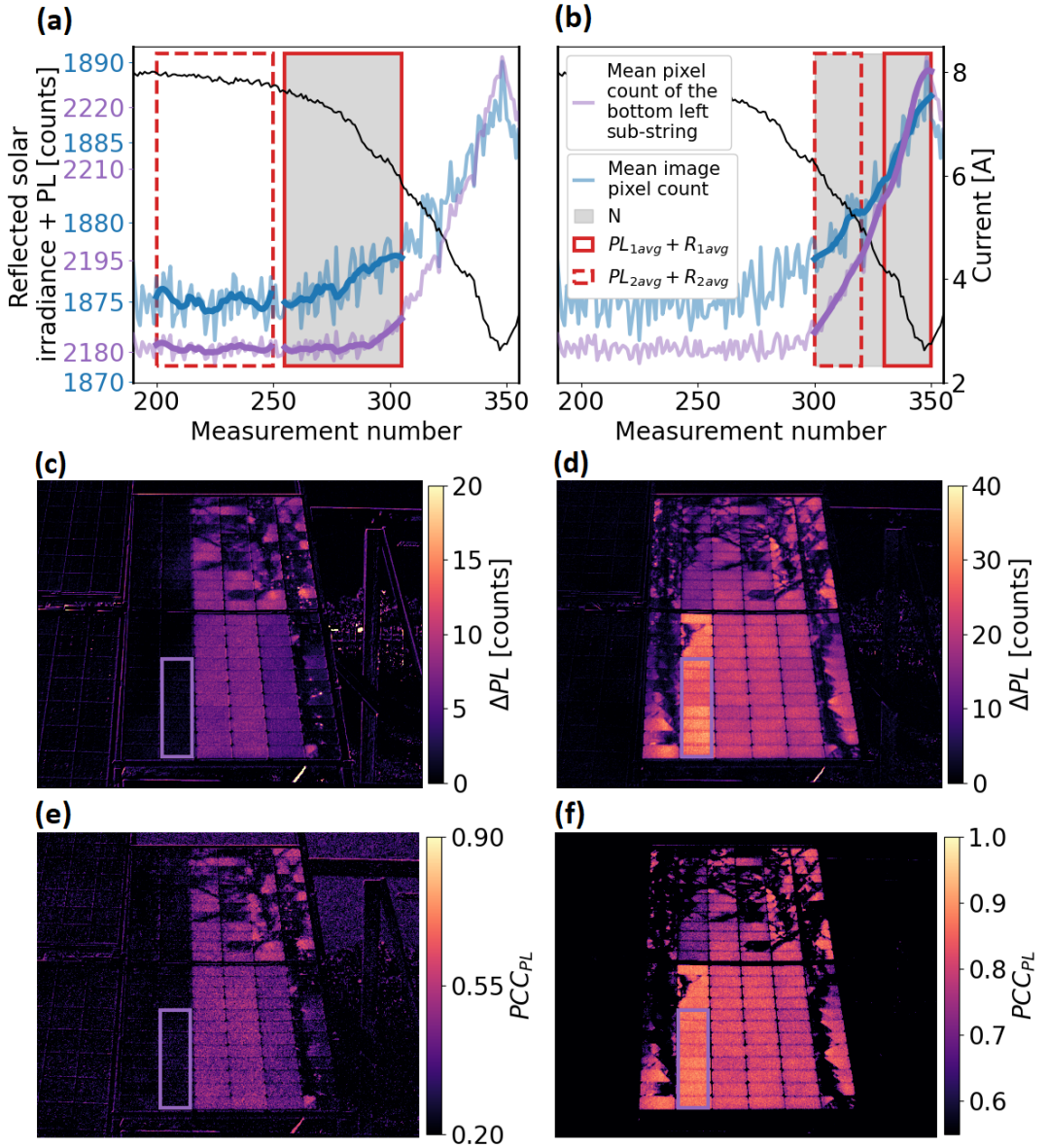


FIG. 10. Illustration of how 150 images from the original *PERC1* image series were used in two different ways (a)-(b) in order to obtain two  $\Delta PL$  (c)-(d) and two  $PCC_{PL}$  images (e)-(f). Two image sub-sets,  $PL_{1avg} + R_{1avg}$  and  $PL_{2avg} + R_{2avg}$ , represented with red squares, each consisting of 50 images (a) and 20 images (b), were acquired during high and low levels of current extraction and used to obtain a  $\Delta PL$  image in (c) and (d). A series of  $N=50$  images (grey region) collected during high level of current extraction (a) and low level of current extraction (b) is used to obtain the corresponding  $PCC_{PL}$  images in (e) and (f). The bottom left sub-string has low values in (c) and (e) compared to (d) and (f). The signal emitted from that part of the module within the purple square in (c)-(f) is compared in (a)-(b) (purple line) with the reference signal from *PERC1* image series (blue line). The trend of the developing signal is emphasized with dark purple and dark blue lines (a)-(b).

ages obtained on different levels of current extraction, as is illustrated in Fig. 10(c)-(f). However, carrying through an exhaustive search generates more data.

The images marked with the grey squares in Fig. 10(a)-(b) illustrate the sub-sets used for calculation of the two  $PCC_{PL}$  images in Fig. 10(e)-(f). These two images were obtained by initiating an unsupervised, exhaustive search for  $PCC_{PL}$  images, which might obtain diverging information. Firstly, the  $N$  number of images was defined as 50. The starting point was chosen at image number 200 and the end point was number 350. In this way the  $PERC1$  data set was narrowed from 500 to 150 images covering the OP from the SC condition to the lowest level of current extraction. The step size was chosen to be 5 images, meaning that the algorithm moved 5 images ahead for every new step. A new  $PCC_{PL}$  image was calculated at every step. This resulted in 21  $PCC_{PL}$  images. Two images among them, which showed diverging information, are presented in Fig. 10(e)-(f).

An unsupervised, exhaustive search with the  $\Delta PL$  algorithm requires the same approach to be initiated. However, every sub-set obtained in such a way could be defined as either  $PL_{1avg} + R_{1avg}$  or  $PL_{2avg} + R_{2avg}$  sub-set because, as shown in Fig. 10(a), valuable information can be disclosed by defining images with a very weak PL signal as the  $PL_1$  intensity level. Consequently, from every sub-set all other sub-sets can be subtracted. This results in 21 potential  $PL_{1avg} + R_{1avg}$  images, 21 potential  $PL_{2avg} + R_{2avg}$  images and 441  $\Delta PL$  images. The  $\Delta PL$  image in Fig. 10(c) was obtained in this way.

The  $\Delta PL$  image in Fig. 10(d) was not visible among the 441  $\Delta PL$  images. A new unsupervised search was initiated with a finer division of the 150 relevant images by reducing the image sub-set size from 50 to 20 images. This resulted in 729  $\Delta PL$  combinations. An image among them, which corresponds with Fig. 10(f), is shown in Fig. 10(d). The two narrow sub-sets, which are used to obtain it, are illustrated in Fig. 10(b). A smaller number of images is needed to disclose more information due to the steep increase in the PL signal intensity during low levels of current extraction.

This example illustrates the disadvantage of processing PL images with  $\Delta PL$  algorithm when they are acquired during an IV curve sweep. The amount of data which can be generated with the  $\Delta PL$  algorithm during unsupervised image processing is much larger than with PCC algorithm. The PCC algorithm will generate less data because it requires only one image sub-set. The  $\Delta PL$  algorithm requires two sub-sets, each of which can be defined as either  $PL_{1avg} + R_{1avg}$  or  $PL_{2avg} + R_{2avg}$ .

## 2. Potential for real-time image processing

As real-time fault detection in PV plants is important<sup>1</sup>, real-time image processing is a step which could be desirable to incorporate in a PL image acquisition procedure. Real-time image processing of the PL images means that it would be possible to obtain information about an IV curve sweep taking place from the PL images only, without depending on additional measurements of electrical parameters. This would

require unsupervised data processing. Different scenarios below will illustrate why we predict that the PCC algorithm is more advantageous than the  $\Delta PL$  algorithm.

The simplest scenario would be imaging a healthy string from which a pronounced PL peak can be detected when it undergoes an IV curve sweep, such as the one in  $PERC3$  image series. Depending on the type of string inverter, one might not know when exactly the IV curve takes place<sup>4</sup>. The imaging starts and batches of images are processed as they are acquired. The advantage of the PCC approach is that a whole batch can be run through the PCC algorithm at once without any type of pre-processing. If the images do not contain information about the changing PL signal, a  $PCC_{PL}$  image of only values close to zero would appear. This image batch could then be deleted while reading in a new group of incoming images and repeating the procedure until a batch of images appears which contains the PL peak. In that case an image such as in Fig. 4(b) would be generated. However, in order to apply the  $\Delta PL$  algorithm, it is necessary to identify the PL peak in the batch of images that is being processed. That could be done by dividing the batch into two or more sub-sets and conducting an unsupervised  $\Delta PL$  calculation until the  $\Delta PL$  image appears, in which the modules "light up". An alternative approach could be to obtain the first derivative of the average image pixel count and in that way identify the PL peak before averaging and subtracting of two sub-sets.

Identifying images with a weak PL signal for the  $\Delta PL$  calculation, such as in  $BSF6$  image series (Fig. 3(f)), might be more complicated. Dividing a batch of images into two or more sub-sets in order to locate the PL peak with an unsupervised  $\Delta PL$  approach might be more time consuming because the PL signal here is narrower than in  $PERC3$  and  $PERC1$  image series. Since the PL peak is quite noisy and therefore hardly visible by inspection, it is also questionable whether a first derivative would detect it. Smoothing of the average image pixel count might help in this respect. Application of the PCC algorithm requires also an adaptation in the form of smoothing. The effect of smoothing with SG filter on the reference signal across 300 images is illustrated in Fig. 11(a). A  $PCC_{PL}$  image obtained without smoothing is shown in Fig. 11(b), and with smoothing in Fig. 11(c). It becomes visible in Fig. 11(c) compared to Fig. 11(b) which modules undergo an IV curve sweep as well as which cells are damaged.

Another scenario would entail simultaneously imaging two or more strings which undergo an IV curve sweep almost at the same time. This is illustrated in Fig. 12, by merging the images from data series  $PERC3$  and  $PERC1$ . In that case, the average image pixel count i.e., the reference signal  $Y$ , consists of two PL peaks which partly overlap, as in Fig. 12(a). Running this image series with 500 images through the PCC algorithm results in a  $PCC_{PL}$  image as shown in Fig. 12(b), where both the damaged module and the string of three modules have high correlation values. This scenario is the same as the first scenario in which the PL signal is pronounced and no smoothing is needed. For the  $\Delta PL$  algorithm application, this would mean, as described above, that it is first necessary to identify the images with higher PL signal intensity.

A more complicated scenario would be when two or more

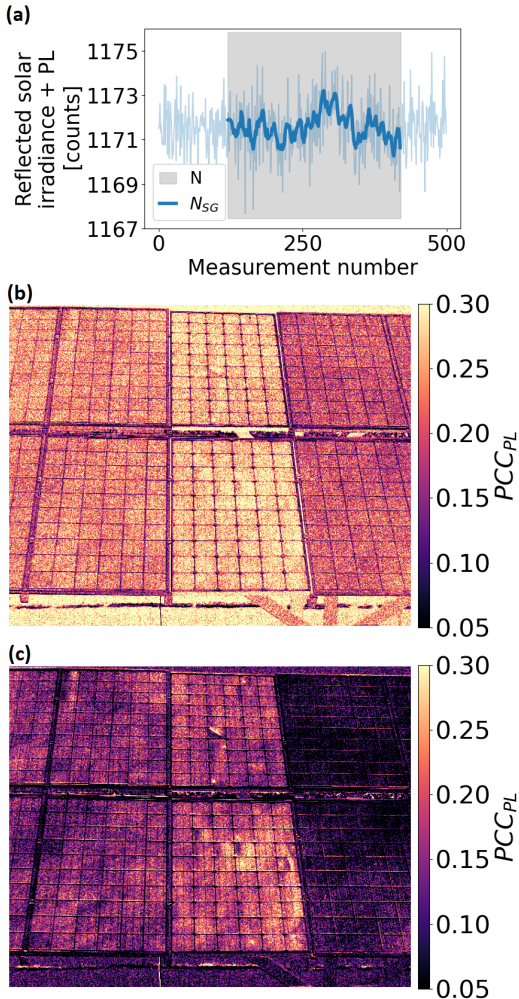


FIG. 11. The effect of smoothing with the SG filter (window size 15 and polynomial order 3) is shown on the reference signal  $Y$  from the *BSF6* data series (a). The  $PCC_{PL}$  image obtained without (b) and with smoothing (c) of the reference signal across  $N$  images.

strings, which do not undergo an IV curve sweep at the same time, are imaged simultaneously. This would result in an average image pixel count as shown in Fig. 13(a). The first and the second PL peak originate from the *PERC3* and *PERC1* image series, respectively, and are indicated with orange crosses and red dots. The  $PCC_{PL}$  image obtained from such an image series is shown in Fig. 13(b). The damaged module shows very low correlation values, up to 0.2, while the string of three modules has correlation coefficient around 0.9.

The reason for this difference in  $PCC_{PL}$  values is illustrated

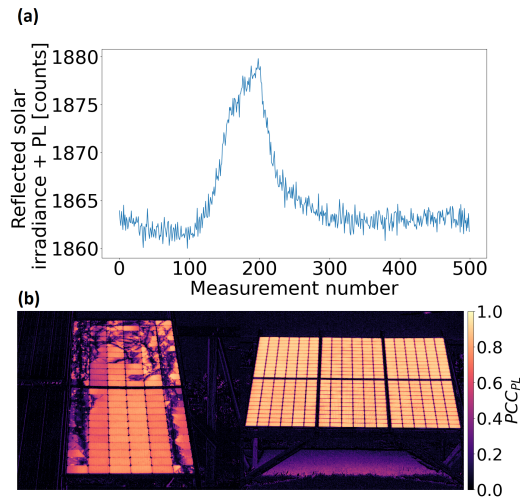


FIG. 12. Imaging of two strings which undergo an IV curve sweep almost at the same time. This is illustrated by merging the *PERC3* and *PERC1* data series. The average image pixel count shows two peaks which partly overlap (a). The  $PCC_{PL}$  image (b) obtained in this way has quite high correlation values across both strings.

in Fig. 13(c)-(d) by plotting the average pixel count from the damaged module and the string of three modules against the reference signal from Fig. 13(a). The linear correlation with the reference signal breaks down in case of the damaged module, Fig. 13(c). Its average signal is no longer linearly similar with the mean image pixel count because the PL peak from the *PERC3* image series (orange crosses) introduces a pronounced tail. That is not the case when correlating the average signal from the three modules with the reference signal  $Y$  in Fig. 13(d). Non-linearity introduced by the damaged module (red dots) is too weak to affect the strong linear relationship between the string in question and the dominant PL peak in the reference signal.

Even though the  $PCC_{PL}$  values across the damaged module are very low, valuable information can still be obtained about the extent of its damage. While the entire such image series can be processed with the PCC algorithm, the  $\Delta PL$  algorithm would require separate identification of the two peaks in Fig. 13(a) in order to obtain two  $\Delta PL$  images.

#### IV. CONCLUSIONS

A PL image series obtained during a string inverter's IV curve scan contains a time-dependent PL signal. This enables application of the Pearson correlation coefficient in order to eliminate the detected reflected solar irradiance and disclose the PL signal. The  $PCC_{PL}$  images show a very good correspondence with the  $\Delta PL$  images.

The PCC algorithm is more robust to varying solar irradi-



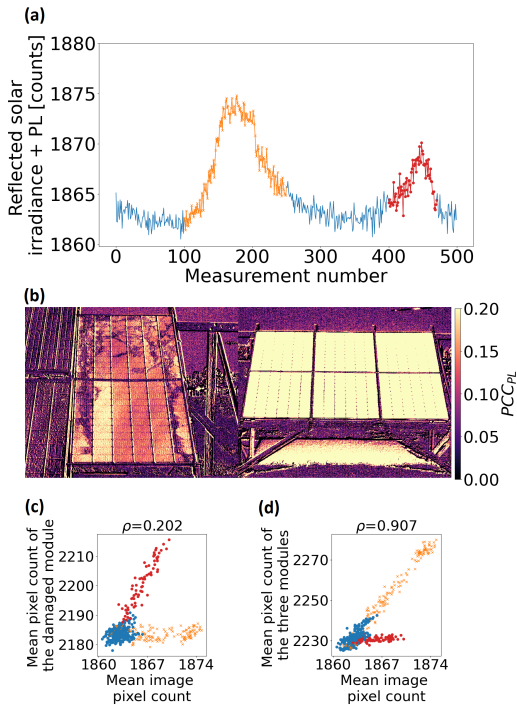


FIG. 13. The reference signal  $Y$  consists of two separate PL peaks if two strings are imaged simultaneously without undergoing IV curve sweeps at the same time. Images in which the PL signal increase originates from separate strings are marked in orange and red (a). The  $PCC_{PL}$  image (b) obtained with such a reference signal shows quite low correlation values for the damaged module. The mean pixel count from the damaged module as a function of the reference signal has  $\rho = 0.202$  (c) and the mean pixel count from the three healthy modules as a function of the reference signal has  $\rho = 0.907$  (d).

ance resulting in a more successful separation of the module pixels from the surrounding pixels. This is manifested in the background pixel values being considerably lower than the module pixel values (increased contrast). The algorithm is very sensitive when it comes to recognizing the PL signal and is better at segmenting the ground-reflected PL emitted from the backside of the bifacial modules.

The PCC algorithm is able to process PL signal from asynchronously emitting strings in the same way as from a single string. This favors high through-put and unsupervised image processing in real-time situations for image sets collected during IV curve sweeps. The method shows promise as a tool for monitoring the condition of modules in industrial PV plants.

## ACKNOWLEDGMENTS

This work was performed within The Norwegian Research Center for Sustainable Solar Cell Technology (FME SU-SOLTECH, project number 257639/E20). The center is co sponsored by the Research Council of Norway and its research and industry partners.

## DATA AVAILABILITY STATEMENT

Data available on request from the authors.

- <sup>1</sup>M. Meribout, V. K. Tiwari, J. P. P. Herrera, and A. N. M. A. Baobaid, "Solar panel inspection techniques and prospects," *Measurement*, 112466 (2023).
- <sup>2</sup>O. Kunz *et al.*, "Outdoor luminescence imaging of field-deployed pv modules," *Progress in Energy* 4(4), 1–23 (2022).
- <sup>3</sup>W. Herrmann *et al.*, "Qualification of photovoltaic (pv) power plants using mobile test equipment," International Energy Agency Photovoltaic Power Systems Programme T13-24 (2021).
- <sup>4</sup>M. Vuković *et al.*, "Noninvasive photoluminescence imaging of silicon pv modules in daylight," *Applied Physics Letters* 120, 1–11 (2022).
- <sup>5</sup>T. J. Silverman *et al.*, "Illuminated outdoor luminescence imaging of photovoltaic modules," *IEEE 44th Photovoltaic Specialist Conference*, 3452–3455 (2017).
- <sup>6</sup>R. Bhoopathy *et al.*, "Outdoor photoluminescence imaging of photovoltaic modules with sunlight excitation," *Progress in Photovoltaics: Research and Applications*, 69–73 (2018).
- <sup>7</sup>R. Bhoopathy *et al.*, "Outdoor photoluminescence imaging of solar panels by contactless switching: technical considerations and applications," *Progress in Photovoltaics: Research and Applications*, 217–228 (2020).
- <sup>8</sup>O. Kunz *et al.*, "High throughput outdoor photoluminescence imaging via pv string modulation," *48th IEEE Photovoltaic Specialists Conference* (2021).
- <sup>9</sup>L. Koester *et al.*, "Development of daylight photoluminescence technique for photovoltaic modules and investigation of temperature dependency," *37th European Photovoltaic Solar Energy Conference and Exhibition*, 908–913 (2020).
- <sup>10</sup>L. Koester *et al.*, "Quality assurance of the photovoltaic power plants installation stage - a complementary strategy based of photoluminescence and steady-state thermography," *38th European Photovoltaic Solar Energy Conference and Exhibition*, 1042–1050 (2021).
- <sup>11</sup>M. Vuković *et al.*, "Photoluminescence imaging of silicon modules in a string," *Progress in Photovoltaics: Research and Applications*, 1–11 (2022).
- <sup>12</sup>C. G. C. Center and L. Huawei Technologies Co., "Smart i-v curve diagnosis: technical white paper," (2020), last accessed 8 May 2023.
- <sup>13</sup>I. Fronius, GmbH, "Lower losses in the case of partial shading of pv systems," (2022), last accessed 8 May 2023.
- <sup>14</sup>Danfoss, "Tlx reference manual," (2010), last accessed 8 May 2023.
- <sup>15</sup>S. Spataru, D. Sera, T. Kerekes, and R. Teodorescu, "Monitoring and fault detection in photovoltaic systems based on inverter measured string iv curves," in *31st European Photovoltaic Solar Energy Conference and Exhibition (WIP Wirtschaft und Infrastruktur GmbH & Co Planungs KG, 2015)* pp. 1667–1674.
- <sup>16</sup>A. H. Smets, K. Jäger, O. Isabella, R. A. Swaaij, and M. Zeman, *Solar Energy: The physics and engineering of photovoltaic conversion, technologies and systems* (UIT Cambridge, 2015).
- <sup>17</sup>D. Acharya *et al.*, "Application of adaptive savitzky—golay filter for eeg signal processing," *Perspectives of Science* 8, 677–679 (2016).
- <sup>18</sup>Sungrow, "Data-driven monitoring starts at the inverter," (2020), last accessed 8 May 2023.
- <sup>19</sup>T. Trupke *et al.*, "Spatially resolved series resistance of silicon solar cells obtained from luminescence imaging," *Applied Physics Letters* 90 (2007).
- <sup>20</sup>M. Guada *et al.*, "Daylight luminescence system for silicon solar panels based on a bias switching method," *Energy Science and Engineering*, 1–15 (2020).

- <sup>21</sup>P. G. Ellingsen *et al.*, "Hyperspectral analysis using the correlation between image and reference," *Journal of Biomedical Optics Letters* 18(2), 020501-1-020501-3 (2013).
- <sup>22</sup>D. Inamdar *et al.*, "The correlation coefficient as a simple tool for the localization of errors in spectroscopic imaging data," *Remote Sensing* 10(2), 231.
- <sup>23</sup>F. van der Meer, "The effectiveness of spectral similarity measures for the analysis of hyperspectral imagery," *International Journal of Applied Earth Observation and Geoinformation* 8(1), 3-17 (2006).
- <sup>24</sup>R. W. Schafer, "What is a savitzky-golay filter?" *IEEE Signal Processing Magazine*, 111-117 (2011).
- <sup>25</sup>J. Chen *et al.*, "A simple method for reconstructing a high-quality ndvi time-series data set based on the savitzky-golay filter," *Remote Sensing of Environment* 91, 332-344 (2004).
- <sup>26</sup>S. Stoicescu *et al.*, "Days:luminescence imaging of pv modules in daylight," 29th European Photovoltaic Solar Energy Conference and Exhibition, 2553-2554 (2014).
- <sup>27</sup>G. Rey *et al.*, "Luminescence imaging of solar modules in full sunlight using ultranarrow bandpass filters," *Progress in Photovoltaics: Research and Applications*, 1-7 (2022).
- <sup>28</sup>O. Kunz *et al.*, "Outdoor pl imaging of crystalline silicon modules at constant operating point," 47th IEEE Photovoltaic Specialists Conference (2020).

# Appendix E

## Paper E



# Photoluminescence imaging of field-installed photovoltaic modules in diffuse irradiance

M. Vuković, M. Hillestad, M. Jakovljević, A. S. Flø, E. Olsen, I. Burud<sup>1</sup>  
*Faculty of Science and Technology, Norwegian University of Life Sciences, Ås, Norway*

(\*Electronic mail: marija.vukovic@nmbu.no)

(Dated: 31 May 2023)

Photoluminescence imaging under sunlight excitation has in the recent years been proposed as a promising inspection technique of field-installed photovoltaic modules. Virtually all studies have been conducted in full sunlight and clear sky conditions. A study in which photoluminescence images had been acquired at an irradiance level below  $100 \text{ Wm}^{-2}$  using the lock-in technique has shown the potential of these images with respect to defect analysis. Additionally, as on-site measurement techniques, and photoluminescence imaging as such, are subject to weather conditions, it would be favourable to extend its applicability to a wider range of irradiance levels. A method for photoluminescence imaging which does not use the lock-in technique for the purpose of filtering of sunlight was proposed recently. The present study extends the application of this approach to diffuse irradiance conditions. We demonstrate that the method gives valuable information about the modules also in case of image acquisition under diffuse global in-plane irradiance as low as  $40 \text{ Wm}^{-2}$ . Photoluminescence images acquired under low irradiance are comparable to electroluminescence images acquired at 10% of short-circuit current. Photoluminescence imaging has also been conducted successfully from the rear of bifacial modules in these illumination conditions.

## I. INTRODUCTION

Imaging of field-installed photovoltaic (PV) modules for the purpose of fault detection is related to irradiance levels in the surroundings. When detecting the emitted long wave infrared radiation (temperature), luminescence in the short wave infrared region or fluorescence in the visible region, the intensity of solar irradiance plays a role for what information one can obtain from the images. The standard requirement in case of thermal infrared imaging is  $600 \text{ Wm}^{-2}$ , but low irradiance levels of around  $250 \text{ Wm}^{-2}$  are desirable for detection of potential induced degradation (PID)<sup>1-3</sup>. In case of electroluminescence (EL) imaging in daylight, low levels of irradiance, down to  $100 \text{ Wm}^{-2}$ , contribute positively to image quality<sup>4,5</sup>. Ultraviolet fluorescence (UVF) imaging is dependent on excitation with an ultraviolet illumination source and the detection of the emitted signal is affected by daylight, so it is mostly conducted in dark environment<sup>6</sup>.

All reported photoluminescence (PL) imaging approaches of field-installed modules, apart from one<sup>7</sup>, are based on the Sun as an excitation source. Almost all of them have been carried out in clear sky and high irradiance conditions<sup>8-17</sup>. But waiting for such conditions in order to conduct imaging is cumbersome and not always appropriate. The question whether the PL image acquisition can be extended to cloudy weather with low irradiance levels is worth examining.

PL imaging in low irradiance conditions can also be useful from the perspective of defect analysis. PL images collected at around  $100 \text{ Wm}^{-2}$  are expected to correspond to EL images obtained with 10% of short-circuit (SC) current<sup>18</sup> and these images can be used for analysis of inactive cell areas<sup>19,20</sup>. One of the two reported cases of PL imaging under diffuse solar irradiance has shown that PL images acquired at an irradiance level below  $100 \text{ Wm}^{-2}$  display valuable information about PID degradation<sup>21</sup>.

The question of whether PL imaging in low irradiance con-

ditions results in interpretable images is not entirely conclusive. The second reported case of PL imaging under lower illumination intensity has shown that a decreasing level of irradiance has a negative effect on PL image quality, with  $260 \text{ Wm}^{-2}$  being the lowest tested irradiance level<sup>4</sup>.

In the present study, our recently proposed PL imaging technique which detects the change in the PL emission by relying on the string inverter's ability to conduct current-voltage (IV) curve sweeps<sup>17</sup> will be put to test. In the present work, we investigate the applicability of this imaging method and a novel algorithm<sup>22</sup> on the PL images of bifacial passivated emitter and rear cell (PERC) modules collected at irradiance levels below  $100 \text{ Wm}^{-2}$ . As it may be advantageous to image the bifacial modules from the rear<sup>19</sup>, we also test PL imaging applied in this context.

## II. METHODOLOGY

Separation of the PL signal from the reflected solar irradiance can be achieved if a change in the PL signal is detected due to the change in the operating conditions of a module or a string. This can be the case when a string inverter initiates an IV curve sweep<sup>17</sup>. During the swipe, the current drops significantly. This decrease in the extracted current results in an increase in the emitted PL signal at around 1140 nm from within the silicon semiconductor material. The PL signal can be registered with a short-wave infrared camera with an InGaAs detector, such as Raptor Photonics Owl 640S with an optical range 900 nm - 1700 nm and a resolution  $640 \times 512$ . An optical band-pass filter produced by Edmund Optics (center wavelength of 1150 nm and an optical density of  $\geq 4.0$ ) is used in order to decrease the amount of reflected sunlight detected by the camera.

Four bifacial monocrystalline PERC modules of type JAM72D20 produced by JA Solar have been imaged. They consist of 144 half-cells and have a rated nominal power of

460 W, open circuit voltage ( $V_{OC}$ ) of 49.91 V (0.693 V/cell) and short circuit current ( $I_{SC}$ ) of 11.5 A. A module of this type is illustrated in Fig. 1. The three sub-strings in the upper half of the module are connected in parallel with the three sub-strings in the lower half of the module.

The modules were installed first time in 2021 and are connected in two strings to two Fronius Primo 3.0 string inverters. One module from each string has been chosen for a more detailed analysis: an undamaged module, termed M1, and a damaged module, termed M2. Module M2 was severely damaged before installation.

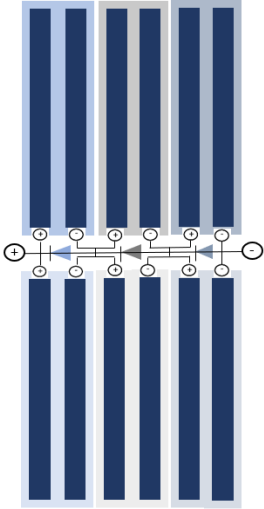


FIG. 1. A bifacial PERC module of type JAM72D20 in which three sub-strings in the upper half of the module are connected in parallel with the three sub-strings in the lower half of the module.

Table I lists important aspects of the data collection campaigns with respect to module notation, in-plane global irradiance intensity, module's condition, camera position, exposure time and data series notation. Each module has been imaged two times under diffuse irradiance, once from the front and once from the rear, as illustrated in Fig. 2.

TABLE I. Overview of the investigated modules, irradiance conditions and camera settings.

Module	In-plane global irradiance $Wm^{-2}$	Module's condition	Camera position	Exposure time $ms$	Image series
M1	46	Undamaged	Front	3.0	M1F
	72		Rear	1.5	M1R
M2	53	Damaged	Front	3.0	M2F
	40		Rear	2.0	M2R

The algorithm used for image processing in the present

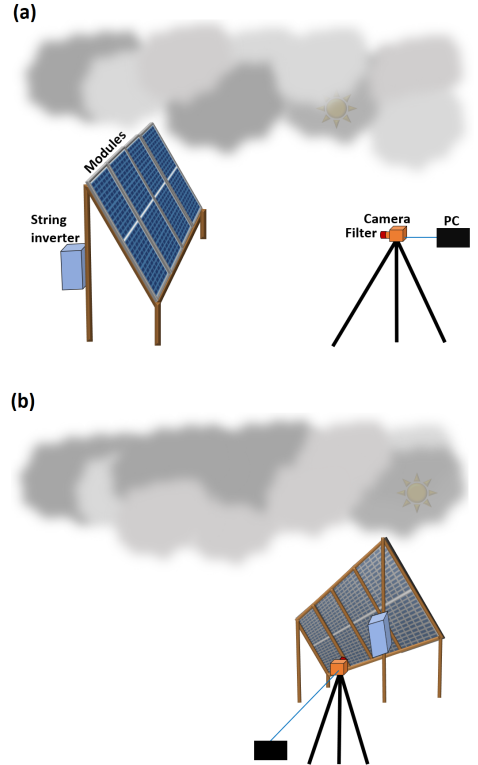


FIG. 2. Experimental set-up consisting of a short wave infrared camera with a filter, bifacial PERC modules and a string inverter during imaging from front (a) and rear (b). The imaging was conducted during two days of heavy clouds, at diffuse irradiance conditions between  $40 Wm^{-2}$  and  $72 Wm^{-2}$ .

study is Pearson correlation coefficient (PCC), presented recently as an alternative to the subtraction algorithm which results in  $\Delta PL$  images<sup>22</sup>. Applying it to the set of  $N$  PL images results in an image of PCC values, termed  $PCC_{PL}$ . It is obtained by correlating the signal in every pixel in the spatial domain across the  $N$  number of images with the reference signal defined as the mean image pixel count. The  $N$  number of images is selected as those images in which the peak of the PL signal changes due to the IV curve sweep<sup>22</sup>.

For the purpose of validation,  $PCC_{PL}$  images obtained from the front side have been compared to  $PCC_{PL}$  images obtained under direct irradiance (approximately  $800 Wm^{-2}$ ) and EL images obtained in dark with short-circuit current and with 10% of short-circuit current,  $EL_{SC}$  and  $EL_{0.1SC}$ . It is expected that the  $PCC_{PL}$  image obtained with irradiance below  $100 Wm^{-2}$  will resemble the  $EL_{0.1SC}$  image because the current level of 10% of  $I_{SC}$  is expected to be reached when the irradiance level is 10% of the irradiance at the standard test conditions<sup>18</sup>.

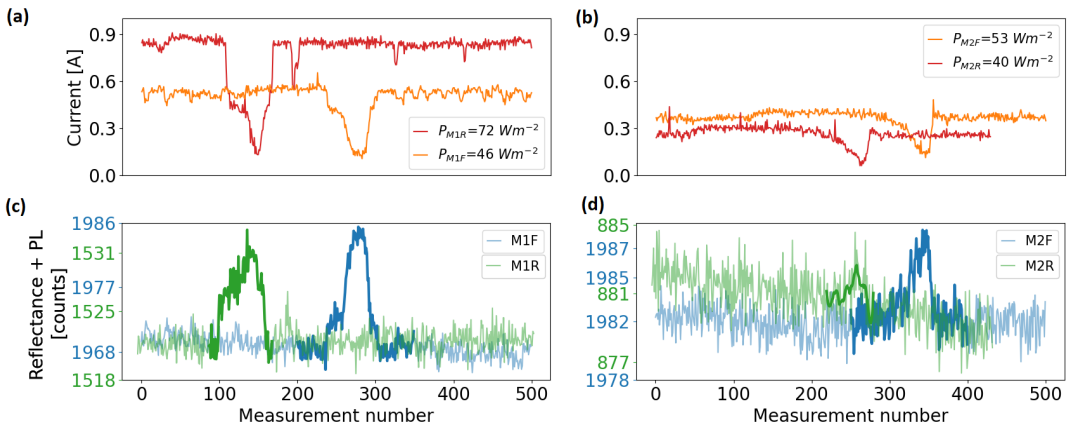


FIG. 3. Change in current during acquisition of image series M1F, M1R, M2F and M2R (a)-(b) is displayed together with the value of average in-plane global irradiance. Average image pixel count of the four image series (c)-(d) with the darker color indicates the  $N$  images used for calculation of the  $PCC_{PL}$  images.

### III. RESULTS AND DISCUSSION

Current measurements and the mean image pixel count obtained from the image series M1F, M1R, M2F and M2R are displayed in Fig. 3. Figure 3(a)-(b) show the variation in current during the four IV curve sweeps and the recorded average in-plane irradiance. Figure 3(c)-(d) show the corresponding mean image pixel count of the four image series. The measurements (images) marked with dark blue and dark green in Fig. 3(c)-(d) are used in order to obtain  $PCC_{PL}$  images shown below.

Despite very low current levels and their small variation during IV curve sweeps, the average image pixel count curves of M1F, M1R and M2F image series have pronounced PL peaks. This can be ascribed to a 5-10 times higher exposure time compared to the same imaging procedure conducted in direct irradiance<sup>17</sup> as well as to the higher  $V_{OC}$  of the investigated modules compared to the aluminium back-surface field cell technology<sup>16,22</sup>. The height of the PL peaks is not comparable between M1F and M1R nor between M2F and M2R because the exposure times were not the same, as shown in Table I.

The PL peak of the M2R image series, Fig. 3(b), is noisy and difficult to detect. This coincides with the fact that the irradiance level was the lowest in the M2R image series out of the four data sets and that the M2 module is damaged. The dark green line which indicates the  $N$  number of images used from that series is drawn with Savitzky-Golay smoothing filter, applied to the M2R series before the PCC algorithm. It has been shown that this type of smoothing considerably improves the extraction of the PL signal from noisy data sets with low PL signal intensity<sup>22</sup>.

The M1F and M1R image series are used to illustrate how well the PCC algorithm performs on images collected under low irradiance in Fig. 4. The module pixels have quite high

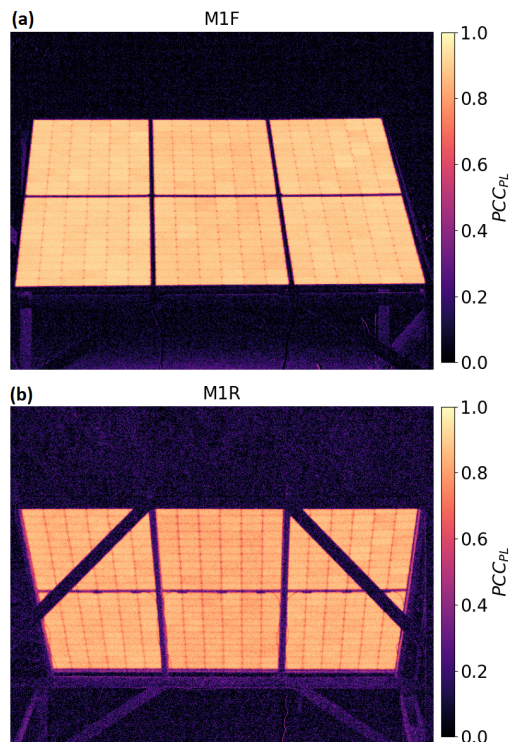


FIG. 4.  $PCC_{PL}$  images of a string of three modules obtained from image series M1F (a) and M1R (b). The module in the middle is called M1.

correlation values, above 0.8, and are well separated from the background pixels with values below 0.3. This is comparable to high PCC module values and low PCC background values in  $PCC_{PL}$  images obtained under direct irradiance. Both the front and rear side image in Fig. 4 show that the three modules are intact and confirm thus the information about the modules obtained from images acquired under direct irradiance<sup>22</sup>.

In order to investigate the variation of the PL signal on cell level, images from M1F and M2F image series have been cropped and transformed so that they only show modules M1 and M2. In this way they can be easier compared to  $PCC_{PL}$  images obtained under direct irradiance, as well as  $EL_{SC}$  and  $EL_{0.1SC}$  images. Figure 5(a)-(d) show  $EL_{SC}$ ,  $EL_{0.1SC}$  and  $PCC_{PL}$  images obtained in direct and diffuse irradiance of module M1, while Fig. 6(a)-(d) show the same images of module M2. All images have been obtained from the front.

It is visible in Fig. 5 that the  $EL_{SC}$  image and  $PCC_{PL}$  image obtained in direct irradiance, on the one hand, and the  $EL_{0.1SC}$  image and  $PCC_{PL}$  image obtained in diffuse irradiance, on the other hand, convey similar information, as expected<sup>18</sup>. It should be noted that the  $PCC_{PL}$  image in Fig. 5(b) deviates from the  $EL_{SC}$  image in Fig. 5(a) with respect to the dark lines

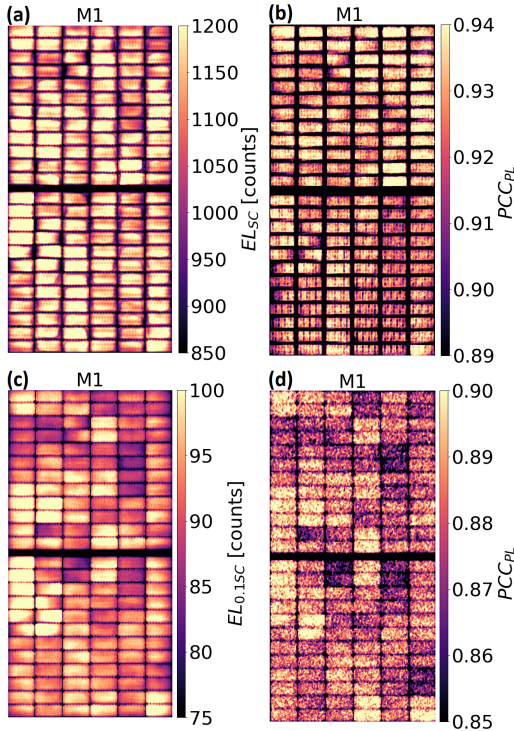


FIG. 5. The  $EL_{SC}$  image (a),  $PCC_{PL}$  image obtained in direct irradiance (b),  $EL_{0.1SC}$  image (c) and  $PCC_{PL}$  image obtained in diffuse irradiance (d) of M1 during front side imaging.

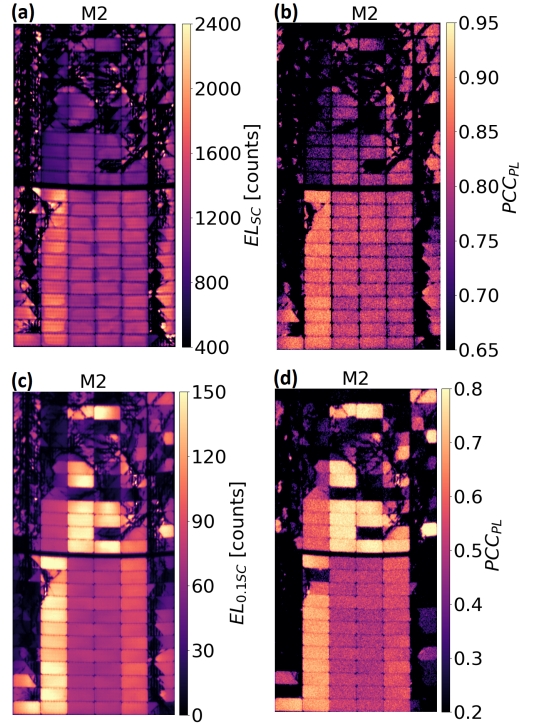


FIG. 6. The  $EL_{SC}$  image (a),  $PCC_{PL}$  image obtained in direct irradiance (b),  $EL_{0.1SC}$  image (c) and  $PCC_{PL}$  image obtained in diffuse irradiance (d) of M2 during front side imaging.

across the cells in the former. These depict the busbars<sup>22</sup>. The damaged M2 module in Fig. 6 shows the same correspondence as M1 between the  $EL_{SC}$  image and  $PCC_{PL}$  image obtained in direct irradiance and the  $EL_{0.1SC}$  image and  $PCC_{PL}$  image obtained in diffuse irradiance.

Unexpectedly, the  $PCC_{PL}$  image in Fig. 5(d) of a healthy M1 module is more grainy, and it seems therefore that it has a lower quality, than the image in Fig. 6(d) of a damaged M2 module. The image in Fig. 5(d) is obtained based on the M1F image series in the same way as the image in Fig. 4(a). The only difference is that it has been cropped, transformed and contrast adjusted from interval [0.1] to interval [0.85-0.9]. This very narrow region of pixel values was selected in order to show the contrast between the cells in Fig. 5(d), which resembles the contrast in the  $EL_{0.1SC}$  image in Fig. 5(c). The value interval used in Fig. 6(d) is much wider and this image of the damaged M2 module therefore seems to have a better quality. The selected value intervals for images in Fig. 5(d) and Fig. 6(d) are shown on their histograms in Fig. 7(a) and Fig. 7(b), respectively.

With respect to the damage which is identifiable from the images of M2 in Fig. 6, the same overall pattern of cracks



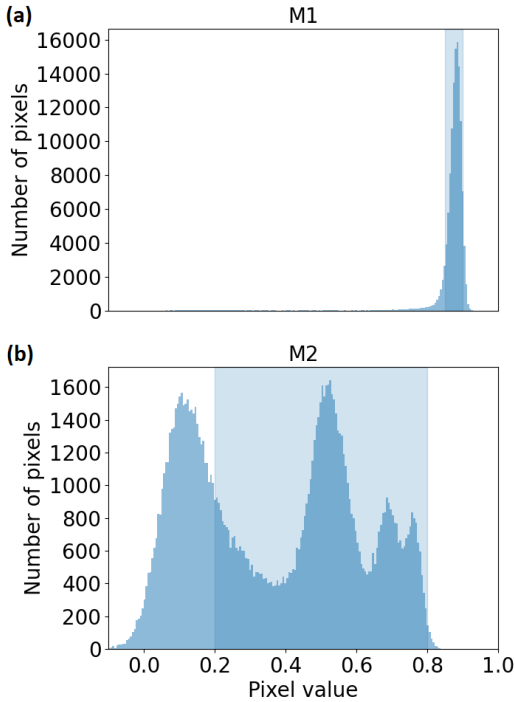


FIG. 7. Histogram of  $PCC_{PL}$  image of M1 presented in Fig. 5(d) (a) and of M2 presented in Fig. 6(d) (b) with an indicated value range used on the colorbars in the two figures.

and isolated regions is visible on all four images. Both EL images in Fig. 6(a) and Fig. 6(c) show that the lower left sub-string emits a higher EL signal than the upper left sub-string. As they are connected in parallel, this gives reason to assume that the upper left sub-string is more damaged and that more current therefore flows through the lower sub-string. The same information can be obtained from the two  $PCC_{PL}$  images in Fig. 6(c) and Fig. 6(d).

However, the  $EL_{SC}$  image of M2 in Fig. 6(a) differs from the  $EL_{0.1SC}$  image in Fig. 6(c) with respect to the emitted signal in the upper center sub-string. More EL signal is emitted from that sub-string than from the lower center sub-string when 10% of SC current passes through the module. This is an indication that the upper center sub-string might pose a path with smaller resistance, despite the damage in that part of the module, when the injection level is low. The same information is obtainable from the two  $PCC_{PL}$  images in Fig. 6(b) and Fig. 6(d).

In order to see how the isolated regions of M2 with low EL and PL emission correspond, the contrast of images in Fig. 6(c)-(d) were adjusted in Fig. 8. The two images appear quite similar, but the regions marked with blue squares show some differences between the cells. In the  $EL_{0.1SC}$  image, there are

damaged cells which emit both a weak and a strong EL signal, while there is almost no PL signal emitted from the same cells in the  $PCC_{PL}$  image.

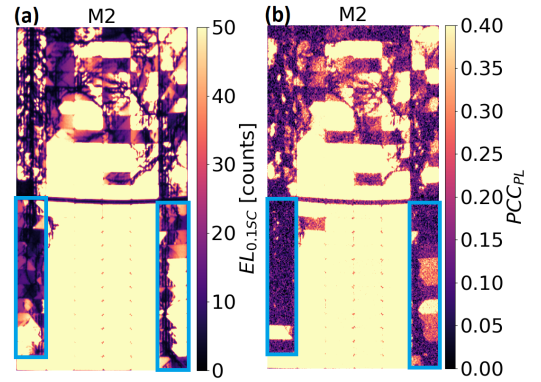


FIG. 8. The  $EL_{0.1SC}$  (a) and  $PCC_{PL}$  (b) image of M2 after the contrast has been adjusted from Fig. 6(c)-(d) in order to emphasize and investigate the correspondence between the regions with low signal intensity.

The  $PCC_{PL}$  images of M1 and M2 obtained from the rear are shown in Fig. 9(a) and Fig. 9(b), respectively. The dark horizontal and diagonal lines in Fig. 9(b) show the back side construction holding the modules in place. For easier comparison with images taken from the front, the pixels in the images in Fig. 9 have been mirrored along the x-axis. They show good correspondence with the images of M1 and M2 obtained from the front in Fig. 5(d) and Fig. 6(d).

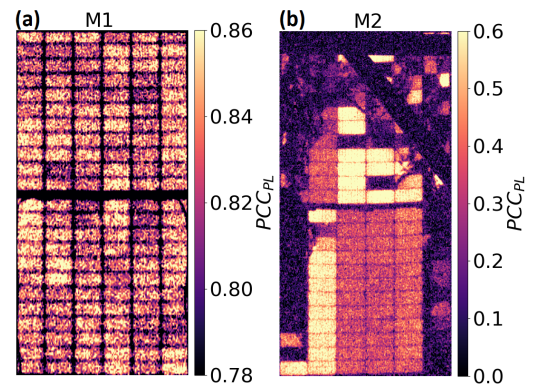


FIG. 9. The  $PCC_{PL}$  images of M1 (a) and M2 (b) from the rear obtained from the image series M1R and M2R.

#### IV. CONCLUSIONS

Acquisition of PL images in low diffuse irradiance conditions during IV curve sweeps results in interpretable images despite very little variation in current extraction. This is also the case for PL images obtained from the rear of bifacial modules. The images correspond to EL images obtained with 10% of short-circuit current. This shows that PL imaging during IV curve sweeps can be extended to weather conditions outside high irradiance and clear sky conditions and that these images might offer diagnostic information about the module defects.

#### ACKNOWLEDGMENTS

This work was performed within The Norwegian Research Center for Sustainable Solar Cell Technology (FME SU-SOLTECH, project number 257639/E20). The center is co sponsored by the Research Council of Norway and its research and industry partners.

#### DATA AVAILABILITY STATEMENT

Data available on request from the authors.

- <sup>1</sup>B. C *et al.*, "Infrared imaging of photovoltaic modules: a review of the state of the art and future challenges facing gigawatt photovoltaic power stations," *Solar Energy* 211 , 712–724 (2022).
- <sup>2</sup>"Iec ts 62446-3:2017 photovoltaic (pv) systems—requirements for testing, documentation and maintenance, part 3: photovoltaic modules and plants—outdoor infrared thermography," Standard (2017).
- <sup>3</sup>B. C *et al.*, "Influence of the irradiance on the detection and performance of pid-affected pv-modules," 35th European Photovoltaic Solar Energy Conference and Exhibition , 2001–2004 (2018).
- <sup>4</sup>M. Guada *et al.*, "Daylight luminescence system for silicon solar panels based on a bias switching method," *Energy Science and Engineering* , 1–15 (2020).
- <sup>5</sup>G. A. d. R. Benatto *et al.*, "Daylight electroluminescence of pv modules in field installations: When electrical signal modulation is required?" 8th World Conference on Photovoltaic Energy Conversion , 735–739 (2022).
- <sup>6</sup>M. Köntges, A. Morlier, G. Eder, E. Fleiß, B. Kubicek, and J. Lin, "Ultraviolet fluorescence as assessment tool for photovoltaic modules," *IEEE Journal of Photovoltaics* 10, 616–633 (2020).
- <sup>7</sup>B. Doll *et al.*, "Photoluminescence for defect detection on full-sized photovoltaic modules," *IEEE Journal of Photovoltaics* , 1–11 (2021).
- <sup>8</sup>T. J. Silverman *et al.*, "Illuminated outdoor luminescence imaging of photovoltaic modules," *IEEE 44th Photovoltaic Specialist Conference* , 3452–3455 (2017).
- <sup>9</sup>R. Bhoopathy *et al.*, "Outdoor photoluminescence imaging of photovoltaic modules with sunlight excitation," *Progress in Photovoltaics: Research and Applications* , 69–73 (2018).
- <sup>10</sup>R. Bhoopathy *et al.*, "Outdoor photoluminescence imaging of solar panels by contactless switching: technical considerations and applications," *Progress in Photovoltaics: Research and Applications* , 217–228 (2020).
- <sup>11</sup>O. Kunz *et al.*, "Outdoor pl imaging of crystalline silicon modules at constant operating point," 47th IEEE Photovoltaic Specialists Conference (2020).
- <sup>12</sup>O. Kunz *et al.*, "High throughput outdoor photoluminescence imaging via pv string modulation," 48th IEEE Photovoltaic Specialists Conference (2021).
- <sup>13</sup>L. Koester *et al.*, "Development of daylight photoluminescence technique for photovoltaic modules and investigation of temperature dependency," 37th European Photovoltaic Solar Energy Conference and Exhibition , 908–913 (2020).
- <sup>14</sup>L. Koester *et al.*, "Quality assurance of the photovoltaic power plants installation stage - a complementary strategy based of photoluminescence and steady-state thermography," 38th European Photovoltaic Solar Energy Conference and Exhibition , 1042–1050 (2021).
- <sup>15</sup>G. Rey, O. Kunz, M. Green, and T. Trupke, "Luminescence imaging of solar modules in full sunlight using ultranarrow bandpass filters," *Progress in Photovoltaics: Research and Applications* 30, 1115–1121 (2022).
- <sup>16</sup>M. Vuković *et al.*, "Photoluminescence imaging of silicon modules in a string," *Progress in Photovoltaics: Research and Applications* , 1–11 (2022).
- <sup>17</sup>M. Vuković *et al.*, "Noninvasive photoluminescence imaging of silicon pv modules in daylight," *Applied Physics Letters* 120 , 1–11 (2022).
- <sup>18</sup>W. Mühleisen, C. Hirschl, G. Brantegger, L. Neumaier, M. Spielberger, H. Sonnleitner, B. Kubicek, G. Ujvari, R. Ebner, M. Schwark, *et al.*, "Scientific and economic comparison of outdoor characterisation methods for photovoltaic power plants," *Renewable energy* 134, 321–329 (2019).
- <sup>19</sup>"Iec ts 60904-13:2018 photovoltaic devices - part 13: Electroluminescence of photovoltaic modules," Standard (2018).
- <sup>20</sup>M. Köntges, I. Kunze, S. Kajari-Schröder, X. Breitenmoser, and B. Bjørneklett, "Quantifying the risk of power loss in pv modules due to micro cracks," in *25th European Photovoltaic Solar Energy Conference, Valencia, Spain* (2010) pp. 3745–3752.
- <sup>21</sup>L. Stoicescu and M. Reuter, "Daysy contactless measurements of pid shunt resistance in installed pv modules," in *25th European Photovoltaic Solar Energy Conference and Exhibition* (2018) pp. 1337–1339.
- <sup>22</sup>M. Vuković *et al.*, "Extraction of photoluminescence with pearson correlation coefficient from images of field-installed photovoltaic modules," *Journal of Applied Physics* 133 , 1–12 (2023).
- <sup>23</sup>S. Stoicescu *et al.*, "Daysy: luminescence imaging of pv modules in daylight," 29th European Photovoltaic Solar Energy Conference and Exhibition , 2553–2554 (2014).
- <sup>24</sup>S. S. GMBH, "Daysy - daylight luminescence system - measurement guide," [https://www.solarzentrum-stuttgart.com/uploads/file/DaySy\\_Measurement\\_Guide\\_current.pdf](https://www.solarzentrum-stuttgart.com/uploads/file/DaySy_Measurement_Guide_current.pdf) (2019), accessed: 2023-04-01.
- <sup>25</sup>O. Kunz *et al.*, "Outdoor luminescence imaging of field-deployed pv modules," *Progress in Energy* 4(4) , 1–23 (2022).



ISBN: 978-82-575-2082-3

ISSN: 1894-6402



Norwegian University  
of Life Sciences

Postboks 5003  
NO-1432 Ås, Norway  
+47 67 23 00 00  
[www.nmbu.no](http://www.nmbu.no)